Analysis of Cell-Specific Heat Shock Transcriptomes in the Inner Ear

by

Matthew M. Ryals

A dissertation submitted to Johns Hopkins University

in conformity with the requirements

for the degree of Doctor of Philosophy.

Baltimore, Maryland

October 2018

Biochemistry, Cell and Molecular Biology Program (BCMB)

Abstract

Ototoxic drug-induced death of sensory hair cells in the inner ear results in permanent hearing loss. There is currently no therapy available for the millions of patients who experience hearing loss after treatment with lifesaving drugs that have ototoxic side effects. An understanding of protective pathways in the inner ear is necessary for the development of therapies to mitigate ototoxic hearing loss. The induction of heat shock proteins (HSPs) protects hair cells from ototoxic death *in vitro* and in animal models. Furthermore, the protective effect of heat shock is non-cell autonomous, and the glial-like supporting cells in the inner ear may secrete the heat shock protein HSP70 to protect hair cells (May, Kramarenko et al. 2013).

This study elucidates the cell type-specific transcriptional responses in hair cells and supporting cells at steady-state and following heat shock. Two techniques, 1) massively-parallel RNA sequencing (RNA-Seq) of affinity-tagged, ribosomally-immunoprecipitated RNA (RiboTag), and 2) RNA-Seq single-cell profiling were used to accomplish this goal. Results using both techniques show effective isolation of cell type-specific transcriptomes, which were validated using orthogonal experimental techniques. Differential gene expression analysis revealed that the heat shock response is transcriptionally present in both cell types, and that hair cells may have reduced translational capacity to mount a heat shock response at the protein level relative to supporting cells.

This study also utilized the transcriptional profile of heat shock in whole inner ear tissue (from RNA-Seq data) to bioinformatically predict compounds that would mimic the transcriptional response to heat chock in the inner ear. Predicted compounds from this

matching process were screened in in a zebrafish model of ototoxicity and revealed three compounds that protected hair cells. Furthermore, one of those compounds, pifithrin-μ, promoted a heat shock-like transcriptional signature and protected cultured murine inner ear tissue from ototoxic drug-induced hair cell death.

In summary, this study characterizes the transcriptional profiles of inner ear hair and supporting cells and provides insight into the nature of the protective heat shock response in these cell types. Secondly, this study translates the native heat shock response of the inner ear into a pharmacologically-induced protective effect against ototoxic hair cell death, which provides a valuable workflow for future studies aimed at preventing hair cell death and hearing loss.

Readers:

Lisa L. Cunningham, National Institutes of Health, Bethesda MD, USA

Randall R. Reed, Johns Hopkins University School of Medicine, Baltimore MD, USA

Acknowledgements

I am grateful to my research mentor Lisa Cunningham, who has fostered my development as a scientist starting with my first research role in her laboratory the first year after my undergraduate degree all way through my training as a graduate student. Her kindness, intellectual curiosity, and drive to help her mentees succeed as scientists is something that I believe puts her into a league of her own as a mentor and researcher. She has been an exceptional advisor to me in the development of my career.

I would like to acknowledge the professors and administrative staff in the Biochemistry, Cell, and Molecular Biology program at Johns Hopkins University. I would especially like to acknowledge now-retired program director Carolyn Machamer, and my thesis committee chair Randy Reed. Carolyn went the extra mile in helping me succeed as a graduate student, and Randy was willing to kindly step in and assume the role as both my liaison to Johns Hopkins as well as being my thesis mentor and co-reader.

I have appreciated working with everyone in the Cunningham lab and the other labs I have worked and interacted with during my time at the National Institutes of Deafness and Other Communication Disorders, and I would especially like to thank Lindsey May, Robert Morell, and Matthew Kelley. Lindsey is an excellent researcher and laboratory manager who was an invaluable colleague to collaborate with during my time as a graduate student. Robert Morell is one of my thesis committee members, but he has also helped me immensely with the computational aspects of this thesis and provided extensive advice during my analyses. Matthew Kelley generously provided me with the use of his laboratory's reagents and equipment and provided his careful advice and helpfulness as one of my thesis committee members. I also spent three weeks in April 2017 performing experiments in Seattle, Washington at the University of Washington, where I utilized the laboratories of Edwin Rubel and David Raible, and I am grateful to them as well as their lab members for hosting me.

Lastly, I would like to acknowledge my friends and family members. My grandfather who passed away during my time in graduate school taught me to always strive to be a lifelong learner, and my grandmother showed me the importance of being patient, forgiving, and kind. My mother continued to inspire me with her own scientific accomplishments, and my father helped keep me focused on my work and my future.

Matthew Ryals
October 2018

Declaration

I submit that the experiments in the following study were performed by myself under the supervision of Lisa L. Cunningham, PhD at the National Institutes of Health. Assistance with experiments in this thesis was provided by the following individuals: Robert Morell PhD, Lindsey May, Daniel Martin PhD, Erich Boger PhD, Patricia Wu, Dave Raible PhD, Nora Welsh, Mike Kelley PhD, Matthew Kelley PhD, and Joseph Burns PhD. Sections 2.5, 3.5, and 4.5 detail their respective experimental contributions to the work presented in this thesis.

Table of Contents

Table of Figures

Table of Tables

Chapter 1: General Introduction

Introduction overview

To understand the experimental approach and vocabulary used in this study and outlined in this study, an introductory knowledge is required of the anatomy and physiology of the mammalian inner ear, drug-induced hearing loss, and the heat shock response. Thus, the intent of the Chapter 1 is to provide a sufficient amount of background information in each of these topics so that a reader will have sufficient background and context for each of the subsequent experimental chapters. The experimental chapters each contain introduction and discussion sections, which provide reintroductions to the rationale of the experiments performed and reinforce introductory concepts to explain any relevant experimental background information pertinent to that chapter.

1.1 Mammalian ear anatomy and physiology

1.1.1 Hearing and cochlear anatomy and physiology

In mammalian vertebrates, detection of sound (auditory) and balance (vestibular) information is crucial for the normal physiology of an organism, but the physiology behind each sensation is complex and involves several unique anatomical structures to function. For auditory processing, the first-order detection of sound performed by the ear relies on several steps in each major section of the ear: outer, middle, and inner ear. The outer ear, known as the pinna, is responsible for guiding sound pressure waves into the ear canal. Sound vibration is transferred through the hollow chamber of the middle ear by the vibration of the

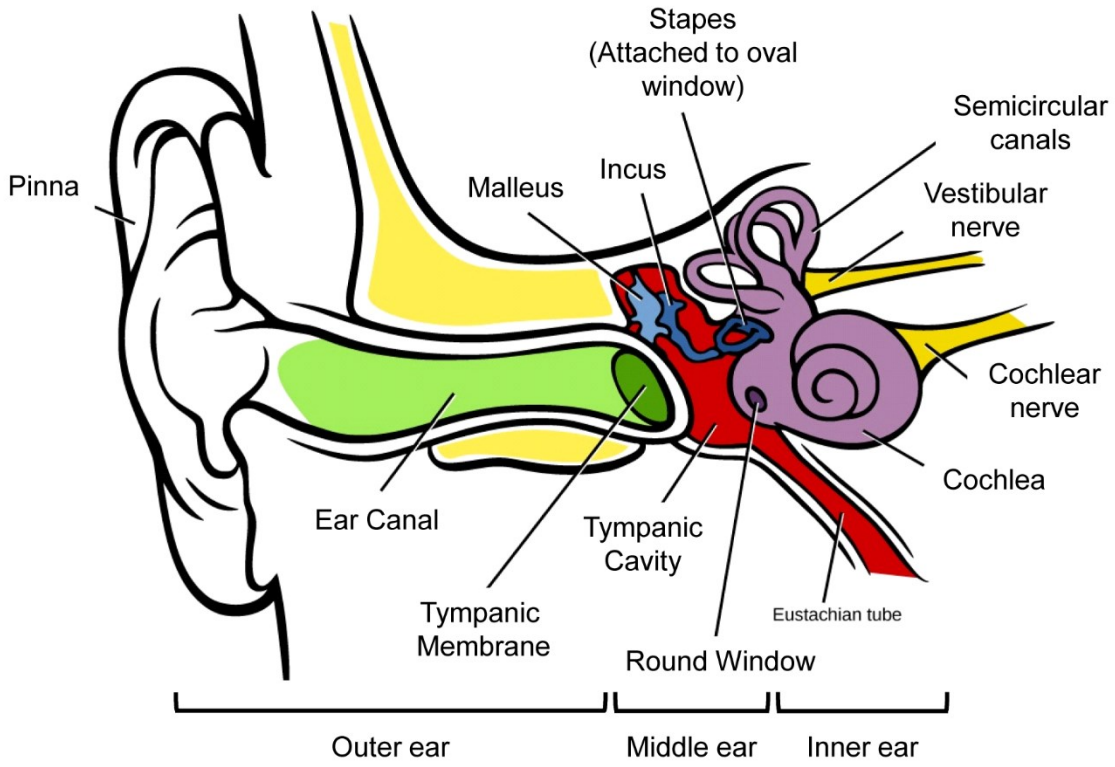

Figure 0.1 Illustration of the features of the outer, middle, and inner ear. Structures labeled in the figure are involved in the physiology of auditory and vestibular physiology. This figure was reproduced with minor modifications under Creative Commons Attribution License 4.0 license from (Avissar, Choi et al. 2013).

tympanic membrane, and the chain of small bones known as ossicles (the malleus, incus, and stapes). The ossicles and tympanic membrane provide an initial pressure gain of incoming sound pressure waves, and the stapes connects to the oval window membrane (LeMasurier and Gillespie 2005). The oval window opens into a fluid-filled structure called the cochlea, which is a region of the otic capsule within the temporal bone known as the bony labyrinth. The bony labyrinth contains three regions known as the cochlea, the vestibule, and the semicircular canals in which sit the sensory epithelia of the auditory and vestibular systems, correspondingly referred to as the membranous labyrinth (Hudspeth 1997, LeMasurier and Gillespie 2005, Khan and Chang 2013). Sitting inside the cochlear chamber, the organ of Corti is part of the membranous labyrinth and is the sensory organ responsible for the

detection of sound vibrations that pass from the oval window to the inner ear. Figure 1.1 illustrates the morphology and locations of the relevant structures of the outer, middle, and inner ear. The mechanical sound wave that enters from the oval window into the cochlea is converted into a standing wave within the fluid of the cochlea and ends at another membranous opening known as the round window. There are two important types of fluid within the cochlea, endolymph and perilymph. Perilymph fills two compartments of the cochlea, the scala tympani below the organ of Corti separated by a layer of tissue composed primarily of extracellular matrix proteins known as the basilar membrane, and the scala vestibuli separated above the organ of Corti by a thin layer of epithelium known as Reissner's membrane. The endolymph bathes the surface of the organ of Corti between the basilar and Reissner's membranes in a region known as the scala media. As discussed in section 1.1.3, the ionic composition of these fluids is integral to sound detection. Specialized sensory cells known as inner and outer hair cells detect the incoming standing wave using specialized microvilli known as stereocilia bundles through a process known as mechanotransduction (section 1.1.3). Hair cells are organized along the cochlear spiral of the organ of Corti, sitting on top of glia-like supporting cells on the basilar membrane in a tonotopic manner, meaning that they are arranged to detect specific frequencies of incoming standing wave vibrations that resonate at certain positions of the basilar membrane and vibrate the tectorial membrane, a collagenous structure sitting on top of the hair cells (Hudspeth 1997, LeMasurier and Gillespie 2005). Low frequency sound is detected at the widest, most flexible, apical portion of the basilar membrane, whereas high frequency sound is detected at the narrow, stiff, basal portion of the basilar membrane nearest the oval window. This tuning process, known as tonotopic mapping, occurs as the stiffness of the

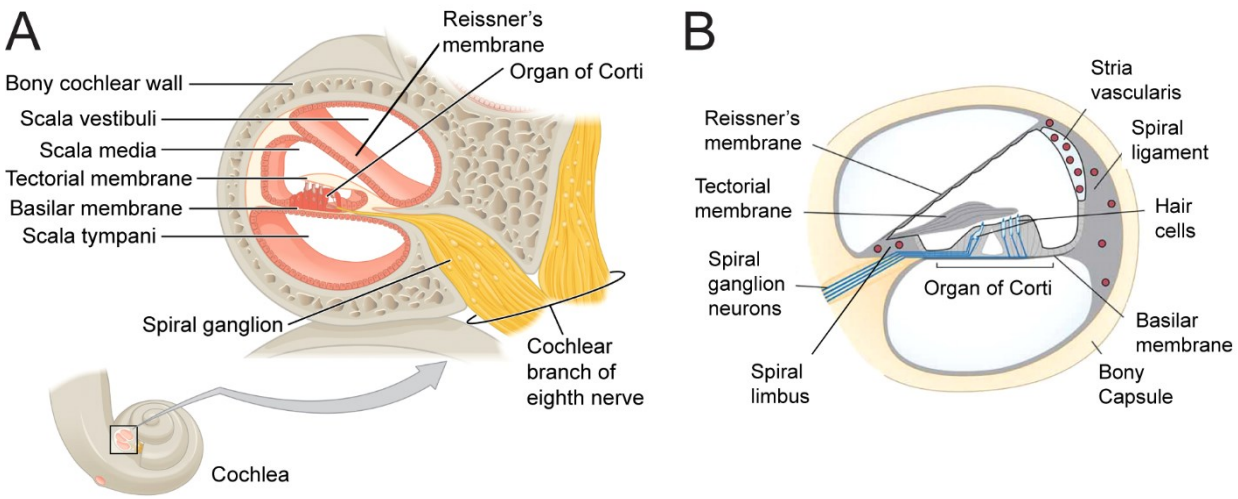

Figure 0.2 A) Illustration of a cross-section of the cochlear chamber. Structures labeled are relevant to sound detection in the cochlea. This image was reproduced with minor modifications under Creative Commons Attribution License 4.0 license from (Betts, Desaix et al. 2013). B) Detailed illustration of a cross-section of the organ of Corti. Additional structures relevant to maintenance of auditory function are labeled. Image reproduced with minor modification from (Jiang, Karasawa et al. 2017).

sensory epithelium varies, which allows vibrations of specific frequencies to travel to specific portions of the membrane, thereby mapping sound frequencies along the surface of the organ. Figure 1.2 illustrates the structure and features within the cochlear chamber and a detailed view of a cross-section of the organ of Corti. Once detected, hair cells transmit a signal to the primary neurons of the auditory system, the spiral ganglia neurons (SGNs). These neurons are in the center of the cochlear chamber and send dendritic projections outward to contact hair cells beneath the basilar membrane where they make synaptic connections with the hair cells. The axons of SGNs comprise the auditory fibers that spiral around the central soft, bony core of the cochlea known as the modiolus and becomes the cochlear (auditory) branch of the eighth cranial nerve (Berglund and Ryugo 1987). The ascending auditory pathway is then responsible for the subsequent integration and processing of auditory information from the eighth cranial nerve. Information is relayed to neurons in the pons in the ipsilateral cochlear nucleus in the brainstem and contralateral superior olivary

complex in the brainstem, where information converges into the inferior colliculus, the medial geniculate body, and the auditory cortex of the temporal lobe. Contralateral afferent projections (and descending efferent pathways into the inner ear) assist in sound localization and fine-tuning of hearing sensation based on the intensity and timing differences of an incoming sound as it reaches each ear (Hudspeth 1997) (reviewed in greater detail in (Dallos and Fay 2012)).

Other noteworthy anatomical features of the cochlea include the stria vascularis, the spiral ligament, the spiral limbus, and the inner and outer sulcus cells. The spiral limbus and spiral ligament represent the bony lining on the inside of the cochlear spiral, and the epithelial cell lining on the lateral bony wall of the cochlea, respectively. The cells of the inner and outer sulcus are the epithelial cells that sit in the organ of Corti between the spiral limbus and the outer spiral ligament. The stria vascularis is a specialized organ lining the outer region of the cochlea that maintains the ionic compositions of the perilymph and endolymph consisting of three cell layers: marginal cells, intermediate cells, and basal cells. The basal cells form extracellular tight junctions with the fibrocytes of the spiral ligament and selectively isolate the endolymphatic fluid within the scala media. These regions represent a selectively permeable border between the blood supply to the inner ear and the membranous labyrinth (Dallos 1992, Wangemann 2006, Dallos and Fay 2012).

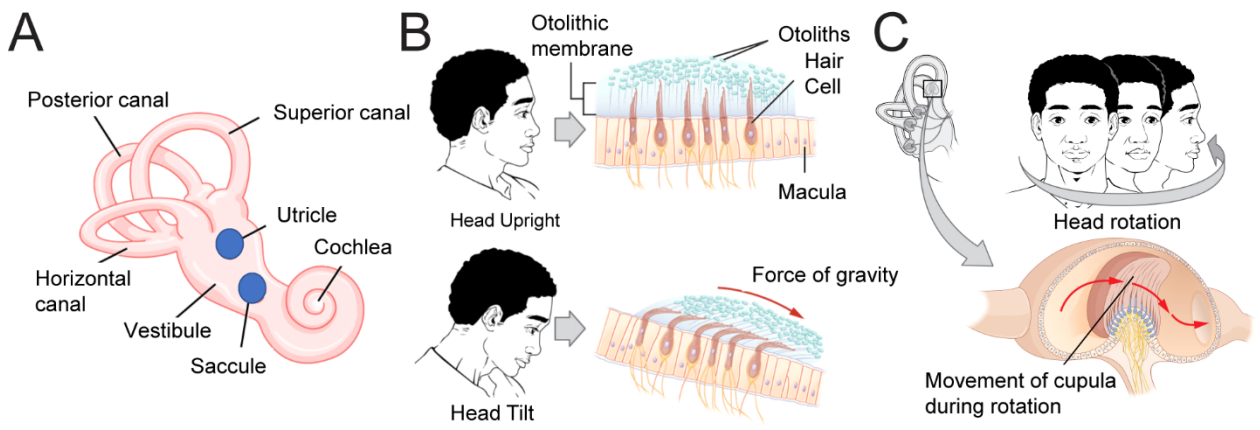

Figure 0.3 A) Illustration of the bony labyrinth with emphasis labeling on the vestibular organs (utricle and saccule positions highlighted in blue) and semicircular canals. This image was reproduced with minor modifications under Creative Commons Attribution License 4.0 license from (Avissar, Choi et al. 2013). B) Illustration demonstrating the physiology of the otolithic membrane displacing hair cell bundles in the utricle in response to linear acceleration of the head. C) Illustration demonstrating the physiology of the displacement of the cupula in response to head rotation, displacing hair cells bundles in the crista of the superior canal. Images in B and C were reproduced with minor modifications under Creative Commons Attribution License 4.0 license from (Betts, Desaix et al. 2013).

1.1.2 Vestibular anatomy and physiology

Vestibular information is detected by five separate organs in the inner ear: The saccule, utricle, and the three ampullae. The saccule and utricle both sit within the vestibule of the bony labyrinth and are responsible for the detection of gravity and linear acceleration of the head, respectively. The sensory epithelia of these organs, also referred to as the maculae, contain a layer of hair cells and underlying supporting cells much like the arrangement of the organ of Corti. On top of the macula is a layer of proteinaceous gel known as the otolithic membrane, embedded in which are crystals of calcium carbonate known as otoconia. Movement of the head causes the otolith membrane to shift, which the stereocilia bundles of hair cells in each macula can detect and transmit to vestibular ganglion neurons (VGNs) using mechanotransduction (section 1.1.3). Hair cells in the utricle are responsible for detecting motions in the horizontal plane, while those in the saccule are responsible for

motions in the vertical plane. The three semicircular canals (superior, posterior, and horizontal) correspond to the x, y, and z axes of three-dimensional space and are responsible for detecting rotational movements of the head. Each semicircular canal contains a sensory epithelium known as the crista ampullaris, and the hair cells within the cristae are embedded in a gel-like substance known as the cupula. Rotations of the head along each axis translate into movement of the cupula, which in turn are detected by hair cells in the cristae. Afferent signals from the cristae are also directed to VGNs, which project into the vestibular branch of the eighth cranial nerve and project to the vestibular nuclear complex of the brainstem (Lysakowski and Goldberg 2004, Khan and Chang 2013). Figure 1.3 illustrates the morphology of the utricle, saccule, and semicircular ampullae and the physiological detection of motion by these organs.

1.1.3 Cellular functions of inner ear hair and supporting cells

Hair cells of the auditory and vestibular systems represent highly-specialized sensory cells with several unique biological structures that allow them to effectively transduce incoming mechanical stimuli into neuroelectric signals that are sent to higher-order processing centers in the brain, a process known as mechanotransduction (Corey and Hudspeth 1979, Gillespie and Muller 2009). This process is made possible in both auditory and vestibular hair cells through utilization of specialized, modified bundles of microvilli located at their apical surface known as stereocilia. The stereocilia bundle consists of rows of microvilli arranged in a directional staircase in decreasing order of height. Each stereocilium consists of tightly-packed actin filaments at its core (Flock and Cheung 1977), surrounded by a variety of cross-linker proteins as well as myosin motor proteins, and grounded to the apical surface by a protein complex known as a rootlet (Fettiplace and Kim

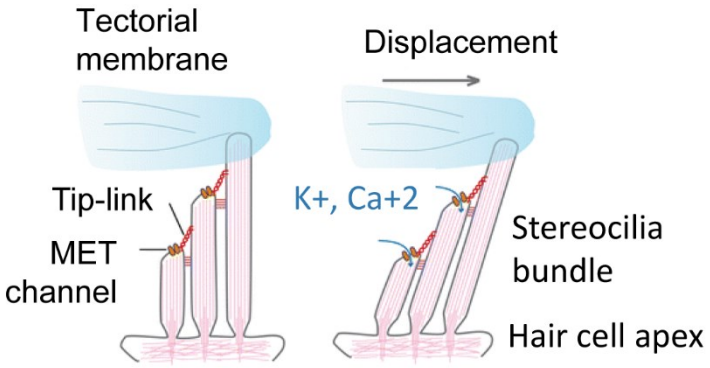

Figure 0.4 Illustration of mechanotransduction at the level of the stereocilia bundle. Labeled structures are important in the process of hair cell detection of a mechanical displacement with analogous processes occurring in both auditory and vestibular systems. Image reproduced with minor modification from (Michalski and Petit 2015).

2014). Beneath the apical surface of the hair cell, a rigid, actin-rich structure known as the cuticular plate holds the stereocilia bundle in place in conjunction with the rootlet (Michalski and Petit 2015). Highly-organized extracellular elements known as tip-links comprised of the proteins cadherin-23 (CDH23) and protocadherin-15 (PCDH15) (Kazmierczak, Sakaguchi et al. 2007) connect the tops of the rows of stereocilia to each other, acting in a spring-like manner to displace the rows of stereocilia when moved (Kachar, Parakkal et al. 2000). At the tips of the lower row of stereocilia are channels, known as mechanoelectric transduction (MET) channels, which are mechanosensitive, multiprotein channels with a pore protein in the center known as transmembrane channel-like 1 (TMC1) that allow for the passage of ions into the hair cell when opened (Kawashima, Geleoc et al. 2011, Pan, Akyuz et al. 2018). The endolymph fluid, which bathes the apical surfaces of hair cells in all inner ear sensory epithelia, contains a high potassium (K+) concentration relative to the perilymph, which is similar ionically to cerebrospinal fluid and has a higher concentration of sodium (Na+) (Corey and Hudspeth 1979). This high concentration of K+ in the scala media is primarily maintained by channel activity in the stria vascularis, which also maintains other

aspects of endolymph composition including bicarbonate/pH buffering; however, Reissner's membrane, the spiral ligament, and supporting cells of the organ of Corti are also involved in cycling K+ into the endolymph and Na+ into the perilymph (Wangemann 2006). Hair cell stereocilia are extremely sensitive to displacement, and upon displacement the tip link pulls each stereocilia, opening the MET channel, which in turn allows K+ into the hair cell, causing its depolarization, with attenuation control of the opened channel provided by Ca+2 influx (Gillespie and Walker 2001). Accordingly, deflection in the direction opposite the longest row of stereocilia will close the mechanotransduction channel, hyperpolarizing the hair cell. At the base of the hair cell are Ca+2-dependent channels, which open upon sufficient membrane depolarization. Influx of Ca+2 from perilymph into the base of the hair cells promotes neurotransmitter vesicle release to afferent synapses, completing the signal transduction process from the hair cell (Glowatzki and Fuchs 2002). Figure 1.4 illustrates the process of hair cell mechanotransduction.

In the organ of Corti, there are two major types of hair cells: inner hair cells (IHCs) and outer hair cells (OHCs). The IHCs form a single row of vase-shaped cells in the inner spiral of the organ of Corti. The stereocilia of IHCs lie in straight, consecutive rows and depolarize when deflected by the resonant vibration of the basilar membrane traveling through the endolymph (LeMasurier and Gillespie 2005). Once depolarized, the synaptic ribbons of IHCs release neurotransmitter vesicles primarily containing glutamate into the synaptic cleft. Ionotropic AMPA receptors expressed on the SGN postsynaptic processes are depolarized by this release and carry the depolarization signal up the eighth nerve (Ottersen, Takumi et al. 1998). The inner hair cells are the principle cells responsible for afferent transmission of incoming stimuli and receive most (roughly 95%) of SGN afferent inputs and are the primary

cells responsible for sound detection. OHCs are cylindrically-shaped and sit laterally to the IHCs and act as cochlear amplifiers to increase sensitivity and the frequency specificity of tonotopic mapping. The V-shaped stereocilia bundle of OHCs are attached to the tectorial membrane secreted by the spiral limbus (see Figure 1.2) that sits above the organ of Corti. OHCs are unique in that they are electromotile, meaning that their depolarization triggers a contractile motor protein (prestin, SLC26A5) (Zheng, Shen et al. 2000) in their cell membranes. The electromotive force generated by these cells enhances the vibrational movement of the basilar membrane and provides fine-tuning during frequency detection and discrimination (LeMasurier and Gillespie 2005).

In the vestibular maculae, there are also two types of hair cells known as type I and type II hair cells. Unique to mature vestibular hair cells is the presence of the kinocilium, which is a microtubule-based true cilium structure at the top of the stereocilia bundle that is embedded in the otolithic membrane. Kinocilia are displaced during the linear and rotational movements of the head, which in turn opens MET channels in these hair cells. In the utricle, type I hair cells have a wide, vase-like shape and are surrounded by large calyx-like afferent VGN synapses with irregular firing rates. Type II hair cells are more cylindrical and are connected to smaller afferent processes with faster, more regular firing rates. A similar system to the stria vascularis is found in the vestibule, where a layer of pigmented epithelial cells play a similar role in establishing an ionic environment essential for hair cells to mechanotransduce (Anniko and Wroblewski 1986). The orientation of the utricular hair cell stereocilia face towards a central line in the utricle known as the line of polarity reversal. Directly below the line of polarity reversal, there is a cellular region known as the striola, which is a region of lower cell density that runs through the middle of the macula in a

crescent shape. In the saccule, hair cell stereocilia face away from the line of polarity reversal, leading to orientations that allow for stimulation and inhibition of different populations of vestibular hair cells depending on the direction of head acceleration. The semicircular canals have similar layouts to ensure proper stimulation/inhibition of mechanotransduction in hair cells of the cristae (Khan and Chang 2013).

In addition to hair cells, the sensory epithelia of the inner ear contain other cell types that are important to the maintenance, structure, and function of these sensory end-organs. The major cell type in cochlear and vestibular sensory epithelia that surrounds the afferent projections of auditory and vestibular neurons and the hair cells are collectively known as 'supporting cells'. These cells share many functions and similarities to glial cells of the central nervous system, including expression of several common glial cell protein markers such as glutamate-aspartate transporter (GLAST, also known as Slc1a3) (Furness and Lehre 1997, Glowatzki, Cheng et al. 2006) and proteolipid protein 1 (PLP1) (Morris, Maklad et al. 2006). These cells play key roles in the normal functioning and homeostasis of the inner ear. Within the organ of Corti, supporting cells are traditionally divided into seven subtypes (Burns, Kelly et al. 2015) (reviewed in (Wan, Corfas et al. 2013)). Within the vestibular system, supporting cells are not morphologically divided into subtypes but serve the same cellular purposes as supporting cells in organ of Corti. Collectively, supporting cells are responsible for maintaining the fluid barrier at the apical surface of inner ear sensory epithelia, known as the reticular lamina. Supporting cells form tight junctions at cell-cell boundaries in the epithelial lumen of the reticular lamina, and also participate in K+ recycling in the endolymph that maintains the ionic separations that enable mechanotransduction as discussed in section 1.1.3 (Anniko and Wroblewski 1986, Wan,

Corfas et al. 2013). Supporting cells are also responsible for the clearance of glutamate from the synaptic space between hair cells and afferent neurons (Glowatzki, Cheng et al. 2006). In addition to these functions, supporting cells have important roles in determining the fate of apoptotic hair cells following injury or toxic insult. To protect the integrity of the endolymph-perilymph fluid boundary, supporting cells seal off dead hair cells by extruding the hair cell's stereocilia bundle with an actin-based ring structure that contracts around the apical portion of the hair cell. The hair cell corpse and cell debris is then phagocytosed by the neighboring supporting cell, and the lumen is preserved by a supporting cell scar consisting of tight cellular junctions over the area where the hair cell was located in the epithelium (Forge 1985, Bird, Daudet et al. 2010, Anttonen, Belevich et al. 2014, Monzack, May et al. 2015). Supporting cells are also involved in promoting auditory neuron survival following ototoxic exposure (Sugawara, Corfas et al. 2005) as well as during steady-state conditions by providing trophic support (Stankovic, Rio et al. 2004). Finally, although hair cells in the mature mammalian inner ear are terminally-differentiated, supporting cells in the vestibular organs can either mitotically divide and differentiate into hair cells or transdifferentiate into hair cells following damage; however, supporting cell transdifferentiation does not occur in the mature auditory system. Mammalian supporting cells lose the ability to mitotically divide and primarily utilize transdifferentiation to replace hair cells, but this phenomenon occurs only at very low levels in the vestibular sensory epithelia and does not result in meaningful improvement in vestibular function (Forge, Li et al. 1998, Wan, Corfas et al. 2013, Bucks, Cox et al. 2017, Burns and Stone 2017). For a more detailed discussion of supporting cell functions within the context of this study, refer to the introduction section of Chapter 2 (section 2.1).

1.1.4 Model systems for studying the inner ear

Experimental study of adult mammalian inner ear tissue is complicated by the fact that adult hair cells of the cochlea do not survive in culture. Neonatal hair cells can survive in culture, but this limits the ability to study adult mammalian cochlear hair cells *in vitro*. Numerous model systems have been developed by researchers to understand hair cell function, and in this study the predominant model system used is the *in vitro* culture of utricle explants from adult mice. Unlike cochlear hair cells, the hair cells of the utricle can survive in culture for several days, and therefore represent a tractable means of studying the activity and responses of mature hair cells. Furthermore, the mouse utricle explant model has a well-characterized method of dissection and isolation out of the bony labyrinth, and has been developed as a tractable means of investigating hair cell homeostasis, death, and survival (Forge and Li 2000, Cunningham, Cheng et al. 2002, Cunningham, Matsui et al. 2004, Cunningham 2006, Kesser, Hashisaki et al. 2007, Brandon, Voelkel-Johnson et al. 2012, Bucks, Cox et al. 2017). Section 3.1 discusses inner ear model systems as they pertain to this study in greater detail.

1.2 Drug-induced hearing loss and cell death

1.2.1 Aminoglycoside ototoxicity

Hair cells are sensitive to a variety of stressors, including aging, traumatic noise, and ototoxic drugs, the two main classes of which are aminoglycoside antibiotics and the anticancer drug cisplatin. Produced naturally in the soil by actinomycete fungi, the first

aminoglycoside to be isolated was streptomycin in 1944 (Schatz, Bugle et al. 1944), which was subsequently used clinically in the treatment of tuberculosis (Hinshaw, Feldman et al. 1946). Aminoglycoside antibiotics are used in modern day as a broad-spectrum antibiotic to treat gram negative bacterial infections ranging from neonatal sepsis to *Pseudomonas* bacterial respiratory infections (especially in in patients with cystic fibrosis) to multi drug-resistant tuberculosis infections (Schacht 1998, Forge and Schacht 2000). Commonly-used aminoglycoside antibiotics in clinical practice include gentamicin, kanamycin, and amikacin (Forge and Schacht 2000). Because of their efficacy in a range of infections, clinical reliance on aminoglycosides remains highly relevant, with increasing reliance on these drugs to treat multidrug-resistant tuberculosis and other drug-resistant bacterial infections (Schacht 1998, Forge and Schacht 2000, Houghton, Green et al. 2010, Takahashi and Igarashi 2017). Ongoing research aims to create liposomal formulations to improve drug delivery as well as develop novel aminoglycosides and co-treatments to reduce bacterial resistance to aminoglycosides themselves (Pagkalis, Mantadakis et al. 2011, Takahashi and Igarashi 2017). The observation that aminoglycosides interfere with the lifecycle of the human immunodeficiency virus (HIV) introduces the possibility for their use in treating HIV infections (Houghton, Green et al. 2010). Additionally, aminoglycosides can induce read-through of premature termination codons (PTCs) in mammalian genes, which are present in over 1800 human genetic disorders and result in truncated proteins. The development of aminoglycosides to treat PTC-related disorders is also an active field of research (Boulikas and Vougiouka 2004, Houghton, Green et al. 2010).

Molecularly, aminoglycosides are highly-cationic compounds consisting of two to three cyclitol-sugar rings to which numerous amino group moieties are attached (Forge and

Schacht 2000, Shakil, Khan et al. 2008). These positively-charged groups preferentially bind to negatively-charged bacterial cell outer membranes and disrupt and upon uptake into bacteria bind to ribosomal 16S RNA, which is a component of the 30S small subunit of the bacterial ribosome. These effects inhibit bacterial growth primarily by interfering with the elongation phase of nascent proteins during bacterial protein translation and also by disrupting the bacterial outer cell membrane (Jana and Deb 2006, Shakil, Khan et al. 2008), ultimately killing the bacteria. The major side effects associated with aminoglycosides include ototoxicity and nephrotoxicity. While the nephrotoxicity associated with these drugs is reversible, the hearing and vestibular damage is not, because cochlear hair cell death induced by ototoxins results in permanent damage to the sensory epithelium, as hair cells are post-mitotic and do not regenerate (Lowenheim, Furness et al. 1999, Chen, Zindy et al. 2003). Clinically-relevant ototoxicity has been observed in roughly 20% in children with cystic fibrosis receiving aminoglycosides to treat respiratory infections (Al-Malky, Dawson et al. 2015) and in roughly 50% of patients receiving either amikacin or kanamycin for the treatment of multidrug-resistant tuberculosis (Sagwa, Ruswa et al. 2015). Additional studies of aminoglycoside ototoxicity show clinical symptoms within approximately 10-20% of patients given these drugs (Moore, Smith et al. 1984, Lerner, Schmitt et al. 1986). Ototoxicity in the cochlea results in permanent, high-frequency, symmetrical bilateral hearing loss (Forge and Schacht 2000, Guthrie 2008), whereas ototoxic damage to the vestibular system results in unsteadiness and oscillopsia (loss of vestibular-ocular reflex), which causes incorrect perceptions of movement in objects during head turning motions (Forge and Schacht 2000, Guthrie 2008). Interestingly, the vestibular hypofunction is sometimes reversible, in contrast to the permanent hearing loss effect (Guthrie 2008).

The cellular and molecular mechanisms underlying aminoglycoside-induced ototoxicity have been partially characterized. Following systemic administration, aminoglycosides enter the cochlea through the blood-labyrinth barrier, where they pass through the marginal cells of the stria vascularis into the endolymph (Wang and Steyger 2009). While aminoglycosides are also capable of entering the perilymph, current uptake hypotheses suggest ototoxic uptake occurs primarily though endolymphatic-trafficked aminoglycosides (Wang and Steyger 2009, Li and Steyger 2011). Aminoglycosides can be taken up by SGNs and appear to cause some cell death and damage to afferent connections to inner hair cells (Oishi, Duscha et al. 2015). Morphological thinning and reducing in marginal cell numbers of the stria vascularis also occurs following aminoglycoside exposure (Forge, Wright et al. 1987). However, most damage and cell death caused by aminoglycosides in inner ear tissue is localized primarily to hair cells, although the precise mechanism behind the susceptibility of hair cells to aminoglycosides remains a topic of active research. Aminoglycosides are thought to primarily enter hair cells through MET channels (Marcotti, van Netten et al. 2005, Li and Steyger 2011) and secondarily through endocytosis at the apical surface of the cell (Hashino and Shero 1995) or transient receptor potential (TRP) channels (Stepanyan, Indzhykulian et al. 2011). The acute response to aminoglycoside exposure in hair cells is the generation of intracellular reactive oxygen species (ROS) (Hirose, Hockenbery et al. 1997, Forge and Schacht 2000, Choung, Taura et al. 2009), among which are highly-reactive molecules such as free hydroxyl radicals and peroxynitrite capable of peroxidizing lipid molecules, damaging DNA through oxidation reactions, and interfering with Ca^{+2} cell membrane channels (Choung, Taura et al. 2009). Aminoglycosides are thought to produce ROS by reacting with iron within the cell and catalyzing the oxidization of unsaturated fatty acids (Sha and Schacht

1999, Lesniak, Pecoraro et al. 2005). ROS can directly activate cell death pathways that trigger programmed cell death (apoptosis) including p38 mitogen-activated protein kinase (MAPK) c-Jun N-terminal kinase (JNK) signaling (Eshraghi, Wang et al. 2007, Coffin, Williamson et al. 2013). These signaling pathways result in the induction of caspases, loss of mitochondrial membrane potential, and cytochrome c release from mitochondria and ultimately leading to chromatin condensation and fragmentation of DNA, both of which hallmarks of classical apoptosis as the dead cell degrades (Forge and Schacht 2000). In addition, non-apoptotic, necrotic cell death pathways through activation of calpains and cathepsin D have also been shown to be activated by chronic aminoglycoside exposure in hair cells (Jiang, Sha et al. 2006, Park, Lee et al. 2012). In the cochlea, outer hair cells show more susceptibility to aminoglycoside ototoxicity than inner hair cells. Furthermore, basal outer hair cells show increased susceptibility to aminoglycoside ototoxicity compared to apical outer hair cells, although with increasing dose, more apically located outer hair cells as well as inner hair cells degenerate, expanding the frequency range of the hearing loss (Ryan and Dallos 1975, Forge and Schacht 2000). In the vestibular system, striolar hair cells and hair cells of the apical portions of the cristae are more susceptible to aminoglycoside-induced ototoxicity compared to the peripheral regions of the tissue, but similarly to the cochlea, the lesion will extend into the peripheral macula with increased aminoglycoside dosage and application (Forge and Li 2000). Thus, aminoglycosides represent a lifesaving class of medicines with a need for better understanding of how to prevent the complex and prominent side effect of ototoxicity.

1.2.2 Cisplatin ototoxicity

Cisplatin is used as a first-line treatment for a wide range of head and neck cancers, and for use in lung, bladder, testicular epithelial cancers. More advanced, metastatic cancers of the breast and prostate are also sometimes treated with cisplatin as well as malignant gliomas, melanomas, and mesothelioma (Boulikas and Vougiouka 2004, Schacht, Talaska et al. 2012). Although cisplatin was originally discovered in 1845, its utility as an antineoplastic agent was not identified until 1965, when platinum electrolytic byproducts were observed to inhibit bacterial cell division, and later cisplatin was shown to specifically inhibit tumor growth in animal models (Rosenberg, Vancamp et al. 1965, Rosenberg, VanCamp et al. 1969). It was approved by the FDA for use in human cancers in 1978 (Gomez-Ruiz, Maksimovic-Ivanic et al. 2012).

Cisplatin is a simple coordination complex molecule that contains at its center a platinum atom with two chloride ligands and two amino ligands arranged in a *cis* configuration (Rozencweig, von Hoff et al. 1977). In cells, cisplatin promotes cell death by forming covalent adducts with nuclear DNA, resulting in crosslinked DNA strands (either intra- or inter-stranded). These crosslinks are detected by DNA damage response proteins, which aggregate over the crosslink, promote apoptosis via the tumor-suppressor protein p53, and halt transcription of RNA (Schacht, Talaska et al. 2012). Cell death induced by cisplatin tends to target cells that are undergoing mitosis because of the relative ease of access to accessible DNA binding in these cells, making it effective for targeting rapidly-dividing cancer cells and leading to G2 cell cycle arrest.

The side effect profile of cisplatin involves nephrotoxicity and ototoxicity, as well as peripheral neuropathy including tingling and numbness, nausea and myelosuppression

(Grunberg, Sonka et al. 1989, Schacht, Talaska et al. 2012). Cisplatin is the most ototoxic drug in clinical use. Clinical symptoms of ototoxicity in patients taking cisplatin has an incidence as high as 75-100% (McKeage 1995), and damage can be delayed or worsen for several years following treatment. Similar to aminoglycoside ototoxicity, cisplatin-induced hearing loss begins in the high-frequency range of hearing and can extend into lower frequencies with increased dose, is permanent, bilateral, and often associated with sensations of tinnitus (McKeage 1995). Vestibular toxicity is less frequently observed, and often involves transient sensation of dizziness accompanied by nystagmus (Kobayashi, Ohashi et al. 1987). Organometallic analogues of cisplatin have been developed with milder adverse event profiles, such as carboplatin and oxaliplatin, but these drugs are also less effective chemotherapeutics than cisplatin when compared at similar doses (McKeage 1995, Schacht, Talaska et al. 2012).

The mechanisms underlying cisplatin ototoxicity share some features with aminoglycoside ototoxicity, but also have several unique features. The exact mechanism for cisplatin entering the inner ear has not been fully elucidated; however, promising information emerging regarding cisplatin's mechanism of entry suggests that it enters the cochlea from the bloodstream via the stria vascularis (van Ruijven, de Groot et al. 2005, Karasawa and Steyger 2015), where the platinum is retained long-term, allowing for progressive damage to inner ear tissue over time (Breglio, Rusheen et al. 2017). After passing through the blood labyrinth barrier, cisplatin may enter cells through solute carrier channels, of which influx copper transporter 1 (CTR1) has been shown to be highly expressed in outer hair cells and is necessary for their uptake of cisplatin (More, Akil et al. 2010). In addition, organic copper transport channel 2 (OCT2), which has been shown to be necessary for both cisplatin-

induced ototoxicity and nephrotoxicity and expressed in cochlear hair cells as well as renal proximal tubular cells, may also play a role in cisplatin uptake (Ciarimboli, Deuster et al. 2010). Acute cisplatin exposure in hair cells results in formation of ROS, specifically superoxide (O_2^-). ROS generation by cisplatin occurs primarily through induced activity of NADPH oxidase 3 (NOX3) (Banfi, Malgrange et al. 2004, Mukherjea, Jajoo et al. 2010), which is a protein expressed in the inner ear normally involved in cell signaling and also is involved in otolith formation (Lundberg, Xu et al. 2015). ROS-mediated depletion of antioxidant enzymes such as glutathione reductase and superoxide dismutase as well as ROS production triggers apoptotic signaling via p53 and is mediated by initiator/executioner caspases 3 and 9 (CASP3/9) as evidenced by hair cell expression of classical downstream apoptotic markers BAX, BCL-2 proteins, DNA fragmentation, and condensed nuclei both *in vitro* and *in vivo* (Alam, Ikeda et al. 2000, Watanabe, Inai et al. 2003, Benkafadar, Menardo et al. 2017); however, necrotic cell death processes involving expression of inflammatory cytokines such as tumor necrosis factor alpha (TNFα) may also play a role in cisplatin-mediated hair cell death (Previati, Lanzoni et al. 2007, So, Kim et al. 2007). In accordance with the observed hearing loss as with aminoglycosides, hair cell loss begins at the base of the cochlea and extends into the apex with increasing dose and exposure to cisplatin. Cochlear outer hair cells are more susceptible to death than inner hair cells, dependent both on basal/apical position and dose of cisplatin. In contrast to aminoglycoside-induced ototoxicity, which is primarily restricted to hair cell death, the damage caused by cisplatin adversely affects several regions of the inner ear. SGNs, intermediate and marginal cells of the stria vascularis, and fibrocytes of the spiral ligament all undergo cell death following cisplatin exposure resulting in degeneration of their respective cochlear structures

(Watanabe, Inai et al. 2003, Liang, Schulte et al. 2005, van Ruijven, de Groot et al. 2005, Schacht, Talaska et al. 2012). Uniquely following cisplatin exposure, the ability of the supporting cells to phagocytize dead and dying hair cells as described in section 1.1.3 is also disrupted, resulting in cell debris and 'corpse'-like hair cell remnants left in sensory epithelia of the inner ear (Monzack, May et al. 2015). Interestingly, although cisplatin does kill vestibular hair cells *in vitro* primarily through p53-dependent apoptosis (Lundberg, Xu et al. 2015), *in vivo* vestibular hair cell death following cisplatin exposure is minimal (Schacht, Talaska et al. 2012). Although not directly examined in this study, cisplatin ototoxicity is a subject of intense research worth noting as it is one of the predominant drugs involved in drug-induced ototoxicity besides aminoglycosides. Importantly, recent clinical trials have revealed a reduction in cisplatin ototoxicity in patients given the inorganic molecule sodium thiosulfate as a co-therapy during cisplatin treatment (Freyer, Chen et al. 2017, Brock, Maibach et al. 2018).

1.2.3 Ototoxin-induced disruption of hair cell protein translation

One interesting recent observation is that both major classes of ototoxic drugs appear to directly affect translation in hair cells, suggesting that perhaps a shared underlying feature in hair cell susceptibility to these drugs be related to their ability to perturb protein homeostasis. Hair cells also have unique protein trafficking due to the presence of their stereocilia bundles. Unique translational properties have also been observed in hair cells with respect to ototoxicity and stereocilia protein turnover, as discussed in the discussion section of Chapter 1: "Incorporation of click-chemistry-tagged amino acids into newly synthesized proteins revealed that the level of protein synthesis is lower in hair cells compared to supporting cells (Francis, Katz et al. 2013). Mature mammalian utricular hair cells also have low turnover of

proteins in stereocilia bundles as measured by incorporation of ^{15}N-containing amino acids using multi-isotope mass spectrometry (MIMS), and although cytoplasmic protein turnover and turnover at stereocilia tips was higher than in the stereocilia shaft in hair cells, this suggests that hair cells by extension could have altered regulation of proteostasis (Zhang, Piazza et al. 2012)…Using the click-chemistry incorporation of tagged amino acids, translation in mouse utricular and cochlear hair cells was specifically decreased upon exposure to ototoxic aminoglycoside antibiotics, and others have demonstrated inhibition of translation or protein synthesis in mouse cochlear explants upon exposure to cisplatin (Francis, Katz et al. 2013, Nicholas, Francis et al. 2017)." At a mechanistic level, it has been suggested the crucial susceptibility to ototoxins such as cisplatin and aminoglycosides may be the ability for hair cells (particularly basal cochlear hair cells) to cope with ROS (Sha, Taylor et al. 2001); however, evidence of differences in protein turnover presented above combined with the altered translational abilities of other ciliated cell types presents a higher-order cell type difference between hair cells and supporting cells, suggesting hair cells may be extremely sensitive to external perturbations of protein synthesis. ROS generation may be only one acute-level side effect of this fundamental cellular attribute of translational sensitivity.

1.3 The heat shock response

1.3.1 Mammalian cellular response to heat stress and heat shock proteins

The ability of a living cell to respond to elevated temperatures is one of the oldest and most fundamental biological response pathways available to all organisms from all three

domains of life: bacteria, archaea, and eukarya. In animal models, the heat shock response (HSR) was originally observed in fly (*Drosophila*) larvae in 1962 when it was noted that puffs in the large chromosomes of the salivary gland were produced following heat exposure (Ritossa 1962). The HSR was subsequently characterized in terms of protein and messenger RNA (mRNA) production (Tissieres, Mitchell et al. 1974, Moran, Mirault et al. 1978). As the understanding of the HSR progressed, the protective effect of HSR against cell death during sustained elevated temperatures, and the protective effect of HSR-induced proteins against cell death was noted in other eukaryotic systems such as mammalian cell lines (Sapareto, Hopwood et al. 1978) and yeasts (McAlister and Finkelstein 1980) (further reviewed in (Daugaard, Rohde et al. 2007)). Further research demonstrated that the HSR resulted in stabilization of thermally denatured proteins, and reduction in components of the apoptotic signaling processes and that these functions were mediated by heat shock proteins (HSPs) (Ananthan, Goldberg et al. 1986) (reviewed in (Garrido, Gurbuxani et al. 2001)).

HSPs are the largest family of genes induced by heat stress. They are proteins that perform several key roles in cellular homeostasis as well as in conditions of cellular stress. The common normal cellular function of most HSPs is their ability to act as molecular chaperones, binding to and assisting in re-forming the shape and function of unfolded proteins. Originally, the induction of HSPs was identified following heat stress, but over time these proteins have been shown to be induced in response to a variety of stressors including free radical oxidation from sources such as UV light, wound healing, or heavy metal exposure (Gabai, Meriin et al. 1997, Morimoto 1998). The induction process relies on the activity of transcription factors known as heat shock factors, of which heat shock factor 1 (HSF1) is common to most vertebrates (reviewed in (Pirkkala, Nykanen et al. 2001)). The

HSP family itself includes 5 broad HSP classes: 1) HSP100s, 2) HSP90s, 3) HSP70s, 4) HSP60s, and 5) the small HSPs (sHSPs). These classes are separated based on the molecular weight and structure of each group of HSPs (e.g. HSP90s are a class of proteins that are approximately 90 kDa in weight with similar structural motifs, whereas sHSPs are those with molecular weights between 10-40 kDa) (Richter, Haslbeck et al. 2010, Jee 2016). Although protection effects from several members of the HSP classes have been observed, one of the most robustly-induced HSP family members in response to heat shock are the HSP70 proteins. HSP70 proteins consist of both inducible and constitutive forms, with several HSP70 homologous genes present in mammalian cells that localize to cytoplasm, the endoplasmic reticulum, mitochondria, and the nucleus (Daugaard, Rohde et al. 2007). In this study, we will be focusing primarily on two highly-related, stress-inducible cytoplasmic members of the HSP70 family, known as HSP70A1A and HSP70A1B, which are encoded by single-exon genes *Hspa1a* and *Hspa1b*, respectively. HSP70 proteins reversibly bind and assist in protein folding and re-folding of disorganized proteins. They can promote recruitment of proteasomal degradation machinery or lysosomal autophagy of proteins that are too badly denatured to re-fold properly (Hartl, Bracher et al. 2011). HSP70 also has several anti-apoptotic activities in both the early and late phases of apoptosis, including prevention of JNK/p38 MAPK signaling (Gabai, Meriin et al. 1997), reduction of mitochondrial permeability pores through inhibition of proapoptotic Bcl-2 family proteins (Stankiewicz, Lachapelle et al. 2005) thereby preventing cytochrome c release, and further in apoptotic signaling cascade, the inhibition of apoptosome, preventing binding of initiator CASP9 for downstream apoptotic signaling of CASP3 (Beere, Wolf et al. 2000, Li, Lee et al. 2000).

1.3.2 Heat shock in the inner ear

The HSR, and specifically the induction of stress-related HSPs or related stress-inducible proteins has been found to be protective against ototoxic damage in the inner ear. Briefly, a nonlethal heat shock preconditioning stimulus is protective against aminoglycoside- and cisplatin-induced hair cell death in cultured mouse utricles *in vitro* (Cunningham and Brandon 2006), and inducible HSP70 is required for this effect, which is lost in utricles from HSP70 knockout mice (Taleb, Brandon et al. 2008). Furthermore, HSP70-overexpressing mice are protected against hearing loss and cochlear hair cell death *in vivo* following exposure to aminoglycosides (Taleb, Brandon et al. 2009). Several lines of evidence exist to suggest that this protective effect may be non-cell autonomous. Namely, after heat shock inducible HSP70 is localized immunohistochemically in supporting cells in cultured mouse utricles *in vitro*, and adenoviral infection of supporting cells with HSP70 protects hair cells against aminoglycoside ototoxicity in vitro, both of which suggest that supporting cells may mediate the protective effect of HSP70. Furthermore, hair cells are protected from aminoglycoside ototoxicity in cultured mouse utricles by either exogenous application of HSP70 or by sharing media (co-culture) with heat shocked utricles, suggesting that there may be a distal signaling component to HSP70-mediated protective of hair cells (May, Kramarenko et al. 2013). Finally, IHCs and hearing function were protected *in vivo* in cochleae of mice exposed to systemic aminoglycosides when supporting cells were infected with adenovirus containing HSP70 with a fluorescent reporter tag (Takada, Takada et al. 2015), suggesting that supporting cell expression of HSP70 is also protective to hair cells in the cochlea (see section 4.1.1). While these studies have identified protective effects of

HSPs in the inner ear, no information currently exists on the cell-specific pattern of expression of HSPs after heat shock at the transcriptional level.

1.4 Hypotheses and specific aims

This introduction has presented background regarding the biological complexity of the inner ear, the issue of drug-induced ototoxicity, and the protective potential of heat shock against hair cell death. Heat shock is a means of protecting highly specialized, particularly fragile hair cells against ototoxicity, and prior research suggests that the multi-purposed supporting cells may mediate this effect. The research focus of this study aims to take a step similar to the initial steps taken to elucidate and validate the protective mechanisms of the HSR, to characterize the cell-specific transcriptomes and heat shock-induced transcriptomes in the sensory epithelia cells of the inner ear. Given the information about ototoxicity and heat shock introduced in sections 1.1-1.3, this study proposes the following specific hypotheses:

Hypothesis 1: Differential gene expression analysis of cell-type-specific and single-cell transcriptome data will reveal the transcriptional signature(s) of the protective heat shock responses in sensory hair cells and glia-like supporting cells.

Hypothesis 2: Alignment of the inner ear heat shock transcriptional signature to a gene expression database will reveal compounds capable of pharmacologically mimicking the otoprotective heat shock response. These compounds will be efficacious in protecting hair cells against drug-induced ototoxicity. By testing the gene expression signature induced by these compounds as well as the compounds' ability to protect against

ototoxicity, protective properties of the heat shock transcriptional signature will be revealed.

To address the proposed hypotheses above, three specific aims were developed:

Specific Aim 1: Determine the transcriptional profile of the heat shocked utricle at the resolution of whole tissue, cell population, and single-cell transcriptomes. Analyze and validate the differentially-expressed genes within cell type-specific populations to determine their differential responses to heat shock.

Specific Aim 2: Identify compounds ("perturbagens") that induce a cellular consensus transcriptional signature that mimics the utricle heat shock response. Prioritize these perturbagens based on criteria that include existing literature information, analysis of perturbagen rank data, tissue viability testing, gene expression, and feasibility of clinical use.

Specific Aim 3: Determine the extent to which the identified perturbagens can effectively mimic heat shock by preventing ototoxic drug-induced hair cell death in inner ear tissue explants.

Chapter 2: RiboTag RNA-Seq of heat shocked utricles

2.1 Introduction

The inner ear contains several highly specialized sensory epithelia that are responsible for auditory and vestibular functions. Each epithelium contains mechanosensory cells known as hair cells (HCs) that detect and transduce external sound and positional information. Surrounding the HCs in each sensory epithelium are glia-like cells collectively referred to as supporting cells (SCs). Supporting cells serve a variety of functions, including functional and structural support, clearance of extracellular debris and dying hair cells, and formation of scars to seal the epithelial lumen after hair cell death (Forge 1985, Abrashkin, Izumikawa et al. 2006, Anttonen, Belevich et al. 2014, Monzack, May et al. 2015). SCs also perform other glial cell-like functions including providing trophic support to neurons through release of brain-derived neurotrophic factor (BDNF) and neurotrophin-3 (NT-3) (Montcouquiol, Valat et al. 1998, Sugawara, Murtie et al. 2007), and the clearance of neurotransmitter from the synaptic cleft between HCs and primary afferent neurons (Glowatzki, Cheng et al. 2006). Together these functions of SCs effectively allow HCs to maintain viable, steady-state mechanotransduction and synaptic function. In both the auditory and vestibular systems, the stromal tissue beneath the sensory epithelium contains resident tissue macrophages as well as bone marrow-derived macrophages identified by macrophage markers (CX3CR1, IBA1) (Okano, Nakagawa et al. 2008, Sato, Shick et al. 2010). These cells migrate to the sensory epithelium to assist SCs in phagocytizing dead and dying HCs and cellular debris following hair cell death (Kaur, Hirose et al. 2015, Hirose, Rutherford et al. 2017).

Hair cells, supporting cells, and resident macrophages have differential responses to stresses. For example, hair cells are more susceptible than supporting cells to damaging stimulation, including ototoxic drugs and noise damage. Similarly, these cell types demonstrate differential responses to protective stimulation, including induction of heat shock proteins (HSPs). We showed previously that heat shock induces HSPs in the mouse utricle ex vivo, and this HSP induction protects against ototoxic drug-induced hair cell death (Cunningham and Brandon 2006, Taleb, Brandon et al. 2008). We further investigated this effect and found that HSP70 expression is both necessary and sufficient for this protective effect (Taleb, Brandon et al. 2009, Baker, Roy et al. 2015). In response to heat shock, we observe robust induction of HSP70 immunoreactivity in SCs with little induction in HCs (May, Kramarenko et al. 2013). Similarly, pharmacological induction of heme oxygenase-1 (Hmox1, also called Heat Shock Protein 32, HSP32) protects against both aminoglycoside- and cisplatin-induced hair cell death (Francis, Kramarenko et al. 2011, Baker, Roy et al. 2015), but HMOX1 immunoreactivity is observed in resident macrophages in the underlying stroma of the utricle, but not in HCs or SCs (Baker, Roy et al. 2015). Thus, HSP-mediated protection is non-cell autonomous in the inner ear (Francis and Cunningham 2017). To better understand the full range of cell-type-specific responses to heat stress and to determine whether these differential responses are transcriptionally regulated, we performed cell-type-specific transcriptional profiling of these cell types in response to heat shock.

Several methods of generating cell-type-specific transcriptional profiles have been used in the inner ear, including FACS-sorting of dissociated, fluorescently labeled cells (Tao and Segil 2015, Hickox, Wong et al. 2017) and single-cell capture (Burns, Kelly et al. 2015) followed by RNA-Seq or mass spectrometry. Each of these techniques requires dissociation

of the sensory epithelium, which could potentially alter gene expression and induce stress response genes such as HSPs (van den Brink, Sage et al. 2017). To avoid the cellular stress caused by dissociation, we utilized the RiboTag approach (Sanz, Yang et al. 2009). This approach utilizes a transgenic mouse that bears a floxed hemagglutinin (HA) tag in the *Rpl22* ribosomal protein locus. Cell-type specificity of the RiboTag is achieved using a Cre driver that results in recombination in the cells of interest. This method then allows isolation of cell-specific transcripts via immunoprecipitation (IP) of the HA-tagged ribosomal subunit RPL22. RNA isolated from the IP can then be sequenced to reveal the transcripts captured from that cell type of interest. This technique has been used previously to study the transcriptomes of other difficult-to-isolate cell types such as Sertoli cells in the mouse testis and hair cells in zebrafish, and it has been shown to avoid the induction of immediate early genes (De Gendt, Verhoeven et al. 2014, Matern, Beirl et al. 2018).

Because the RiboTag system relies on Cre recombination for generation of the HA-RPL22 protein, two Cre lines were selected for this study. GFI1 is a protein involved in HC development and survival, and the Gfi1-Cre mouse (Yang, Gan et al. 2010) expresses Cre in HCs of inner ear epithelia (Matern, Vijayakumar et al. 2017). Gfi1-Cre has been used to drive fluorescent protein expression in HCs, to isolate neonatal utricle HCs for single-cell RNA-Seq analysis (Burns, Kelly et al. 2015), and to drive expression of genetic markers of HC development (Liu, Dearman et al. 2012). Special consideration of which Cre line to use to isolate utricle SCs was necessary, because SCs share a common progenitor with HCs (Lanford, Lan et al. 1999), and SCs retain a limited ability to transdifferentiate into HCs (White, Doetzlhofer et al. 2006, Lin, Golub et al. 2011), especially in the utricle (Bucks, Cox et al. 2017). Therefore, we used an inducible Cre model for SCs to allow for Cre induction

in mature SCs. GLAST (SLC1A3) is a glutamate transporter expressed in juvenile and adult SCs (Jin, Kikuchi et al. 2003, Glowatzki, Cheng et al. 2006, Dalet, Bonsacquet et al. 2012). The GLAST-CreER mouse bears a tamoxifen-inducible Cre transgene (Wang, Rattner et al. 2012), and it has been used to study the inner phalangeal SCs of the cochlea (Mellado Lagarde, Wan et al. 2014) and has also been characterized in supporting cells in adult mouse utricles (Stone, Wisner et al. 2018). We combined the RiboTag mouse with the Gfi1-Cre or GLAST-CreER lines to obtain cell type-specific transcripts from control and heat shocked utricles, and we used RNA-Seq to discover the transcriptional responses of each cell type to heat shock.

2.2 Methods

2.2.1 Mouse breeding, organotypic utricle culture, heat shock stimulation

Gfi1-Cre (*Gfi1*$^{tm1(cre)\text{Gan}}$) mice were generated by Dr. Lin Gan at U. Rochester, and they were generously provided for this study by Dr. Joseph C. Burns and Dr. Matthew W. Kelley, Laboratory of Cochlear Development, National Institute on Deafness and Other Communications Disorders. GLAST-CreER mice (Tg(*Slc1a3-cre/ERT*)1Nat) (Stock # 012586), RiboTag mice (B6N.129-*Rpl22*$^{tm1.1Psam}$/J) (Stock # 011029), and CBA/J mice (Stock # 000656) were obtained from the Jackson Laboratory. Male Gfi1-Cre, GLAST-CreER, and RiboTag mice were each bred with female wild-type CBA/J mice for a single generation. Genotyping was performed using genotyping primers previously described (Yang, Gan et al. 2010) or the primers suggested by the Jackson Laboratory. Mice that were positive for at least one copy of either Gfi1-Cre or GLAST-CreER were then crossed

to mice with at least one copy of the RiboTag Rpl22-HA. Mice from the second cross were genotyped again, and experiments for hair cell-specific transcripts were performed with utricles from mice bearing both Gfi1-Cre and Rpl22-HA. Experiments on supporting cell-specific transcripts were performed using utricles from mice bearing both GLAST-CreER and Rpl22-HA. All mice used in this study were adults, with ages ranging from P30-P60. A mixture of male and female mice was used in all experiments. Mice were euthanized by CO_2 asphyxiation followed by decapitation. Utricles were immediately dissected in M199 media (Life Technologies, 12350039), and the epithelial roof was gently dissected away, leaving the otoconia intact. The utricles were incubated overnight at 37°C (95% air/5% CO_2) in DMEM/F-12 media (Life Technologies, 11320033) with 5% FBS (ThermoFisher), and 50 U/mL penicillin (Sigma). Cultured utricles were then either exposed to heat shock in microcentrifuge tubes placed in a 43°C in a water bath for 30 minutes and allowed to recover for 2 hours, or they remained at 37°C under control culture conditions. Some utricles were further dissected to remove the macrophage-containing stromal tissue underlying the sensory epithelium. For this procedure, cultured utricles were incubated with thermolysin (1-2 mg/mL; Sigma), elastase (4 U/mL; Sigma), and DNase I (10 Kunitz/mL; Ambion) in serum-free DMEM/F12 media for 10-15 minutes at 37ºC. Following treatment, utricles were transferred into a petri dish containing serum-free DMEM-F12, and epithelia were carefully separated ("peeled") from the underlying stroma using an eyelash tool. Peeled epithelia were then flash-frozen. All experiments were approved by the NIH/NINDS Animal Care and Use Committee (protocol #1327-14).

2.2.2 GLAST-CreER tamoxifen induction, Cre line reporter characterization

To investigate the cell types expressing Cre in each line, each line of Cre mice was crossed to a reporter line, B6.Cg-*Gt(ROSA)26Sor*$^{tm14(CAG-tdTomato)Hze}$/J (hereafter referred to as Rosa26-tdTomato, obtained from the Jackson Laboratory, stock # 007914). Following genotyping of pups, mice positive for both GLAST-CreER and Rosa26-tdTomato were administered either tamoxifen (30 mg/mL in corn oil; Sigma, T5648) at 0.225 mg/g body weight or an equivalent volume of corn oil vehicle by IP injection at P21-22 as previously described (Mellado Lagarde, Wan et al. 2014). Utricles were analyzed three weeks post-injection. Utricles from mice bearing both Rosa26-tdTomato and either Gfi1-Cre or GLAST-CreER were used to quantify Cre expression. Following overnight fixation (4% PFA in 1XPBS (ThermoFisher) and three 15-minute washes in 1XPBS), tdTomato fluorescence in utricle whole mounts was used to quantify the percentage of cells positive in each Cre reporter cross following staining for Myosin-VIIa and Hoechst 33342 (see section 2.3 for immunohistochemistry methods). Z-stack images (1 μm step size, unidirectional scanning, two frame averaging) were obtained for each utricle imaging through the sensory epithelium using a Zeiss LSM 780 confocal microscope (Carl Zeiss Microscopy, Oberkochen Germany). Image analysis was performed using Zen 2.3 software (Carl Zeiss Microscopy). tdTomato-positive HCs were counted in five 2500 μm^2 regions, and the percentage of those cells displaying Myosin-VIIa immunoreactivity at the level of the hair cell body and nucleus were averaged across regions and reported as a cell density. tdTomato-positive SCs were counted at the level of the supporting cell body in five regions, and the percentage of those

cells out of the total number of nuclei in the region were averaged across regions and reported as a cell density.

2.2.3 Immunohistochemistry and in situ hybridization

For validation studies, immunohistochemistry (IHC) and fluorescent in situ hybridization were performed using utricles from adult (P30-60) wild-type CBA/J mice (both males and females). Alexa Fluor-647 Phalloidin (1:75; ThermoFisher, A22287) was used to label the cuticular plate and stereocilia in validation IHC experiments. All utricles undergoing IHC were fixed overnight at 4ºC with 4% PFA in 1XPBS (ThermoFisher), washed 3 times (3X), 15 minutes each, with 1X PBS at room temperature followed by incubation in blocking solution (1X PBS, 2% bovine serum albumin, 0.8% normal goat serum or normal donkey serum, and 0.4% Triton X-100) for 3 hours at room temperature. Utricles were then incubated in primary antibody overnight at 4ºC, washed 3X 15 minutes with blocking solution, and incubated in secondary antibody for 4 hours at RT. Utricles were then counterstained for 10 minutes with Hoechst 33342 (1:5000; ThermoFisher, H3570), washed 3X 15 minutes 1X PBS, and mounted on glass slides using Fluoromount G (Southern Biotech). Imaging was performed using a Zeiss LSM 780 confocal microscope (Carl Zeiss Microscopy, Oberkochen Germany). The following primary antibodies were used for IHC and visualized using AlexaFluor-conjugated secondary antibodies (1:500; ThermoFisher): mouse anti-Myo7a (1:100, Developmental Studies Hybridoma Bank, 138-1), rabbit anti-Myo7a (1:250; Proteus Biosciences, 25-6790), rabbit anti-Rbp1 (1:100; Abcam, ab154881), mouse anti-Mreg (1:100; Novus Biologicals, 8F9-1B2), rabbit anti-Rasd2 (1:100; ThermoFisher, PA5-20439), mouse anti-Tspan8 (1:100; ThermoFisher, MA5-24296), goat anti-S100a11 (1:100; R&D Biosystems, AF4874), goat anti-Rbm24 (1:100; Santa Cruz

Biotech, SC-248361). For FISH, utricles were fixed overnight at 4ºC with 4% PFA, washed three times with 1X PBS, and cryopreserved sequentially at 4ºC in incubations of 1 mL of 10%, 20%, and 30% sucrose (Sigma) in 1X PBS each until tissue sank in the sucrose solution. Utricles were then incubated overnight in 30% sucrose with Optimal Cutting Temperature (OCT) compound (Tissue Tek), embedded and sectioned (10-12 μm sections) on a CM3050S cryostat (Leica Biosystems, Buffalo Grove IL). The RNAScope (Advanced Cell Diagnostics, Newark California) fixed frozen section pretreatment and staining assay was then performed according to the manufacturer's protocol. Briefly, slides were placed in a slide rack and washed for 5 minutes in 1X PBS, then submerged and boiled at 99-100ºC in 1X Target Retrieval reagent for 10 minutes, then washed in distilled water followed by washing in 100% ethanol. Slides were treated for 30 minutes with Protease III at 40ºC in a HybEZ oven (Advanced Cell Diagnostics). Slides were then washed briefly in distilled water, and in situ probes were incubated onto slides for 2 hours followed by two 2-minute washes in 1X Wash buffer. Fluorescent Amplification probes 1-4 were each hybridized in subsequent steps for 30, 15, 30, and 15 minutes respectively in the HybEZ oven at 40ºC, with each hybridization step followed by two 2-minute washes in 1X wash buffer. Slides were counterstained with DAPI for 30 seconds, and then mounted using Fluoromount G. Sections were imaged using a Nikon A1R confocal microscope (Nikon Instruments Inc., Melville New York) with identical magnification, gain, and pinhole settings between heat shock and control conditions relative to a negative control probe slide for each batch of slides processed. The following RNAScope probes were used in this study: *M. musculus* Hspa1b (Advanced Cell Diagnostics, 478211), *M. musculus* 3-plex positive control probe (Advanced

Cell Diagnostics, 320881), and 3-plex negative control probe (Advanced Cell Diagnostics, 320871).

2.2.4 RiboTag immunoprecipitation, cDNA library preparation, RNA sequencing, alignment of reads, and bioinformatic workflow

For immunoprecipitation (IP), 8-10 pooled whole utricles (or 10-12 peeled epithelia) were used in each biological replicate. Ribosome immunoprecipitation was performed as described previously (Sanz, Yang et al. 2009) with a minor modification. Briefly, the utricles were flash-frozen, homogenized in a Dounce homogenizer, and then incubated for 6 hours at 4ºC with a mouse anti-HA monoclonal antibody (Covance, MMS-101R). Antibody-incubated lysate was then precipitated using Protein G Dynabeads (Invitrogen) and incubated at 4ºC overnight. RNA was extracted from the initial lysate (hereafter referred to as 'input'), the IP samples, and the remaining lysate (hereafter referred to as 'supernatant') using the RNeasy Micro Plus kit (Qiagen) including the genomic DNA removal spin column step. RNA concentration and integrity of each IP and input RNA sample were determined using a total RNA Pico chip on a Bioanalyzer (Agilent Technologies, Santa Clara California). Sequencing libraries were prepared using the SMART-seq v4 Ultra Low Input RNA Kit for Sequencing (Takara Bio USA, Mountain View California). Dual indexed libraries were prepared using the Nextera XT DNA Library Preparation kit (Illumina, San Diego California). Eighteen Gfi1-Cre samples, including input, IP, and supernatants, were multiplexed and sequenced on a HiSeq 1500 (Illumina) in 126 x 126 bp paired end mode. On a second flow cell, twenty-four GLAST-CreER and peeled epithelium Gfi1-Cre samples (input and IP only for each condition)

were multiplexed along with a repeat of the original eighteen Gfi1-Cre samples and run on a HiSeq 1500 (Illumina) using 126 x 126 bp paired end mode.

2.2.5 Differential gene expression analysis workflow and gene ontology analysis

Demultiplexed FASTQ files were mapped to the mouse GRCm38/mm10 genome (Gencode GRCm38.vM11) using the STAR (v2.5.2) aligner (Dobin, Davis et al. 2013) with the "GeneCounts" parameter. Raw gene counts were analyzed for differential gene expression (DGE) using three RNA-Seq statistical methods: DESeq2 (Love, Huber et al. 2014), EdgeR (Robinson, McCarthy et al. 2010, McCarthy, Chen et al. 2012), and Limma-Voom (Law, Chen et al. 2014). Input and supernatant samples were not used in the final DEG analysis, and one control GLAST-CreER IP out of four replicates was dropped due to poor technical characteristics. Only those differentially expressed genes (DEGs) that were identified by all three analysis tools at a given cutoff (criteria described below) were considered for downstream analyses. The conservative approach of using multiple comparison tools can increase the specificity of identified DEGs in whole tissue RNA-Seq experiments (Seyednasrollah, Laiho et al. 2015), at the expense of decreased sensitivity. All six IP groups were compared in a pairwise fashion for each differential gene expression technique, yielding 15 total pairwise comparisons. Certain cell type marker genes of interest were observed to be oriented in the direction of enrichment for the predicted cell type even if the individual q-value or fold change magnitude assigned to that DEG differed between analyses. Therefore, two levels of fold change and a multiple comparisons q-value cutoff were adopted: 1) The "stringent" cutoff required a DEG to have at least a $\log_2$ fold change ($\log_2$FC) absolute value of 1.0 or greater, and a q-value of 0.05 or less for all

three analysis packages. 2) The "relaxed" cutoff required a $\log_2$FC absolute value of 0.585 or greater and an adjusted p-value of 0.2 or less for all three analysis packages. Thus, the 'relaxed cutoff' includes genes of possible biological interest that may have dropped out of the stringent cutoff potentially because of the statistical adjustments that differ between gene expression packages; however, it is important to note that cutoff criteria were used as an *a priori* attempt to analyze those DEGs with biological relevance within each dataset. Relevant comparisons such as the comparison between control whole-tissue Gfi1-Cre IP vs control whole-tissue GLAST-CreER IP were used to analyze cell-type-specific marker expression and validate cell type specificity based on Cre driver. For PCA analysis and visualization, the PCAExplorer package was used (Marini 2018). For gene-ontology (GO) annotation analysis, the PANTHER Classification System (Mi, Muruganujan et al. 2013, Mi, Huang et al. 2017) was used in conjunction with the GO Ontology database (released on 2018-02-02). GO annotations for the input genes were assigned a Bonferroni-corrected p-value and fold-enrichment compared to GO annotations in the *Mus musculus* PANTHER database of 22,262 mouse genes using Fisher's Exact test. The 'Complete Biological Process' and 'Complete Cellular Component' GO ontology databases were used to determine which GO annotations were overrepresented in each gene set using a cut-off of a Bonferroni-corrected p-value of 0.05 or less and a 2-fold enrichment cutoff. For differential GO annotation analyses between IP groups, ToppCluster (Kaimal, Bardes et al. 2010) was used in conjunction with the GO ontology database.

2.3 Results

2.3.1 Crosses with reporter mice reveal hair cell-specific recombination using Gfi1-Cre and supporting cell-specific recombination using GLAST-CreER

Utricles from Gfi1-Cre;Rosa26-tdTomato mice showed robust tdTomato labeling in nearly all HCs of the sensory epithelium (Fig 2.1 A-D), with 96.5% (SD ± 1.5%; n=4) of HCs expressing tdTomato (Fig 2.1 E). Gfi1-Cre;Rosa26-tdTomato utricles showed very little tdTomato-positive signal in the SC layer, with an average density of 1.1% (SD ± 0.7%; n=4) tdTomato-positive SCs per 2500 μm2. These data indicate that Gfi1-Cre resulted in robust recombination in hair cells with very little recombination in supporting cells.

GLAST-CreER;Rosa26-tdTomato utricles injected with corn oil vehicle showed no tdTomato-positive HCs (n=3), and an average density of 1.0% (SD ± 0.1%; n=3) tdTomato-positive cells in the SC layer. Utricles from mice that received tamoxifen at P21-22 (Fig 2.1 F-I) showed induction of tdTomato in the SC layer, with an average of 65.8% (SD ± 21.3%; n=7) of supporting cells expressing tdTomato (Fig 2.1 J), which is similar to previous GLAST-CreERT reporter recombination efficiency in adult utricle supporting cells (Stone, Wisner et al. 2018). Induction of tdTomato in HCs of these mice was low at 1.1% (SD ±

Figure 0.1 A comparison of the hair cell (HC) and support cell (SC) specific CRE promotors used in the study. A-E) Gfi1-Cre results in recombination in HCs. A-D: Representative maximum intensity projections from a Gfi1-Cre x Rosa26-tdTomato mouse showing tdTomato expression (A). Myo7a (C) was used to count HCs, and Hoechst staining (B) was used to count SC nuclei. Composite image (D) shows localization of the tdTomato signal primarily in hair cells. E) 96.5% of HCs and 1.1% of SCs are tdTomato+ in utricles from Gfi1-Cre;Rosa26-tdTomato mice. F-I: GLAST-CreER results in recombination in SCs. Representative maximum intensity projections from a tamoxifen-injected GLAST-CreER;Rosa26-tdTomato mouse showing tdTomato expression (F), Myo7a staining (H), Hoechst (G), and a composite (I) of tdTomato and Myo7a immunostaining. Localization in SCs is observed in the composite image. J) Quantification of tdTomato expression in cells in both vehicle-injected and tamoxifen-injected mice showing that tamoxifen results in tdTomato induction in SCs with little induction in HCs. Scale bar (I) represents 50 μm and applies to all panels. Utricles imaged at 40X magnification.

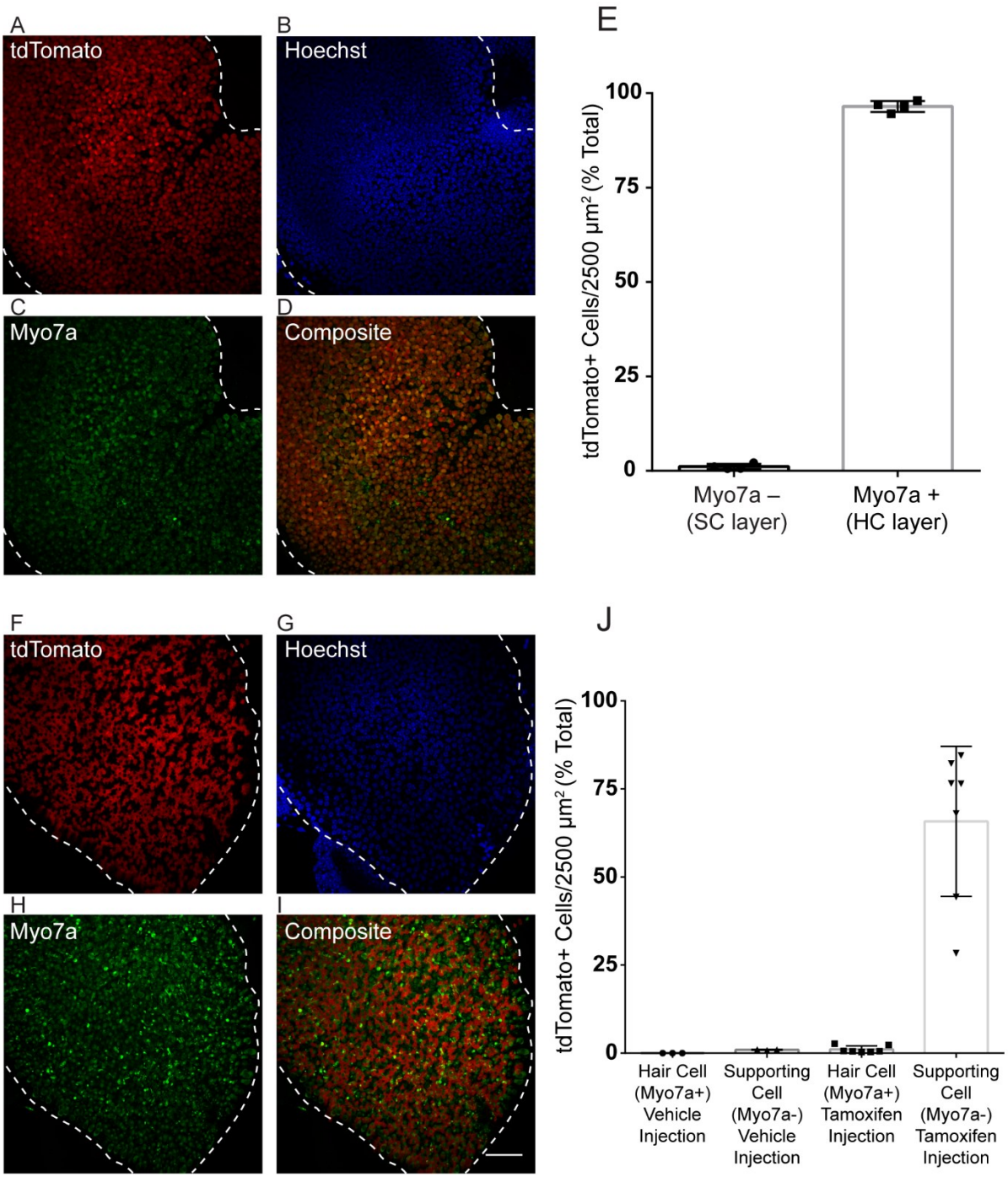

1.0%; n=7) (Fig 2.1 J). These data indicate that while the GLAST-CreER did not result in recombination in all supporting cells, it did so predominately in SCs with very little induction in hair cells.

2.3.2 Transcriptomes of RiboTag IPs readily separate according to both cell type and experimental condition

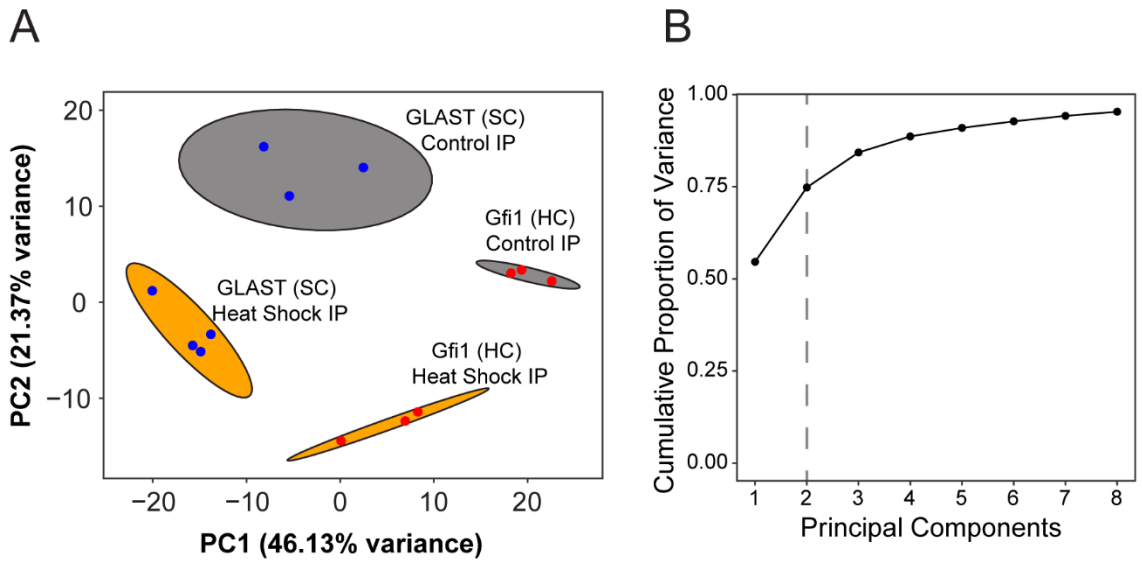

Figure 0.2 Bioinformatic analysis of RiboTag IP samples. A) PCA analysis of IP samples from RiboTag Gfi1-Cre (red) and GLAST-CreER (blue) IPs. PC1 represents 46.13% of the total variance in the experimental data, and PC2 represents 21.37% of the total variance. Ellipses represent 95% confidence intervals around each group of samples, and the color of each ellipse corresponds to the treatment type (heat shock in orange or control in gray). B) Cumulative proportion graph of variance explained by each PC after PC2 reveals that most of the experimental variance is contained within the first two principle components (dashed gray line) and subsequent PCs explain a diminishing amount of variance.

RNA-Seq was performed in each of the HC and SC specific RiboTag mice using total RNA isolated from cultured utricles, and cDNA libraries were generated and sequenced as described in the Methods Section. Using the top 500 most variable genes, PCA analysis of the control whole tissue Gfi1-Cre IP (n=3), control whole tissue GLAST-CreER IP (n=3), heat shock whole tissue Gfi1-Cre IP (n=3), and heat shock whole tissue GLAST-CreER IP (n=4) separated groups based on the Cre driver along principal component 1 (PC1; 46.13% of the total variance). Principal component 2 (PC2; 21.37% of the total variance) separated groups based on the treatment type (heat shock or control) (Fig 2.2 A). 95% confidence intervals plotted within the PC1 and PC2 coordinate space show a clear separation of each

experimental IP group. Examination of additional PCs revealed that most of the cumulative variance was captured within the first two PCs (Fig 2.2 B). Based on this separation, we analyzed DEGs with confidence that each group represented a unique combination of variance in treatment and Cre driver effects.

2.3.3 Transcripts from the Gfi1-Cre IP include canonical markers of hair cells, and transcripts from the GLAST-CreER IP include canonical markers of supporting cells

To determine whether enrichment of cell-specific transcripts had occurred in each group, DEGs that were enriched in either direction in the Gfi1-Cre IP compared to the GLAST-CreER IP under control (no heat shock) conditions were analyzed. Using the stringent cutoff criteria (see methods), 478 DEGs were enriched in the control Gfi1-Cre; this increased to 1513 DEGs when the relaxed cutoff was applied (Fig 2.3 A). These enriched transcripts included well-known HC markers such as *Gfi1*, *Ocm*, *Calb1*, *Bdnf*, and *Myo3a* when the stringent cutoff was applied to the DEG analysis. When the relaxed cutoff was applied, additional established HC markers such as *Ptprq*, *Pvalb*, *Atoh1*, *Calb2*, and *Ctbp2* were enriched in the Gfi1-Cre IP, indicating that the relaxed cutoff does include cell type-specific transcripts (Fig 2.3 B). These data indicate that the Gfi1-Cre RiboTag IP is enriched for HC-specific transcripts.

479 DEGs were enriched in the control GLAST-CreER IP using the stringent cutoff criteria (Fig 2.3 C). This number increased to 1287 DEGs when the relaxed cutoff was applied. Known markers of SCs, including *Slc1a3*, *Hey2*, *Jag1*, *Hes1*, *Sox9*, *Notch3*, *Tectb*, *Otog*, and *Cdh1* were enriched in the GLAST-CreER IP stringent cutoff group of DEGs. When the relaxed criteria were applied, another SC marker *Otoa*, was enriched in the

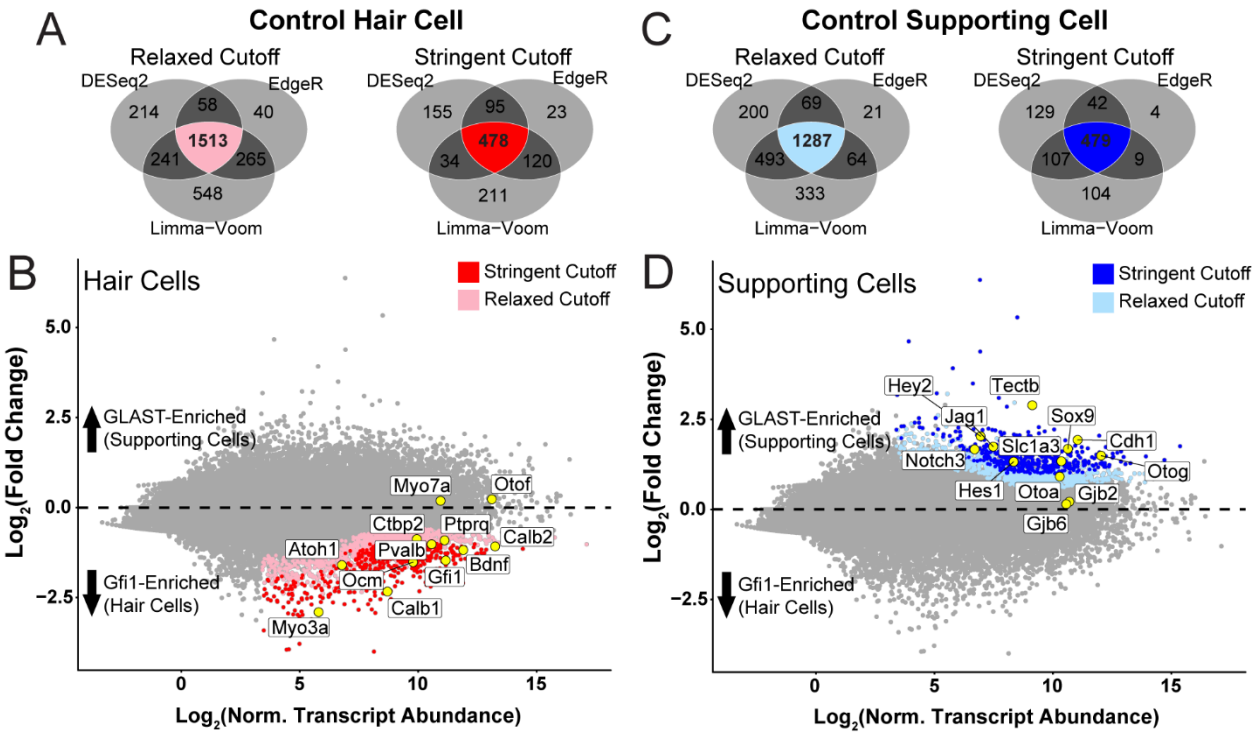

Figure 0.3 Identification of consensus DEGs between RiboTag IPs using three different gene expression tools. A) Transcripts that are enriched in HCs using the stringent criteria (478 DEGs) and the relaxed criteria (1513 DEGs). B) Gfi1-Cre RiboTag IPs are enriched for HC markers. Scatterplot of Log_2FC values versus normalized transcript abundance from the comparison of the Gfi1-Cre IP to the GLAST-CreER IP in the control (no heat shock) condition. Transcripts enriched using the relaxed (pink) and stringent (red) criteria are shown, and some known HC markers are labeled (yellow). C) Transcripts that are enriched in SCs using the stringent criteria (479 DEGs) and the relaxed criteria (1287 DEGs). D) GLAST-CreER RiboTag IPs are enriched for SC markers. Scatterplot of Log_2FCsversus normalized transcript abundance from the Gfi1-Cre IP compared to GLAST-CreER IP. Enriched transcripts using the relaxed (light blue) and stringent (blue) criteria are shown and include known SC markers (yellow).

GLAST-CreER IP (Fig 2.3 D). The markers analyzed in these control DEG comparisons have also been observed segregating to HC and SC cell types in previous RNA-Seq studies of mouse utricle (Burns, Kelly et al. 2015, Scheffer, Shen et al. 2015). Thus, the GLAST-Cre ER RiboTag IP is enriched for supporting cell-specific transcripts.

2.3.4 Hair cell DEGs are enriched for stereocilia components, while supporting cell DEGs are enriched for translational machinery and cell adhesion

To learn more about the enriched transcripts in each one of the IP groups we analyzed the data for functional enrichment of either biological processes or cellular components based on the gene ontology database (Table 2.1). DEGs identified using the stringent cutoff criteria in the control Gfi1-Cre IP group (478 genes) and in the GLAST-CreER IP group (479 genes) were used for GO annotation analysis. Control Gfi1-Cre IP DEGs showed significant enrichment for few terms in the 'Biological Process' category, including those focused on the neuroepithelial cell type and functional organelle organization. The enrichment for 'Cellular Component' terms for the Gfi1-Cre IP yielded more significantly overrepresented terms specifically dealing with the structural features of hair cell mechanotransduction, including GO terms for the stereocilia bundle, synaptic membrane, and transport vesicles which combined represent enrichment for transcripts coding for the major components of the hair cell synapse. Selected GO terms enriched in the Gfi1-Cre IP are summarized in Table 2.1 A. The control GLAST-CreER IP DEGs were significantly enriched for more GO annotations than the Gfi1-Cre IP DEGs using the same GO annotation cutoffs, notably in the 'Biological Process'category. Enrichment in the 'Biological Process' category included GO terms concerning cell-cell junction maintenance, L-glutamate uptake (presumably related to neurotransmitter recycling at the hair cell synapse), and active ribosomal assembly for cytosolic translation. GLAST-CreER IP GO enrichment in the 'Cellular Component' category contained terms that included both transcripts of proteins making up the epithelial extracellular matrix and underlying basement membrane as well as enrichment for transcripts

A **Hair Cell**

Biological Process GO Annotation	Genes in GO	Fold Enrichment	Adjusted p-value (FDR)
'Neuroepithelial Cell Differentiation' (GO:0060563)	63	7.33	2.36E-02
'Organelle Localization' (GO:0051640)	435	2.83	2.16E-02
'Cellular Localization' (GO:0051641)	1765	1.77	3.91E-02

Cellular Component GO Annotation	Genes in GO	Fold Enrichment	Adjusted p-value (FDR)
'Stereocilium' (GO:0032420)	46	6.69	3.31E-02
'Perikaryon' (GO:0043204)	131	3.92	3.09E-02
'Axon Part' (GO:0033267)	240	4.06	2.11E-04
'Transport Vesicle' (GO: 0030133)	271	3.03	1.35E-02
'Synaptic Membrane' (GO: 0097060)	317	2.59	4.65E-02
'Golgi Subcompartment' (GO:0098791)	402	2.42	4.88E-02

B **Supporting Cell**

Biological Process GO Annotation	Genes in GO	Fold Enrichment	Adjusted p-value (FDR)
'Hemidesmosome assembly' (GO:0031581)	4	36.86	1.05E-02
'L-glutamate uptake across plasma membrane' (GO:0098712)	7	21.06	2.82E-02
'Integrin activation' (GO:0033622)	8	18.43	3.51E-02
'Ribosome small subunit assembly' (GO:0000028)	19	12.93	4.63E-03
'Ribosome large subunit assembly' (GO:0000027)	35	7.02	3.49E-02
'Cytoplasmic Translation' (GO:0002181)	43	8	3.13E-03

Cellular Component GO Annotation	Genes in GO	Fold Enrichment	Adjusted p-value (FDR)
'Polysome Ribosome' (GO: 0042788)	10	14.74	2.71E-02
'Basal Lamina' (GO:0005605)	22	15.64	3.49E-05
'Basement Membrane' (GO:0005604)	103	10.02	4.23E-12

Table 0.1 Selected GO terms for Gfi1-Cre and GLAST-CreER IP enrichment comparisons. A) Sample of selectively-overrepresented 'Biological Process' and 'Cellular Component' GO terms returned using PANTHER on the 478 DEGs selected using the stringent cutoff criteria from the Gfi1-Cre IP (HC) enrichment compared to GLAST-CreER IP (SC). The name of the GO term and its accession number, the number of genes in each GO term, the fold of overrepresentation of DEGs in that GO term from the PANTHER query, and the FDR are shown in each column. B) Sample of significantly-overrepresented 'Biological Process' and 'Cellular Component' GO terms returned using PANTHER on the 479 DEGs selected using the stringent cutoff criteria from the GLAST-CreER IP enrichment compared to Gfi1-Cre IP.

related to polysomal translational machinery. The selected GO terms in the GLAST-CreER IP are summarized in Table 2.1 B.

2.3.5 Validation of cell type specificity in the RNA-Seq DEG analysis

In addition to looking at canonical markers of hair cells and supporting cells, we also validated additional DEGs. We selected three transcripts from the enriched DEG list for each IP (Gfi1-Cre and GLAST-CreER) and validated these using immunohistochemistry

(IHC). DEGs *Mreg*, *Rbm24*, and *Rasd2* were each enriched in the Gfi1-Cre RiboTag IP (Fig 4A), and the protein products of these genes were localized to HCs only (Fig 2.4 B-J). *Mreg* and *Rasd2* were both were enriched in the stringent cutoff, but *Rbm24* was enriched in the relaxed cutoff of the control Gfi1-IP compared to control GLAST-CreER IP. Both *Mreg* and *Rasd2* transcripts have previously localized to hair cells in the neonatal cochlea (Cai, Jen et al. 2015). All three targets localized to different regions of the hair cell. MREG immunoreactivity was localized to specific puncta within the HC body (Fig 2.4 C). RASD2 staining was localized specifically to the base of the cuticular plate (Fig 2.4 I) as previously observed (Burns, Kelly et al. 2015). RBM24 immunoreactivity filled the entire HC body (Fig 2.4 F). For supporting cells, *S100a11*, *Rbp1*, and *Tspan8* were DEGs that were enriched in the stringent cutoff of the control GLAST-CreER IP compared to the Gfi1-Cre IP (Fig 2.4 K). IHC staining for S100A11 and RBP1 appeared throughout the cell body of the SCs (Fig 2.4 M, Fig 2.4 P), whereas TSPAN8 immunoreactivity was localized to the SC cell membrane (Fig 2.4 S). Validation of the predicted cell type specificity for these genes supports the cell-specific DEG identification of the RNA-Seq data, and the predicted localization of RBM24 to HCs supports the idea that biologically meaningful DEGs may be

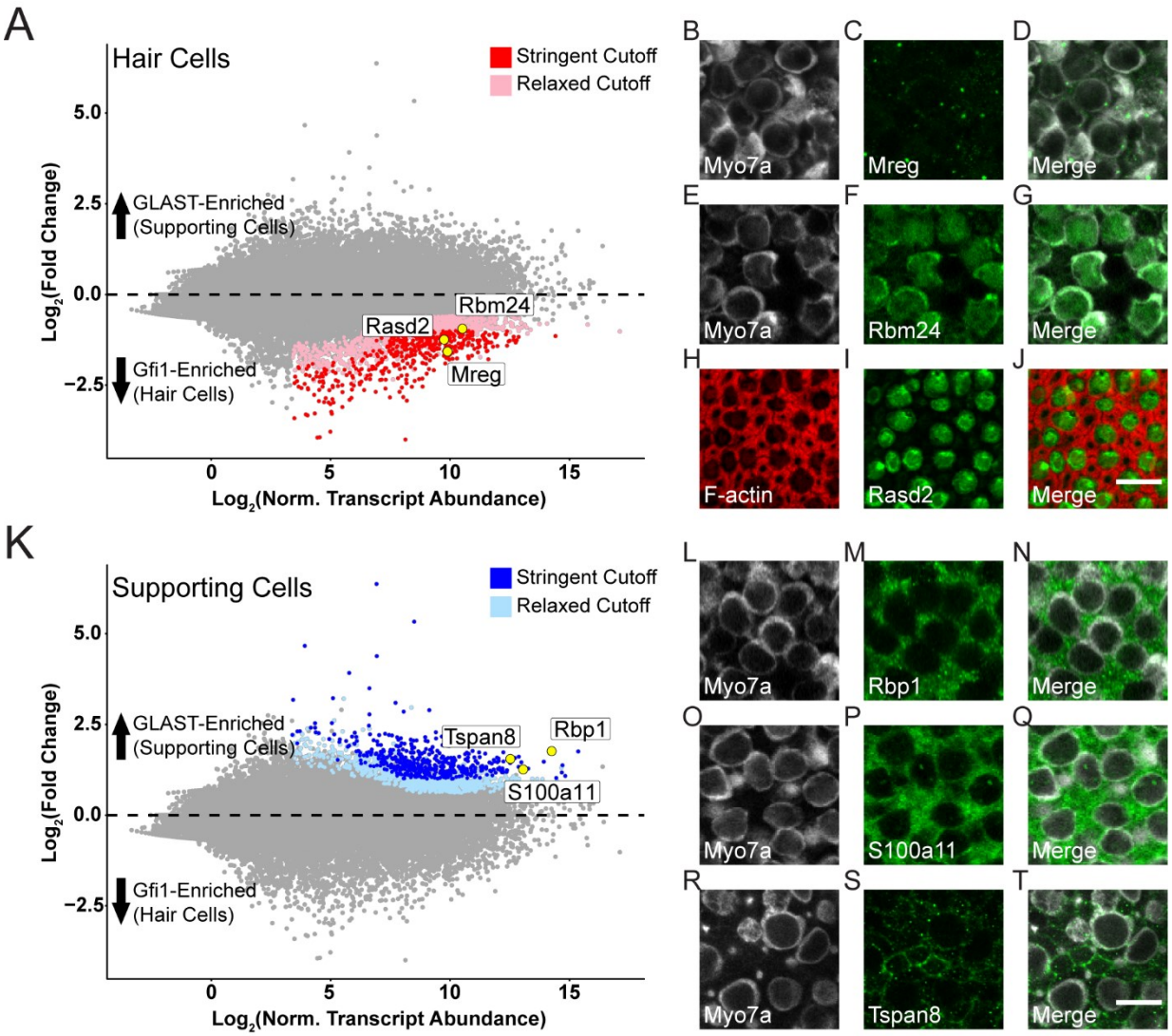

Figure 0.4 Validation of the cell-type-specificity of the RNA-Seq data. A) Three transcripts (*Mreg*, *Rbm24*, *Rasd2*) that were enriched in the Gfi1-Cre RiboTag IP were selected for validation. B-J: Immunohistochemical staining for the three targets selected in A. *Mreg* staining (green, C), *Rbm24* staining (green, F), and *Rasd2* staining (green, I) are observed in hair cells. Either *F-actin* (red, Phalloidin) or *Myo7a* (white) was used as a counterstain (B, E, H) with merged images (D, G, J). K) Three transcripts (*S100a11*, *Rbp1*, *Tspan8*) that were enriched in the GLAST-CreER RiboTag IP were selected for validation. L-T: Immunohistochemical staining for the three targets selected in K. d) *Rbp1* (green, M), *S100a11* (green, P), and *Tspan8* (green, S) are observed in supporting cells. *Myo7a* was used as a counterstain (white) (L, O, R) with merged images (N, Q, T). Images are 900 μm^2 composites from confocal images taken at 40X and 63X magnifications. Scale bars (J and T, lower right panels) represent 10 µm and apply to all panels.

found within the relaxed cutoff as was observed with cell specific canonical cell marker enrichments.

2.3.6 Removing the underlying stroma from the sensory epithelium reveals a macrophage DEG signature in the Gfi1-Cre RiboTag IP

In addition to hair cells, the Gfi1-Cre mouse line induces Cre recombination in resident macrophages of the inner ear, including those in the stromal tissue beneath the utricle sensory epithelium (Matern, Vijayakumar et al. 2017). To determine if transcripts from macrophages were present in the IPs from Gfi1-Cre RiboTag mice, we compared transcripts isolated from Gfi1-Cre IPs (n=3) to those isolated from utricles in which we removed the stromal tissue and examined transcripts from just the remaining "peeled" sensory epithelium (n=2) (Fig 2.5 A). PCA analysis using the top 500 most variable genes revealed that principal component 1 (PC1; 93.53% of the total variance) separates samples based on whether the samples were whole or peeled. Thus, the primary difference in DEGs in a comparison between these two groups reveals transcript differences between whole tissue (with stroma) and isolated sensory epithelium (without stroma). Using the stringent cutoff criteria, 606 DEGs were enriched in the whole tissue compared to the peeled epithelia, and 231 DEGs were enriched in the peeled epithelia compared to the whole tissue (Fig. 2.5 B). The group of 606 DEGs enriched in the whole tissue group contained 79 genes enriched in the GO annotation 'inflammatory response' (ToppCluster GO annotation, FDR <0.05, GO:0006954), including HSP32 (*Hmox1*), which we have reported in macrophages (Baker, Roy et al. 2015). The whole tissue DEGs also contained 75 genes with the GO annotation 'immune system development' (FDR < 0.05, GO:0002520), including *Ptprc* (also known as CD45), a general immune cell marker. Thus, within the 606 genes identified as DEGs enriched in whole tissue, both *Ptprc* and *Hmox1* were significantly enriched along with other markers of tissue macrophage identity including *Cx3cr1*, *Itgam* (also known as CD11B), *Cd68*, and *Adgre1* (also known as

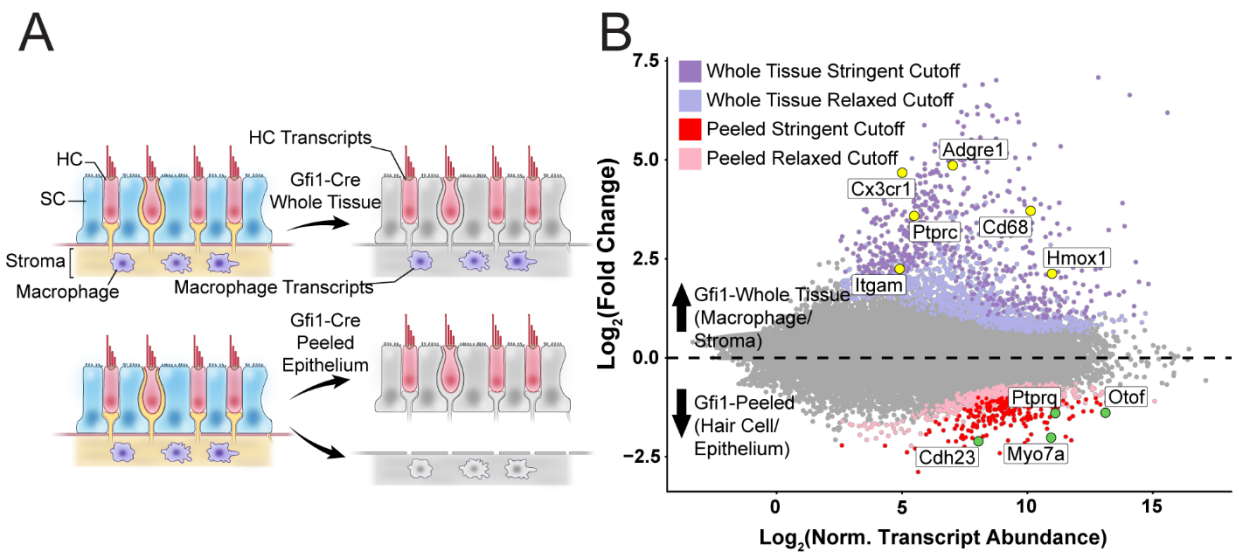

Figure 0.5 Isolation of cell type-specific transcripts from both HCs and tissue macrophages in the Gfi1-Cre RiboTag model. A) A schematic representation for how the identification of macrophage-specific transcripts was achieved by comparing DEGs from whole utricle Gfi1-Cre RiboTag IPs (top) to those from utricles in which the stroma had been separated from the sensory epithelium, yielding a "peeled" sensory epithelium (bottom). Shown are HCs (red), SCs (blue), stroma (beige), and macrophages (purple). B) Comparison of whole tissue (sensory epithelium plus stroma, purple) to peeled tissue (sensory epithelium without stroma) DEGs revealed macrophage markers. Scatterplot shows Log2FC values versus normalized transcript abundance from DEG comparison of the whole tissue Gfi1-Cre IP to the peeled epithelium Gfi1-Cre. Stringent and relaxed cutoff criteria were used to identify potential DEGs of interest, and markers of HC type (Myo7a, Otof, Ptprq, Cdh23) are shown in green and labeled along with markers of tissue macrophage cell type shown in yellow (Cd68, Itgam (CD11b), Ptprc (CD45), Cx3cr1, Adgre1 (F4/80), Hmox1 (Hsp32)).

F4/80) (Okano, Nakagawa et al. 2008, Sato, Shick et al. 2010, O'Malley, Nadol et al. 2016, Matern, Vijayakumar et al. 2017) (Fig 2.5 B). Importantly, neither of these inflammation-related GO annotations was enriched in the peeled (no stroma) epithelia DEG set, which was enriched for 'ear development' (FDR < 0.05, GO:0043583) (Fig 2.5 B). Thus, separating the sensory epithelium from the underlying tissue allowed us to identify macrophage-specific transcripts in the Gfi1-Cre RiboTag IP.

2.3.7 IPs from control and heat shocked utricles reveal a heat shock response in both hair cells and supporting cells

To investigate the response to heat shock in hair cells, we compared the control Gfi1-Cre IP to the heat shock Gfi1-Cre using both cutoff criteria. The stringent cutoff criteria identified 113 DEGs, and the relaxed criteria identified 329 DEGs (Fig 2.6 A). DEGs enriched in the heat shock Gfi1-Cre IP included 12 DEGs in the stringent cutoff group (18 DEGs in the relaxed cutoff group) enriched in the GO term 'response to heat' (FDR < 0.05 for both cutoffs, GO:0009408), and 15 DEGs in the stringent cutoff group (24 DEGs in the relaxed cutoff group) enriched in the GO annotation 'response to unfolded protein' (FDR <0.05 for both cutoffs, GO:0006986). We next examined the heat shock response in supporting cells by comparing the control GLAST-CreER IP to the heat shock GLAST-CreER IP using both cutoff criteria. The stringent cutoff criteria identified 66 DEGs, and the relaxed cutoff criteria identified 206 DEGs (Fig 2.6 B). Ten DEGs in the stringent cutoff group (12 in the relaxed cutoff group) were enriched for the GO term 'response to heat' (FDR < 0.05 for both cutoffs), and 13 DEGs in the stringent cutoff group (18 in the relaxed cutoff group) were enriched in the GO annotation 'response to unfolded protein' (FDR < 0.05 for both cutoffs). Thus, the enrichment by the heat shock condition was similar between hair cells and supporting cells, and markers of heat shock, including both major stress-inducible genes for HSP70, *Hspa1a* and *Hspa1b*, were enriched within the stringent criteria for both heat shocked Gfi1-Cre IP and GLAST-CreER IP compared to their respective control IPs. Importantly, when comparing between groups from the same cell type, DEG markers of cell identity were not included in the cutoffs, which emphasizes that the difference being compared is dominated by the effect of heat shock rather than cell type. For

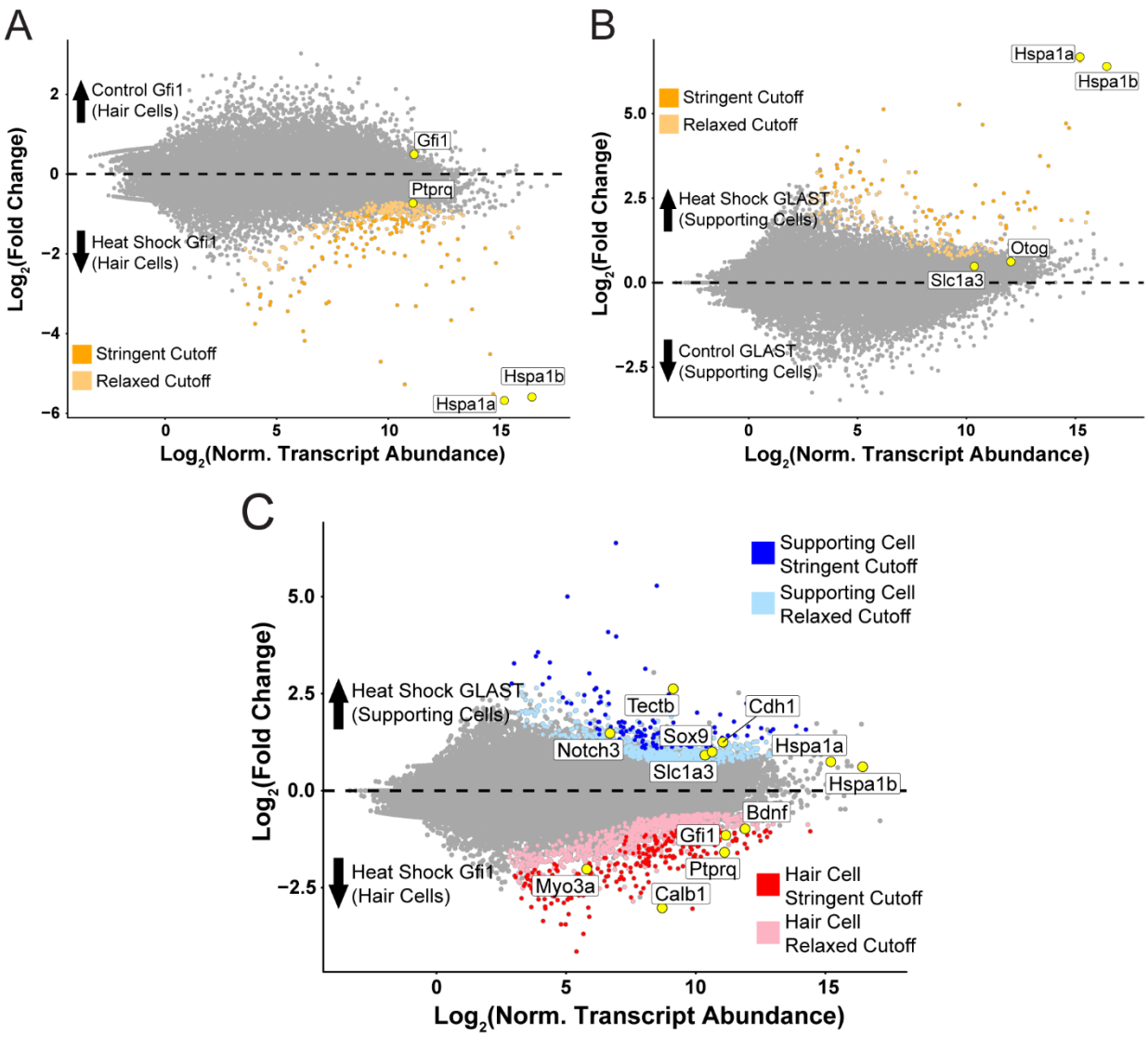

Figure 0.6 Both HCs and SCs demonstrate transcriptional responses to heat shock. A) Hair cell response to heat shock. Scatterplot shows Log2FC values versus normalized transcript abundance for the heat shock Gfi1-Cre IP group versus the control Gfi1-Cre group. DEGs identified using the relaxed cutoff are shown in light orange, and DEGs identified using the stringent cutoff are shown in dark orange. Inducible HSP70 genes Hspa1a and Hspa1b are highly enriched and shown as yellow points with labels. B) Supporting cell response to heat shock. Scatterplot shows Log2FC values versus normalized transcript abundance for the heat shock GLAST-CreER IP group versus the control GLAST-CreER IP group. DEGs are shown for relaxed (light orange) and stringent (dark orange) cutoff criteria. Enriched inducible HSP70 genes Hspa1a and Hspa1b are also shown (yellow, labeled). C) Heat shock responses in HCs vs. SCs. Scatterplot shows Log2FC values versus normalized transcript abundance for the comparison of the heat shock Gfi1-Cre IP group to the GLAST-CreER IP group. DEGs enriched in the heat shock GLAST-CreER IP using relaxed (light blue) and stringent (dark blue) criteria are shown, as are DEGs enriched for heat shock Gfi1-Cre IP for both relaxed (pink) and stringent (red) criteria. No enrichment is observed in either group for Hspa1a or Hspa1b (yellow, labeled), but enrichment is observed for HC markers Bdnf, Gfi1, Ptprq, Calb1, Myo3a in the heat shock Gfi1-Cre IP (yellow, labeled). Enrichment is observed for SC markers Notch3, Tectb, Sox9, Slc1a3 (GLAST), Cdh1 in the heat shock GLAST-CreER IP.

the Gfi1-Cre IP comparison, HC markers such as *Gfi1* and *Ptprq* were outside of the cutoff

criteria (Fig 2.6 A). For the GLAST-CreER IP comparison, SC markers such as *Slc1a3* and *Otog* were outside of the cutoff criteria (Fig 2.6 B). After examining the transcripts enriched by heat shock within each cell type, we then compared the heat shock response of hair cells to that of supporting cells. In this comparison, stress-inducible *Hspa1a* and *Hspa1b* no longer were significantly enriched in either cutoff group for either heat shock IP group (Fig 6C), indicating no specific enrichment in the heat shock transcriptional response in hair cells or supporting cells. The comparison between heat shock groups contained DEGs that describe steady-state cell type differences, with HC markers *Calb1*, *Gfi1*, and *Ptprq* enriched in the stringent cutoff for the heat shock Gfi1-Cre IP, and HC markers *Myo3a* and *Bdnf* enriched within the relaxed cutoff (Fig 2.6 C). Similarly, in the heat shock GLAST-CreER IP, SC markers *Notch3*, *Cdh1*, and *Tectb* were enriched in the stringent cutoff and SC markers *Sox9* and *Slc1a3* were enriched in the relaxed cutoff (Fig 2.6 C).

2.3.8 In situ hybridization for inducible HSPs following heat shock reveals expression of transcript in both SCs and HCs

In situ hybridization experiments on heat shock and control utricles for *Hspa1b* transcript (also known as inducible HSP70) demonstrated limited staining of the utricle

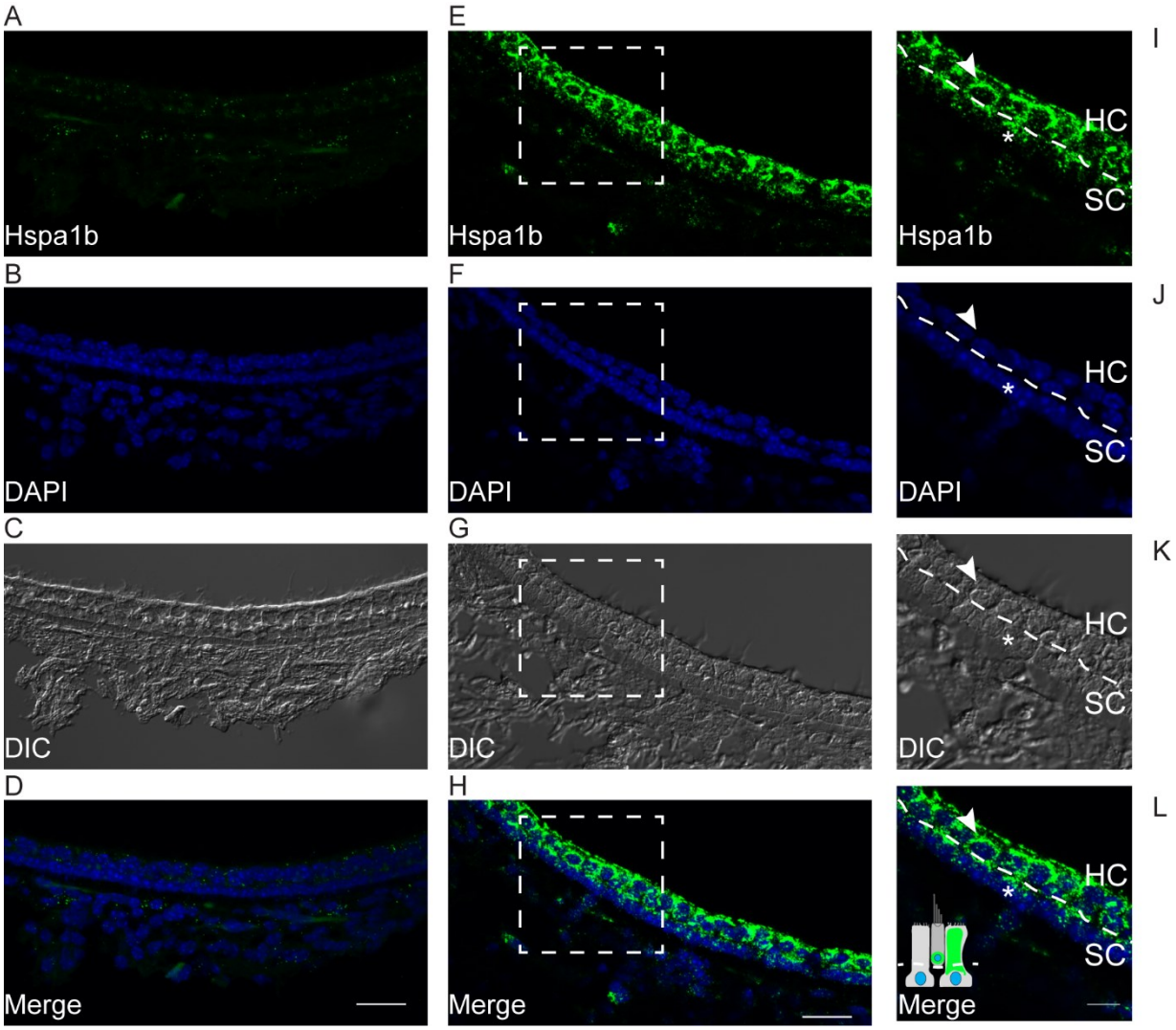

Figure 0.7 Both hair cells and supporting cells express HSP70 mRNA after heat shock. A-D: Representative utricle cross section Z-stack from control (non-heat shocked) cultured utricles hybridized with fluorescent in situ probe against Hspa1b. A) Hspa1b fluorescent in situ signal. B) DAPI nuclear counterstaining C) DIC image (single Z-stack slice) showing hair cell and supporting cell morphology in utricle epithelium cross section. D) Composite of A and B showing lack of strong Hspa1b signal in control utricle epithelium. E-H: Representative utricle cross section from heat shocked cultured utricles 2 hours post-heat shock hybridized with in situ probe against Hspa1b transcript. E) Hspa1b fluorescent in situ signal. F) DAPI nuclear counterstain. G) DIC (single Z-stack slice) to show morphology of the utricle epithelium cross section. H) Composite image of E and F show Hspa1b transcript hybridization signal in both hair cells and supporting cells. Images were taken at 60X, scale bars in lower right corners of D and H represent 25 µm. I-L: 3X digital zoom inset of heat shocked utricle from region bounded by dashed line boxes in F-H. HC and SC labels show hair and supporting cellular layers of the sensory epithelium, respectively, separated by a dashed line. Arrow indicates perinuclear Hspa1b hybridization signal in the HC layer, and the asterisk denotes a SC extension filled with Hspa1b hybridization signal in from the SC layer extending to the luminal surface of the epithelium. L) Diagram in the lower left corner is a representation of in situ signal localization in both HC and SCs. Scale bar in L represents 10 µm.

sensory epithelium under control culture conditions. As shown in Fig 2.7 A, there were some fluorescent hybridization signals in the HC layer for *Hspa1b* mRNA, demonstrating a limited amount of inducible HSP70 under control conditions in hair cells. The hair cell and

supporting cell layers of the sensory epithelium can be more clearly visualized using the combination of both DAPI and DIC imaging (Fig 2.7 B, Fig 2.7 C) along with the composite of the DAPI and FISH signals (Fig 2.7 D). Heat shocked utricles show a robust hybridization signal of *Hspa1b* transcript across the entire utricle sensory epithelium 2 hours after heat shock as well as a moderate increase in *Hspa1b* transcript signal in the underlying stromal cells. Given the saturation of the signal, it is somewhat difficult to discern which cell type the *Hspa1b* signal comes from, but as shown in Fig 7E as well as the zoomed-in inset in Fig 7I there are patterns of fluorescent signal in 'ring-like' structures around hair cell bodies as well as in the interstitial cytoplasmic protrusions of supporting cells rising to the luminal surface of the epithelium. These structures are visualized in a 3X digital zoom indicated by the arrow and asterisk in Fig 2.7 I-K. At the luminal surface of the epithelium *Hspa1b* hybridization signal can be visualized, although very little signal was directly observed in hair cell stereocilia bundles.

2.4 Discussion

Using the RiboTag method, we have shown that it is possible to isolate cell-type specific transcripts from both the supporting cells and hair cells of the mature mammalian utricle sensory epithelium. This study provides transcriptional profiles that agreed well with other cell-specific RNA-Seq (FACS single-cell RNA-Seq and proteomics) isolation methods that have been utilized in the inner ear (Burns, Kelly et al. 2015, Scheffer, Shen et al. 2015, Tao and Segil 2015, Hickox, Wong et al. 2017). We validated the transcriptional enrichment observed in the RiboTag IPs using immunohistochemistry to show localization of cell type-specific enriched transcripts. GO annotations enriched in the comparisons from both hair cell

and supporting cell IPs in the control condition suggest a fundamental difference between adult HC and SC cell types. GO analysis for the transcripts enriched in hair cells in both the 'Biological Process' and 'Cellular Component' categories suggest that the transcripts isolated through IP are primarily related to specific hair cell functions of mechanotransduction (e.g. components of the stereocilia bundle) and neurotransmitter release (e.g. components of synaptic vesicles, synaptic membrane, and vesicle secretion). On the other hand, supporting cell DEGs were enriched for a far more diverse set of both 'Biological Process' and 'Cellular Component' GO annotations, some of which were consistent with the supporting cell functions of maintaining the structural integrity of the sensory epithelium through cell-cell and cell-matrix protein expression.

Traditionally the RiboTag method has compared the IP enrichment of genes to the 'input' sample, i.e. those transcripts remaining after the immunoprecipitation (Sanz, Yang et al. 2009, Sanz, Evanoff et al. 2013, De Gendt, Verhoeven et al. 2014). Direct comparison of IPs from different Cre lines may be advantageous in future RiboTag studies, particularly when using inducible Cre models such as GLAST-CreER where we observed variable recombination efficiency in utricular supporting cells upon tamoxifen induction. Comparison to the 'input' for such inducible Cre models would be likely to fail to enrich in most instances, because there would be residual cell type-specific transcripts remaining in the input following IP; however, by comparison of IPs from two different Cre drivers, we were able to circumvent this limitation and study directly the ribosome-associated transcripts in hair cells and supporting cells in a single DEG analysis.

Our RiboTag data demonstrated induction of HSP70 mRNA in both hair cells and supporting cells after heat shock. We validated this finding using in situ hybridization, which

also showed induction of HSP70 mRNA (*Hspa1b*) in both hair cells and supporting cells in response to heat shock. Our previous immunochemistry data (May, Kramarenko et al. 2013) indicate that HSP70 immunoreactivity is largely restricted to supporting cells after shock. Taken together these data indicate that heat shock results in induction of HSP70 mRNA in both cell types, but HSP70 protein levels increase in supporting cells with little increase in hair cells. Thus, our data point to differences between hair cells and supporting cells in the translational efficiency of the heat shock response. Several lines of evidence suggest that the mechanism underlying this difference is likely reduced overall translational capacity in hair cells compared to supporting cells. First, SCs were functionally enriched in transcripts related to ribosomal subunits and translational machinery, including polysome ribosome components. The comparative enrichment of these DEGs specifically in SCs suggests a relative enrichment in the ribosomal apparatus compared to HCs, and by extension an increased translational capacity of the SCs relative to HCs. Second, the relative lack of translational activity in mature HCs compared to SCs has been previously reported using other methodologies in studies of translational turnover within these two cell types. Incorporation of click-chemistry-tagged amino acids into newly synthesized proteins revealed that the level of protein synthesis is lower in hair cells compared to supporting cells (Francis, Katz et al. 2013). Third, mature mammalian utricular hair cells also have low turnover of proteins in stereocilia bundles as measured by incorporation of ^{15}N-containing amino acids using multi-isotope mass spectrometry (MIMS), and although cytoplasmic protein turnover and turnover at stereocilia tips was higher than in the stereocilia shaft in hair cells, this suggests that hair cells by extension could have altered regulation of proteostasis (Zhang, Piazza et al. 2012) Together these data suggest that the reason that HSP70 protein is

reduced in HCs compared to SCs (despite similar induction of HSP70 mRNA) after heat shock may be due to a lower concentration of functional ribosomes/polysomes in an average hair cell compared to an average supporting cell. Thus, hair cell ribosomes may be translationally saturated (or nearly saturated) at steady-state, and they may lack the excess translational capacity to generate a robust inductive stress response at the protein level. Indeed, using the click-chemistry incorporation of tagged amino acids, translation in mouse utricular and cochlear hair cells was specifically decreased upon exposure to ototoxic aminoglycoside antibiotics, and others have demonstrated inhibition of translation or protein synthesis in mouse cochlear explants upon exposure to cisplatin (Francis, Katz et al. 2013, Nicholas, Francis et al. 2017). If we interpret the RiboTag experiments at the molecular level, then our results imply that the translation block in HCs that would result in reduced HSP70 protein expression compared to SCs must occur during either the elongation or termination phases of translation, because the Rpl22-HA protein used for the immunoprecipitation is part of the larger 60S ribosomal subunit (Sanz, Yang et al. 2009), which typically binds the mRNA after translation initiation has occurred.

The RiboTag method was employed here as a means of deriving HC and SC-specific transcriptomes, but as with any method it is worth discussing both the advantages and limitations of the approach. Interestingly, some HC markers such as *Myo7a* and *Otof* were not enriched in the Gfi1-Cre IP, indicating that the separation of marker genes using the RiboTag IP method does not necessarily enrich for all possible cell-type transcripts. Similarly, two SC markers, *Gjb2* and *Gjb6*, were not enriched in the control GLAST-CreER IP in this comparison, which mirror the observations for HC enrichment that the IP comparisons do not capture all cell-type DEGs (Fig 2.3 D). Notably, comparison of the control whole tissue

Gfi1-Cre and peeled Gfi1-Cre IPs demonstrated enrichment for both *Myo7a* and *Otof* in the peeled Gfi1-Cre IP (Figure 2.5 B), which the comparison of the whole tissue Gfi1-Cre IP to the control whole tissue GLAST-CreER IP did not enrich for. Therefore, it may be advantageous in some cases to perform de-epithelialization to more completely isolate the full profile of cell-specific transcripts, as enrichment for each cell type may be incomplete when IPs are compared that have been isolated from a highly heterogenous whole tissue lysate. This effect may be due to the limited efficiency of the immunoprecipitation, which is estimated to capture roughly 25% of the HA-tagged ribosomes from tissue lysates (Sanz, Yang et al. 2009). Therefore, isolated sensory epithelia represent a more purified pool of cell-specific transcripts, increasing the IP efficiency. It is also important to note that in the Gfi1-Cre model, both hair cells and tissue macrophages underwent Cre-mediated recombination (Matern, Vijayakumar et al. 2017). Markers from inner ear tissue macrophages were identified through comparison of peeled sensory epithelia IPs compared to whole tissue Gfi1-Cre IPs, which allowed for 'unmasking' of the macrophage-specific transcripts. Although the reliance of RiboTag on Cre lines that may undergo recombination in cell types other than the target cell type is a limitation of the RiboTag system, it may also represent a unique opportunity to discover expressed transcripts from rare and difficult-to-isolate cell populations such as tissue macrophages or other resident leukocyte-derived cells. Although this technique would require de-epithelialization, it would avoid the stress induced by complete tissue dissociation and FACS (van den Brink, Sage et al. 2017). One limitation of this study is that it captures the response to heat shock in the utricle at a single timepoint, 2 hours post-heat shock. This time point corresponds to the peak of HSP70 mRNA expression in heat shocked utricles, and therefore although the response in each cell type appears quite

similar at this time point, there may be subtleties of the cell type specific response to heat shock that appear later in the downstream stress response. Further studies of the differences in ribosomal abundance and protein synthesis between hair cells vs. supporting cells may also further elucidate some of the observed transcriptional enrichments isolated in this study.

This study demonstrates that the RiboTag method is a viable means of obtaining cell type-specific transcripts in the inner ear. We first characterized the specificity of the Cre mouse models used in this study using a tdTomato reporter line. We isolated transcripts from supporting cells and hair cells and validated the methodology by showing RNA-Seq enrichment of known cell type markers, immunohistochemistry of novel markers, and in situ hybridization. The Gene Ontology enrichment for each cell type shows supporting cells may be functionally enriched in translational machinery when compared to hair cells, which are enriched predominately for structural transcripts related to stereocilia and mechanotransduction. We have demonstrated that the Gfi1-Cre model also enriches for the tissue macrophages of the inner ear, and these transcripts can be revealed through immunoprecipitation of peeled utricle sensory epithelia in comparison to the whole tissue, which contains the macrophages in the underlying stromal tissue as shown by enrichment for known markers of the tissue macrophage cell type. Lastly, we have studied the effect of heat shock stress on cultured utricles and shown that the heat shock response is present at the transcriptional level in both hair cells and supporting cells. Although previous research has shown HSP70 protein induction predominately in supporting cells of the cultured utricle, HSP70 transcript is observed by in situ hybridization in both cell types following heat shock. A potential explanation for this observation is that supporting cells may be functionally enriched for translational machinery compared to hair cells, allowing them to produce a more

robust protein-level response to inductive stressors such as heat shock. By extension, hair cells may utilize their translational machinery 'at capacity' at steady-state, resulting in reduced heat shock protein expression. Future research into cell type-specific translational dynamics may further resolve the dynamics of the heat shock response in the inner ear.

2.5 Experimental contributions

I performed utricle dissection and culture, performed validation immunohistochemistry and in situ hybridization, prepared SMART-seq cDNA generation, Nextera XT library construction, and performed analysis of DEGs and GO enrichments. Lindsey May performed mouse breeding and genotyping, assisted in utricle dissection and culture, optimized and performed the RiboTag immunoprecipitation assay assisted in extracting RNA from each sample. Robert Morell performed RNA-Seq sample demultiplexing, raw read alignment, read quality analysis, bioinformatic guidance, and DEG analysis reporting. Daniel Martin generated the bioinformatic pipeline to process through samples using the DEG analysis packages used in the study and provided bioinformatic guidance. Nora Welsh assisted in performing target validation immunohistochemistry. Erich Boger assisted in performing SMART-seq cDNA generation, Nextera XT library construction, and performed the HiSeq 1500 flow cell preparation and sequencing runs.

Chapter 3: Single cell RNA-Seq of heat shocked utricle epithelia

3.1 Introduction

The transcription of genes is a complex process and using orthogonal experimental gene expression techniques can help to resolve transcriptional changes that occur in different cell types. In Chapter 2, we used the RiboTag technique to enrich for HC and SC transcripts from adult mouse utricles before and after heat shock. The conclusions from the DGE analysis of that study suggested that these two cell types had similar transcriptional profiles after heat shock but differed in their control phenotypes. One difference that was noted in that chapter was the significant enrichment of SCs for Gene Ontology (GO) groups of genes involved in translation. Despite some of the caveats associated with single-cell RNA-Seq that were discussed previously, the RiboTag technique itself has several caveats that limit the interpretation of the conclusions from the previous chapter. One limitation of RiboTag-based RNA-Seq approaches lies in the enrichment step. If cell types isolated using different Cre driver lines are compared and react similarly to a stimulus (heat shock), it is difficult to determine whether the gene enrichment is a result of background enrichment from residual transcripts from mRNA isolated in the tissue lysate input or directly from that cell type. Thus, concluding that the heat shock response is seen in both hair cell and supporting cell immunoprecipitates (IPs) does not exclude the alternative explanation that heat shock mRNA species enriched in each IP are carried over from the input pool. According to the RiboTag-based experimental results in the Chapter 2, the heat shock response appeared to be either in both cell types or perhaps in one cell type with enrichment carryover from the input into the other cell type. Although it is theoretically possible as a workaround to attempt to subtract

enriched genes also present in the input samples of each IP replicate, the advantages of directly comparing the IPs from each Cre driver are numerous: 1) It allows for complete detection of all enriched species from each Cre line without loss of enriched genes due to subtracting out borderline-enriched mRNA species from the input, 2) it allows for comparison of 'like-to-like' in terms of sample sequencing complexity, as most IP are aligned reads from much lower inputs of mRNA compared to the bulk tissue inputs and thus are subjected differing levels of read distribution normalization during DGE analysis, and lastly 3) it allows for the straightforward accounting of experimental variance as a result of Cre driver and heat shock/control experimental treatment factors without introducing an uncontrolled third factor of background subtraction that would be unaccounted for in the downstream DGE analysis. Furthermore, the enrichment immunoprecipitation will only enrich for those mRNA species isolated through antibody capture; moreover, it will only enrich to the extent that those transcripts are preferentially expressed in that cell type above the background input signal of bulk tissue mRNA combined with uncaptured mRNA. It was noted in the Chapter 2 that not all markers were detectable in each immunoprecipitation from each cell type despite the relative specificity of the Cre driver. One part of the explanation for this could be lack of immunoprecipitation of the complete collection of cell-specific transcripts from each cell; nevertheless, conclusions about the GO enrichments from the previous chapter and the resulting conclusions are sound since cell type is a strong driver of difference between mature HCs and SCs. The GO analysis is likely to find the relevant functionally-overrepresented GO groups for each cell type even if only a subset of transcripts were profiled in each IP.

In this chapter, we characterize the single cell transcriptional profiles present in adult mouse utricle epithelium as well as use the single-cell transcriptional data to clarify the ambiguity in the conclusions regarding the heat shock response from the previous chapter introduced by the inherent limitations of the RiboTag technique. The primary advantage of single-cell RNA-Seq that was leveraged in this study is that each cell's mRNA profile is granular, meaning that gene detection after sequencing is uniquely isolated from a single given cell, and therefore the overall response of clustered cell types represents the transcriptional response from that cell type alone. Thus, we can ascertain cell-specific responses to heat shock, which helps test the validity of the conclusions arrived at in Chapter 2.

3.2 Methods

3.2.1 Mouse breeding, organotypic utricle culture, heat shock stimulation

Adult (P30-P90) wild-type littermate mice (male and female) from the RiboTag (B6N.129-*Rpl22*$^{tm1.1Psam}$/J) Gfi1-Cre (*Gfi1*$^{tm1(cre)}$Gan) cross (See Chapter 2) were used to perform single-cell captures. Organotypic culture and heat shock stimulation are identical to section 2.2.1.

3.2.2 Utricle epithelium isolation, single cell suspension preparation and cell counting

For utricle epithelium peeling, cultured utricles were incubated with a 0.2 µm sterile-filtered (Millipore) solution of thermolysin (1-2 mg/ml; Sigma), elastase (4 U/ml; Sigma),

and DNase I (10 Kunitz/ml; Ambion) in serum-free DMEM/F12 media for 10-15 minutes at 37ºC. Following treatment, utricles were transferred into a petri dish containing serum-free DMEM/F-12 media, and epithelia were carefully separated ("peeled") from the underlying stroma using an eyelash tool. The process for isolating 8-10 utricle epithelia took about 30-45 minutes. We worked in tandem to process 8-10 heat shocked utricle epithelia while 8-10 control (non-heat shocked) utricle epithelia were simultaneously being isolated. To prepare single-cell suspensions, the Papain Dissociation System (Worthington Biochemical) was used according to manufacturer instructions by preparing the following solutions: Papain solution (sterile Earle's Balanced Salt Solution (EBSS), papain (20 U/mL), 1 mM L-cysteine, and 0.5 mM EDTA), ovomucoid/BSA inhibitor solution (DMEM/F-12, 10 mg/ml ovomucoid inhibitor, 10 mg/ml bovine serum albumin), and DNase I solution (EBSS, 2000 U/ml DNase I). The papain solution was dissolved at 37ºC in a heated bead bath for 10 minutes prior epithelium isolation, and then the open papain solution vial was transferred to a 37 ºC incubator with 95% air/5% CO_2 for oxygenation and pH equilibration for 15-20 minutes. The DNase I solution was also equilibrated at 37ºC (95% air/5% CO_2). 500 mL of DNase I solution was added to 5 ml of papain solution after equilibration, and utricle epithelia were transferred by sterile glass pipette into a sterile microcentrifuge tube containing 500 µl of the papain/DNase I solution. Utricle epithelia were incubated in this solution for 1 hour in a 37ºC incubator with 95% air/5% CO_2. At 10-minute intervals during this incubation, the epithelia-solution mixture was triturated by pipetting a 200 µL volume up and down approximately 100 times. 5 minutes before the end of the incubation, a cell-permeant live stain (Calcein AM, Invitrogen), dead cell impermeant stain (ethidium homodimer I (EthDI), Invitrogen) and cell-permeant nuclear counterstain (Hoechst 33342, Invitrogen) were added

to the cell suspension, each at a 1:625 dilution. Hoechst dye was added to one condition, heat shock or control, per capture chosen at random so that treatment conditions could be distinguished by fluorescence. At the end of the incubation, 500 µl of ice-cold ovomucoid/BSA solution was added to the cell suspension at the end of the papain/DNase I incubation to inhibit protease activity. The resulting cell suspension was spun at 1420 rpm at 4ºC in a swing bucket centrifuge (Allegra X30-R, Beckman Coulter) for 5 minutes, and the cell pellet was then resuspended in 1 ml of DMEM/F-12, followed by a second 5-minute spin at 1420 rpm at 4ºC and resuspension in 1 ml of fresh DMEM/F-12 to remove any residual dyes. Excess media was carefully removed, and the cell pellet was then gently resuspended in 15 µl of DMEM/F-12. A 1:10 dilution of resuspended cells used to obtain a cell count with live/dead fluorescent signals quantified using a Luna-FL automatic cell counter (Logos Biosystems). Cells were placed on ice until single-cell capture was performed.

3.2.3 Single cell capture, single cell imaging, full-length cDNA generation

Single cell capture, cell lysis, reverse transcription, and cDNA PCR amplification were performed using the Fluidigm C1 system (Fluidigm, PN 100-7168 L1). Briefly, either small- or medium-sized (5-10 µm and 10-17 µm cell diameter cutoffs, respectively) integrated fluidic chips (IFC, Fluidigm) were primed with cell wash buffer for 30 minutes on the C1 platform. The IFC priming step was performed while cells were being dissociated to minimize the time between dissociation and cell capture. After IFC priming, cells from both conditions were loaded in equal proportions along with wash buffer according to their cell counts such that a total of approximately 2 x 10^5 cells was loaded into the IFC in a volume of 20 µl of media and cell wash buffer. After loading, cells were captured on the IFC and

washed before removing the chip from the C1 for imaging. Images from all 96 capture sites on the IFC were recorded using a Axio Observer.Z1 microscope (Zeiss) at 10X magnification. Z-Stacks of 5-7 images (~5 μm step size) were taken at each capture site using a custom automated script in the Zen Blue software (Zeiss), and the Calcein AM, EthDI, and Hoechst fluorescence intensity values at each capture site in the IFC were recorded, background-subtracted and normalized the maximum single cell mean gray value from each channel to evaluate the efficacy of the live/dead and conditional staining. Following imaging (~ 30 minutes), the IFC was re-inserted into the C1 machine, which then automatically performed cell lysis, reverse transcription, and PCR amplification of cDNA on cells in each capture site on the IFC using reagents from the SMARTer Ultra Low RNA kit (Clontech). In total six captures were performed (3 small-sized and 3 medium-sized IFC captures). cDNA concentrations were determined for each single cell capture site using the PicoGreen assay (Life Technologies) with fluorescence intensities measured on a DTX 880 fluorescence plate reader (Beckman Coulter). The Nextera XT DNA Library kit (Illumina) was used to fragment cDNA, add adapters, PCR-amplify cDNA (12 cycles), and add barcodes to designate each unique single cell cDNA library. Two multiplexed cDNA libraries were generated, with each library generated using cDNA from three single cell capture IFCs each for a total of six IFC captures.

3.2.4 RNA sequencing and alignment of reads

Multiplexed libraries were sequenced on a single lane of a HiSeq 1500 (Illumina) using 126 x 126 bp paired-end mode. The second batch of three captures was sequenced on another lane of a HiSeq 1500 and added to the first batch of reads. Demultiplexed FASTQ files were aligned using STAR (v2.5.2) (Dobin, Davis et al. 2013) with the

"TranscriptomeSAM" parameter to GRCm38/mm10v17 genome (Gencode GRCm38.vM10). Transcript abundances from aligned reads were then estimated on a per gene level using RSEM v.1.2.19 (Li and Dewey 2011) in units of transcript per million (TPM). Aligned read QC and down sampling was performed using RNA-SeQC (DeLuca, Levin et al. 2012).

3.2.5 Downstream bioinformatic analysis: Principal component analysis, batch correction, marker expression, and cell clustering

Identification of cell outliers, normalization of TPM counts, IFC-capture batch correction, and clustering of single cell gene counts was performed using custom R scripts generated to analyze single-cell RNA-Seq datasets from inner ear tissue (Burns, Kelly et al. 2015) as well as the R package SINGuLAR v3.5.2 (Fluidigm, PN 100-5066 F1). Briefly, the TPM count table from 177 cells was loaded into the SINGuLAR Outlier analysis script, and outliers were identified based on shared expression of genes within the TPM count table and excluded from the dataset. These excluded cells were confirmed as outliers via principal component analysis (PCA) of all single cells. The TPM expression table was then loaded into a custom R analysis package and normalized across cells as previously described (Burns, Kelly et al. 2015). The information recorded for each cell (identifier, capture number, heat shock/control condition, Hoechst dye usage) were then loaded into an expression set object as covariates for each cell. The 'capture number' covariate was corrected for as a batch effect across cells. Using unsupervised PCA analysis, clustering of cells along different principal components was noted qualitatively. The expression matrix was then filtered for highly-variable genes to select genes play a role in driving cell clustering by PCA. The principle components (PCs) that managed to separate cells into meaningful groups were then

used to further filter the gene list down to 500 genes that had the highest loadings across each of the selected PCs.

3.2.6 Between-cluster differential gene expression (DGE) analysis and gene ontology overrepresentation analysis

Once cells were clustered into distinguishable cell types, the next goal was to determine differentially expressed genes (DEGs) between the four cell treatments of interest (control HCs, control SCs, heat shocked HCs, and heat shocked SCs) in a pairwise manner. The SINGuLAR v3.5.2 package was used to perform a one-way ANOVA by calculating the average expression of each transcript grouped by cell type. Adjusted p-values (Benjamini-Hochberg multiple comparisons correction) were calculated for each DEG based on one-way ANOVA with individual pairwise comparisons (Tukey posthoc test) between the log-transformed mean expression values for each gene across groups (hereafter referred to as a fold change). A between-treatment groups p-value cutoff of ≤ 0.05 was used to determine significantly enriched DEGs between groups. GO analysis was performed using PANTHER (Mi, Muruganujan et al. 2013, Mi, Huang et al. 2017) and ToppCluster (Kaimal, Bardes et al. 2010) as described in section 2.2.5.

3.2.7 Immunohistochemistry and in situ hybridization single cell validation

Immunohistochemistry staining and fluorescent in situ hybridization were performed as described in section 2.2.3. The following RNAScope probes were used in this study: *Cd9* (ACDBio, 430631), *Otof* (ACDBio, 485671), *Hspb1* (ACDBio, 488361).

3.3 Results

3.3.1 Preliminary analysis selects single cell transcriptomes based on capture cell fluorescent signal, cDNA yield, and bioinformatic outlier analysis

Several preliminary steps were taken to choose single cell for downstream bioinformatic analysis. Normalized fluorescence intensity values were used to effectively distinguish cells in each condition captured on the same IFC. Background and fluorescence intensity measurements were measured for 159 captured single cells and scaled to the maximum value of fluorescence value for that capture, normalized onto a scale of 0-1000 (arbitrary units). Condition was based on the presence or absence of a Hoechst fluorescent signal. Prior to each capture, we decided which condition would be labeled with Hoechst dye. For captures 1, 2, and 6, Hoechst dye was added to the heat shocked cell suspension. For captures 3, 4, and 5, Hoechst dye was added to the control (no heat shock) cell suspension. When fluorescence intensities were then quantified, a statistically significant difference in each capture between cells identified as Hoechst-positive and Hoechst-negative (unpaired t-test, two-tailed, not assuming consistent SD, $p < 0.0001$ for all comparisons) was observed, indicating clear distinction of conditions in each capture (Fig 3.1 A). cDNA concentration measurements were then measured for the 159 single cells identified in the six IFC captures, and these concentrations combined with IFC capture image quality of each cell were used to choose cells from each IFC capture that yielded enough cDNA ($\geq$ ~70 pg/µl) to generate libraries for sequencing, yielding 156 single cells for sequencing (Fig 3.1 B). No significant effect on cDNA yield from cells pooled by condition was observed due to heat shock versus

control treatment (p=0.381, Mann-Whitney U Test, two-tailed) (Fig 3.1 C). Outlier analysis identified 134 cells that passed the outlier selection algorithm used in the SINGuLAR analysis package. In addition to these cells, two outlier cells from capture 1 (G11-1_G8-CS41_3 and H06-1_D9-CS22_3) were added from below the cutoff, bringing the total to 136. The cDNA yield and total number of genes detected from these 2 cells were otherwise within the range of the accepted cells, so it was decided to include them as they represented only a fraction of the minority of cells that fell below the outlier cutoff. One of the remaining 136 cells, B10-2_C7-CS18_4, was manually dropped from the analysis despite passing the outlier test and having a normal cDNA yield due to having only 202 genes detected (TPM > 1) after read alignment (Fig 3.1 C, Fig 3.1 D). Thus, from a total of 156 single cell libraries that were sequenced, 135 (87%) yielded libraries that were used in the downstream bioinformatic data analyses.

Figure 0.1 Preliminary information about captured cells was used to help determine those cells to analyze and sequence. A) Normalized Hoechst dye fluorescence intensity values for cells captured in each of the six IFC captures. Asterisks represent a significant difference in fluorescence intensity between conditions with **** representing $p < 0.0001$ (unpaired t-test, two-tailed, not assuming consistent SD). Each capture shows significant differences in Hoechst fluorescence intensity depending on which condition the dye was applied to before capture on the IFC. B) cDNA concentrations (ng/µl) as measured using the Picogreen assay for each cell captured in the six IFCs used. A cutoff of ~70 ng/µl was used to select cells with sufficient cDNA from each capture for sequencing. C) Pooled cDNA concentrations from the six IFC captures according to experimental condition, heat shock or control. No significant difference was detected between cDNA concentrations of cells according to condition, $p = 0.38$ (Mann-Whitney test). D) SINGuLAR outlier analysis of the first sequencing run of single cell transcriptomes using 50 commonly-expressed genes between cells, which identified 72 single-cells for downstream analysis. 2 additional cells were manually selected from the borderline outliers, bringing the total to 74 valid cells (shown in blue) used from the first set and 10 outliers (shown in red) were rejected. E) SINGuLAR outlier analysis for the second sequencing run of single cell transcriptomes using 61 commonly-expressed genes between cells, which identified 62 valid cells (shown in blue) and 10 outliers (shown in red). One cell was manually excluded from the valid cells, bringing the total to 61 valid cells form the second sequencing run.

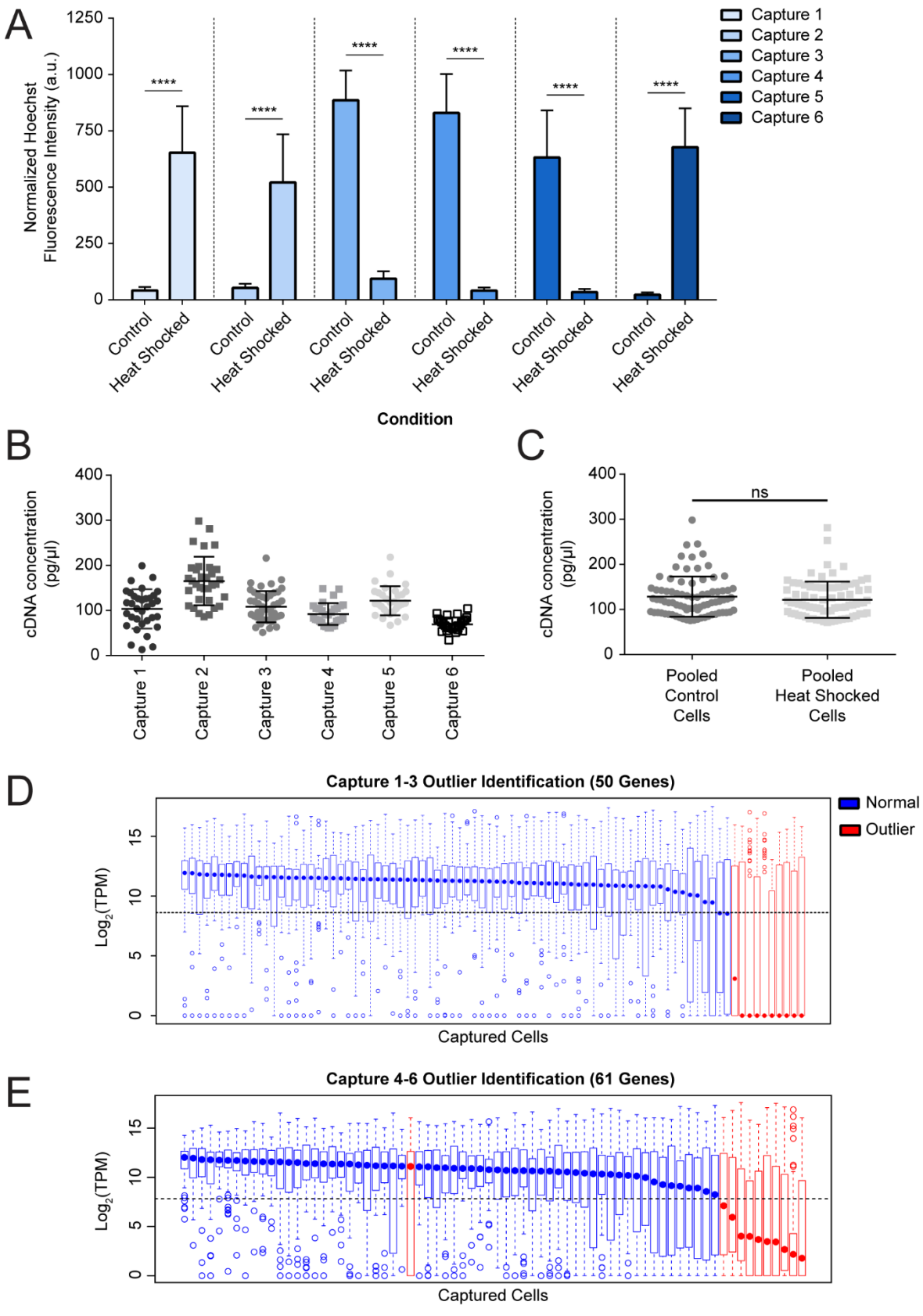
A
Normalized Hoechst Fluorescence Intensity (a.u.)
1250
1000
750
500
250
0
****
Capture 1
Capture 2
Capture 3
Capture 4
Capture 5
Capture 6
Control
Heat Shocked
Condition
B
cDNA concentration (pg/µl)
400
300
200
100
0
Capture 1
Capture 2
Capture 3
Capture 4
Capture 5
Capture 6
C
ns
Pooled Control Cells
Pooled Heat Shocked Cells
D
Capture 1-3 Outlier Identification (50 Genes)
Normal
Outlier
Log2(TPM)
Captured Cells
E
Capture 4-6 Outlier Identification (61 Genes)

3.3.2 Principal component analysis and clustering of single cells reveals three major cell groups in utricle epithelia that are separated by expression of canonical cell type markers

PCA of the first nine principal components separating the single cell transcriptomes was used to perform unsupervised cell clustering. The clearest separation of variance in the single cell transcriptome data was observed between PCs 1 and 2 showing two qualitatively distinct groupings of cells (Fig 3.2 A); however, no clear separation could be determined as a result of overlaying the heat shock and control condition information onto the PCA plots. Additional PCs within the first 9 PCs were observed to have their own clustering patterns, and we decided to include PCs 1, 2, 3, 5, and 8 in our downstream analyses. All 5 of these PCs were chosen to filter the gene expression matrix for those genes that contributed to each PC. Accordingly, it was observed that within the genes selected that significantly correlated with separation on each of the selected PCs (1, 2, 3, 5, and 8), there were transcript markers of both hair cell and supporting cell identity (see genes in Fig 3.2 C) as well as heat shock protein transcripts significantly correlated with each PC (Table 3.1). Bootstrapping analysis was then performed to assess the total number of kmeans clusters in the dataset once it had been reduced to the selected PCs. This analysis determined an ideal kmeans cluster number of k=3, and single cells were then divided into three clusters according to the kmeans separations. Upon kmeans clustering, it was possible to identify one cell that was a potential doublet and outlier from the major cell groups, H10-2_C6-CS63_5, from the 5th capture (arrows, Fig 2A-B). This cell was dropped from subsequent analyses and clustering was re-performed.

To validate marker expression, a one-way ANOVA was performed to look at DEGs between the first kmeans cluster (41 cells) and the second kmeans cluster (60 cells) to determine significantly enriched markers in each cluster (fold change ≥ 2, ANOVA FDR-adjusted p-value < 0.05, Tukey post-hoc p-value < 0.05). Gene expression for canonical cell-type markers was examined in each kmeans cluster. Examination of the expression levels of twenty-one mature HC type markers (*Bdnf, Cabp2, Espn, Smpx, Nrxn3, Ptprq, Mreg, Elmod1, Myo15, Myo6, Myo7a, Otof, Rbm24, Espnl, Calb2, Pvalb, Tomt, Gfi1, Rasd2, Atoh1, Ctbp2*) revealed 14/21 (67%) markers significantly enriched in the first kmeans cluster (*Espn, Cabp2, Smpx, Bdnf, Ptprq, Nrxn3, Mreg, Elmod1, Myo15, Myo7a, Rbm24, Espnl, Otof, Myo6*), which we then designated as the HC-type cluster (Fig 3.2 C, red). One HC marker (*Calb2*) was 'borderline' significant (i.e. between-groups p-value = 0.002 before multiple-comparisons correction). Similarly, the expression level of twenty-one SC type markers (*Anxa2, Cd9, Rbp1, S100a11, Tspan8, Cdh1, Sox9, Otog, Hes1, Tecta, Ptgds, Notch2, Jag1, Slc1a3, Otoa, Gjb2, Gjb6, Notch1, Tnfaip2, Dkk3, Sox2*) revealed 12/21 markers significantly enriched in the second kmeans cluster (*Tspan8, Tecta, Sox9, S100a11, Rbp1, Otog, Hes1, Cd9, Anxa2, Cdh1, Ptgds, Notch2*), which we then designated the SC-type cluster (Fig 3.2 C, blue). 3 supporting cell markers (*Otoa, Jag1, Slc1a3*) were 'borderline' statistically significant (i.e. between groups p-value = 0.002, 0.005, 0.03, respectively). All 42 markers that were examined are either known canonical hair cell or supporting cell markers in the inner ear, identified as expressed preferentially in utricle or cochlear hair cells or not in previous inner ear cell type gene expression studies (Burns, Kelly et al. 2015, Cai, Jen et al. 2015, Scheffer, Shen et al. 2015, Krey, Drummond et al. 2016, Yang, Scholl et al. 2016, Hickox, Wong et al. 2017), identified and validated in

the corresponding cell type in Chapter 2 using RiboTag RNA-Seq DGE analysis and immunohistochemistry, or validated by RNAScope in situ hybridization in Section 3.3.4. The third kmeans cluster did not consistently express transcripts from either group group of 21 cell type markers within the utricle epithelium. To characterize the kmeans cluster groups on a global scale, heatmap hierarchical clustering using 500 genes selected from the PCs used to separate the kmeans clusters was used to reveal a clear transcriptional pattern separating the hair cells and supporting cells using hierarchical clustering (Fig 3.2 D). Accordingly, the third kmeans cluster failed to segregate into its own group within this heatmap and was dropped from subsequent analyses.

Figure 0.2 Clustering and marker gene expression were used in determining the cell types of captured single cells. A) PCA plot of PC1 versus PC2 for the 135 valid single cells transcriptomes identified by experimental condition (heat shock in orange, control in blue). Cells cluster into two main groups but do not appear to cluster by condition alone on the first two principal components. Ellipses represent 95% confidence intervals around each cluster. B) Three unsupervised kmeans clustering groups were determined within the dataset by selecting the top 500 genes from PCs 1,2,3,5 and 8 for analysis. The kmeans clustering groups were mapped onto the single cells with cluster one in red, cluster two in blue, and cluster three in green on the PC1 versus PC2 plot. C) Normalized $\log_2$(TPM) gene expression for 41 gene markers in single cell clusters. Fourteen gene names highlighted in red correspond to hair cell marker genes significantly enriched (one-way ANOVA followed by Tukey post-hoc test, $p < 0.05$) in kmeans cluster one, identified as the hair cell cluster. Twelve gene names highlighted in blue correspond to supporting cell marker genes significantly enriched (one-way ANOVA followed by Tukey post-hoc test, $p < 0.05$) in kmeans cluster two, identified as the supporting cell cluster. D) Heatmap of normalized $\log_2$(TPM) gene expression levels for the 500 genes used in principal component filtering of single cell transcriptomes. Hierarchical clustering of cells clusters gene expression profiles into two distinct groups that correspond to the kmeans hair cell and supporting cell clusters.

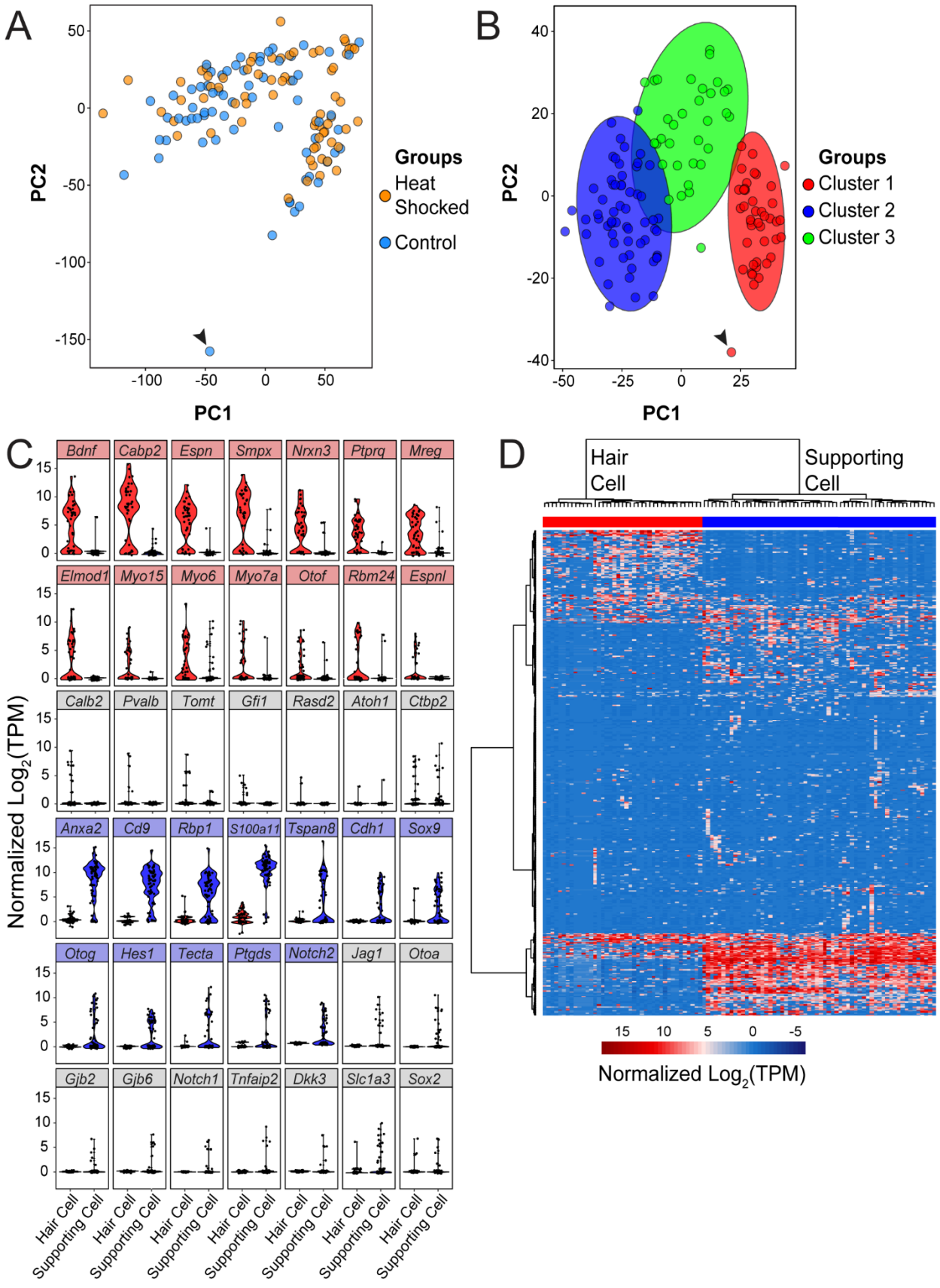
A
PC2
PC1
Groups
Heat Shocked
Control
B
PC2
PC1
Groups
Cluster 1
Cluster 2
Cluster 3
C
Bdnf
Cabp2
Espn
Smpx
Nrxn3
Ptprq
Mreg
Elmod1
Myo15
Myo6
Myo7a
Otof
Rbm24
Espnl
Calb2
Pvalb
Tomt
Gfi1
Rasd2
Atoh1
Ctbp2
Anxa2
Cd9
Rbp1
S100a11
Tspan8
Cdh1
Sox9
Otog
Hes1
Tecta
Ptgds
Notch2
Jag1
Otoa
Gjb2
Gjb6
Notch1
Tnfaip2
Dkk3
Slc1a3
Sox2
Normalized Log2(TPM)
Hair Cell
Supporting Cell
D
Hair Cell
Supporting Cell
Normalized Log2(TPM)

PC1 Gene	PC1 Correlation Coefficient	PC1 p-value
S100a11	0.73	1.11E-23
Anxa2	0.71	1.37E-21
Cd9	0.67	1.60E-18
Smpx	-0.4	2.09E-06
Bdnf	-0.4	2.06E-06
Nrxn3	-0.42	3.13E-07
Ptprq	-0.43	2.92E-07
Espn	-0.46	3.22E-08
Cabp2	-0.49	2.34E-09

PC2 Gene	PC2 Correlation Coefficient	PC2 p-value
Smpx	0.62	7.41E-16
Espn	0.61	3.40E-15
Cabp2	0.57	5.82E-13
Mreg	0.57	6.09E-13
Hspb1	-0.5	7.21E-10

PC3 Gene	PC3 Correlation Coefficient	PC3 p-value
Tecta	0.39	2.96E-06
Otog	0.38	7.35E-06

PC5 Gene	PC5 Correlation Coefficient	PC5 p-value
Hsph1	0.45	3.46E-08

PC8 Gene	PC8 Correlation Coefficient	PC8 p-value
Dnajb9	0.44	1.41E-07

Table 0.1 Gene correlations to selected PCs used in clustering of single cells. The first column shows the gene names identified as significantly correlated to PCs 1, 2, 3, 5, and 8 that were used for kmeans clustering analysis of cells. The correlation coefficient of each gene's expression level to the corresponding PC is shown in the second column. The p-value for that correlation is shown in the third column. Genes highlighted in blue correspond to genes that were identified as supporting cell markers, genes highlighted in red correspond to genes identified as hair cell markers, and genes in orange correspond to HSP genes observed in the correlations.

3.3.3 Gene ontology (GO) analysis for DEGs between cell types reveals translational machinery enrichment in supporting cells compared to hair cells and a transcriptional heat shock response in both cell types

The cell type identity assigned to each kmeans cluster (hair cell as cluster 1 and supporting cell as cluster 2 for a total of 101 cells) was combined with the experimental condition information (control or heat shocked) to produce four 'cell treatment' groups: 25 heat shocked HCs, 16 control HCs, 23 heat shocked SCs, and 37 control SCs. PCA analysis of these subgroups using the 500 genes identified in Section 3.3.2 revealed some separation of these groups according to heat shock or control condition along PC3 (Fig 3.3 A) but significant overlap was observed between conditions, indicating the variation in gene

expression due to heat shock effect was relatively smaller than the variation due to cell type between these groups.

Two primary differential gene expression comparisons were made to characterize the cell type-specific responses to heat shock: Heat shocked HCs compared to control HCs, and heat shocked SCs compared to control SCs. Genes induced by heat shock (ANOVA FDR-adjusted p-value < 0.05, fold change ≥ 1, Tukey post-hoc p-value < 0.05) from these comparisons are shown in Fig 3.3 B. The overlap of these two comparisons included 9 genes total: *Hspa1a, Hspa1b, Hspe1, Hsph1, Hspd1, Hsp90aa1, Dnaja1, Gm5844,* and *Gm12346* encoding HSP70-1, HSP70-2, HSP10, HSP105, HSP60, HSP90, HSP40-A1, and two expressed HSP90 pseudogenes, respectively. Accordingly, GO enrichment using PANTHER in the 'Biological Process' category for these 9 genes was significantly enriched for the GO term 'response to unfolded protein' (GO: 0006986, FDR-adjusted $p = 7.0 \times 10^{-7}$) and the GO term 'response to heat' (GO:0009408, FDR-adjusted $p = 5.3 \times 10^{-3}$). Both GO terms were also significantly enriched in the shared response to heat stress in Chapter 2. Thus, the shared induced response in these cell types in response to heat shock contained transcripts encoding most major families of HSPs. An exception was in the HSP27 small HSP family, of which there was one family members (*Hspb1*) that was significantly expressed only in the heat shocked SC comparison. For the heat shocked SC versus control SC comparison, 27 unique genes were induced. GO enrichment of these genes using PANTHER showed significant enrichment for the GO term 'protein folding' (GO: 0006457, FDR-adjusted $p = 1.6 \times 10^{-6}$), which contained the genes *Dnajb1*, *Hspa8*, *Chordc1*, *Clu*, and *Hspb1*. For the heat shocked HC versus control HC comparison, 16 genes total were induced. GO analysis in the 'Biological Process Slim' category for these DEGs showed enrichment for the GO

term ‘protein transport’ (GO: 0015031, FDR-adjusted p = 0.034), which contained the genes *Grtp1*, *Kdelr2*, and *Ap3b2*. Normalized $\log_2$(TPM) expression of the genes identified in the GO terms for the shared heat shock genes, heat shock SC genes, and heat shock HC genes are shown in Fig 3.3 C.

To analyze the GO enrichments for the steady-state transcriptional differences between SCs and HCs, the DGE comparison was analyzed between control HCs versus control SCs. DEGs were identified in these comparisons by filtering the ANOVA analysis based on the FDR-adjusted p-value (ANOVA FDR-adjusted p-value < 0.05) for each gene. Of the 402 DEGs identified using this cut-off, 104 DEGs were attributed to HCs (fold change > 1, Tukey post-hoc p-value < 0.05). GO term enrichment using PANTHER for the control HC DEG set revealed GO terms involving detection of mechanical stimuli and sensory receptor cell differentiation in the ‘Biological Process’ category as well as stereocilia, cilium and synapse GO terms in the ‘Cellular Component’ category. 298 DEGs were attributed to SCs (fold change < 1, Tukey post-hoc p-value < 0.05). Many more GO terms were enriched in the control SC DEG set, and several of these GO terms involved translational machinery and basement membrane in the ‘Biological Process’ category as well as ribosome assembly and cell junction maintenance in the ‘Cellular Component’ category. A sample of selected

significant GO term enrichments are shown for control HCs in Table 3.2 A, and for SCs in Table 3.2 B.

Figure 0.3 Differential gene expression analysis identifies unique and shared genes and GO groups relevant to supporting cells and hair cells in control and heat shocked conditions. A) PCA of cell treatment groups (control hair cells in dark green, control supporting cells in purple, heat shocked hair cells in light red, and heat shocked supporting cells in orange) along PCs 1 and 3 using the 500 genes from kmeans clustering. Ellipses represent 95% confidence intervals and show some separation of the four groups along PC3, but significant overlap can be seen between the cell treatment groups. Despite this, cell type is still effectively clustering each population of cells along PC1. B) Venn diagram of genes significantly induced in heat shocked hair cells and supporting cells compared to their control counterpart groups. Names shown in the overlap (dark orange) represent genes induced by both cell types after heat shock, and genes in the boxes below are the 27 unique genes significantly induced in supporting cells after heat shock (orange box) and the 7 unique genes significantly induced in hair cells after heat shock (red box). C) Normalized $\log_2$(TPM) gene expression plots for 6 of the genes expressed after heat shock (names highlighted in dark orange) in both supporting cells and hair cells following heat shock, 5 genes uniquely induced in supporting cells after heat shock (names highlighted in orange) corresponding to genes in the 'protein folding' GO term, and 3 genes uniquely induced in hair cells after heat shock (names highlighted in red) that correspond to the 'vesicle-mediated transport' GO term.

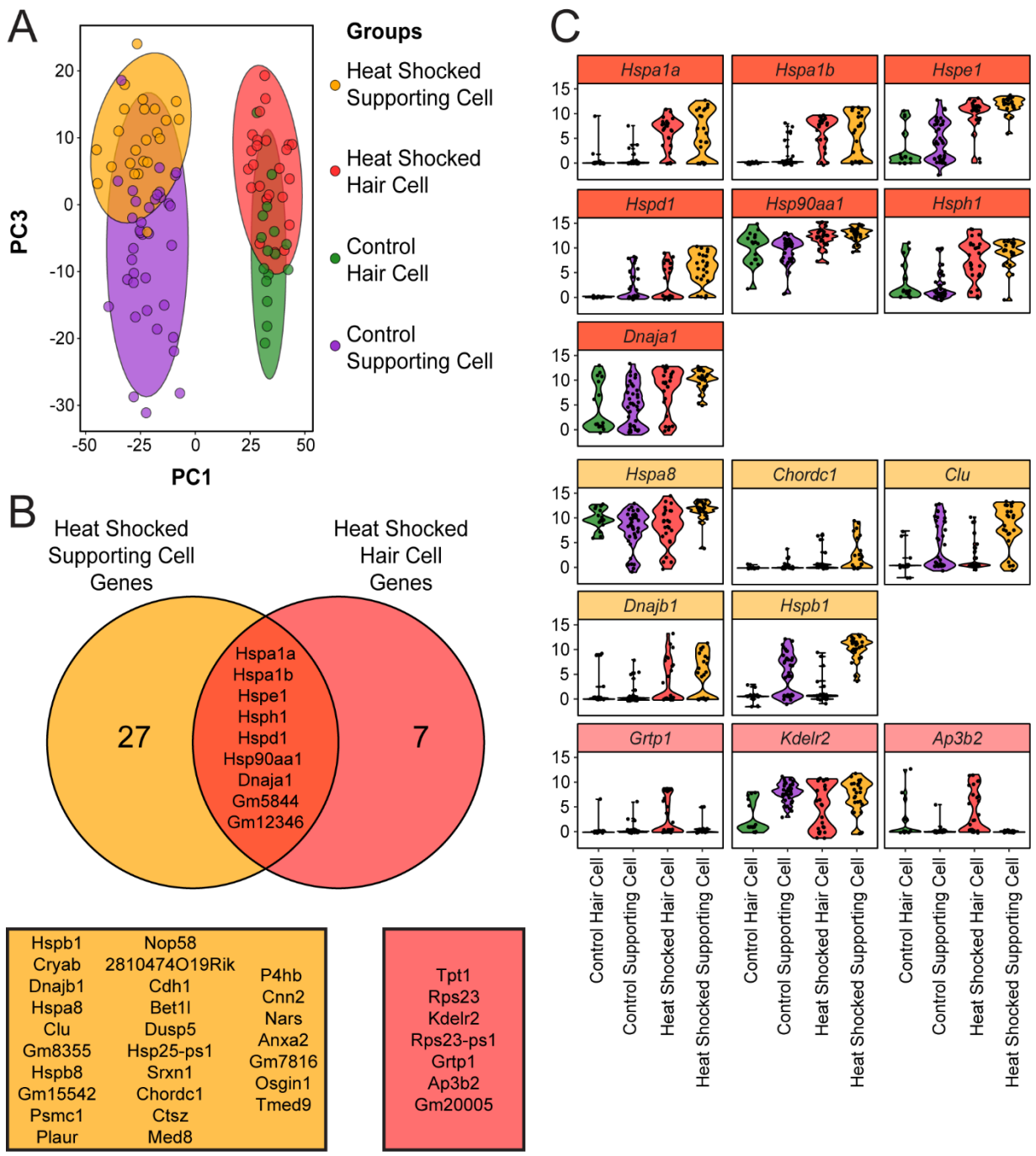
A
Groups
Heat Shocked Supporting Cell
Heat Shocked Hair Cell
Control Hair Cell
Control Supporting Cell
PC3
PC1
B
Heat Shocked Supporting Cell Genes
Heat Shocked Hair Cell Genes
27
7
Hspa1a
Hspa1b
Hspe1
Hsph1
Hspd1
Hsp90aa1
Dnaja1
Gm5844
Gm12346
Hspb1
Cryab
Dnajb1
Hspa8
Clu
Gm8355
Hspb8
Gm15542
Psmc1
Plaur
Nop58
2810474O19Rik
Cdh1
Bet1l
Dusp5
Hsp25-ps1
Srxn1
Chordc1
Ctsz
Med8
P4hb
Cnn2
Nars
Anxa2
Gm7816
Osgin1
Tmed9
Tpt1
Rps23
Kdelr2
Rps23-ps1
Grtp1
Ap3b2
Gm20005
C
Hspa1a
Hspa1b
Hspe1
Hspd1
Hsp90aa1
Hsph1
Dnaja1
Hspa8
Chordc1
Clu
Dnajb1
Hspb1
Grtp1
Kdelr2
Ap3b2
Control Hair Cell
Control Supporting Cell
Heat Shocked Hair Cell
Heat Shocked Supporting Cell

A **Hair Cell**

Biological Process GO Annotation	Genes in GO	Fold Enrichment	Adjusted p-value (FDR)
Detection of mechanical stimulus involved in sensory perception (GO:0050974)	42	22.32	3.98E-02
Inner ear receptor cell differentiation (GO:0060113)	71	16.5	2.56E-02
Sensory organ development (GO:0007423)	550	4.69	3.13E-02
Neuron development (GO:0048666)	789	3.86	3.54E-02

Cellular Component GO Annotation	Genes in GO	Fold Enrichment	Adjusted p-value (FDR)
Stereocilium bundle (GO:0032421)	57	32.89	6.35E-07
Cluster of actin-based cell projections (GO:0098862)	183	11.52	6.39E-05
Cilium (GO:0005929)	599	4.69	3.01E-03
Synapse (GO:0045202)	1022	3.21	1.54E-02

B **Supporting Cell**

Biological Process GO Annotation	Genes in GO	Fold Enrichment	Adjusted p-value (FDR)
Basement membrane (GO:0005604)	105	4.86	3.03E-02
Focal adhesion (GO:0005925)	146	4.07	3.31E-02
Polysomal ribosome (GO:0042788)	30	33.99	2.80E-12
Apicolateral plasma membrane (GO:0016327)	21	12.14	3.88E-02

Cellular Component GO Annotation	Genes in GO	Fold Enrichment	Adjusted p-value (FDR)
Ribosome assembly (GO:0042255)	70	20.64	3.61E-13
Cytoplasmic translation (GO:0002181)	62	23.3	8.44E-14
Apical junction assembly (GO:0043297)	33	15.45	5.81E-04
Positive regulation of adherens junction organization (GO:1903393)	30	14.16	3.79E-03

Table 0.2 Differential gene expression analysis identifies GO terms enriched in supporting cells and hair cells in the control condition. A) Sample of selectively-overrepresented 'Biological Process' and 'Cellular Component' GO terms returned using PANTHER on the set of 104 DEGs significantly expressed in control hair cells. B) Sample of selectively-overrepresented 'Biological Process' and 'Cellular Component' GO terms returned using PANTHER on the set of 298 DEGs significantly expressed in control supporting cells. The name of the GO term, its accession number, fold overrepresentation, number of genes in each GO term found within each DEG set, and the FDR-adjusted p-value are shown in each column.

3.3.4 In situ hybridization reveals cell-specific expression of transcripts in both SCs and HCs and validates markers of cell type identified within the single cell RNA-Seq dataset

Although in situ hybridization had previously been performed for a transcript encoding inducible HSP70 (*Hspa1b*) in Chapter 2, we also wanted to validate the localization of other markers. We chose markers of cell type that were identified in the analysis in section 3.2 (*Otof* for HCs, *Cd9* for SCs) for analysis. We were also interested in the localization of heat shock protein transcript *Hspb1*, which encodes a stress-inducible member of the HSP27 family, a smaller group of HSPs that have not been well characterized in the inner ear; however, *Hspb1* was of interest because it was a transcript that was highly enriched in the supporting cell group particularly after heat shock.

RNAScope probes measuring Otoferlin (*Otof*) expression (Fig 3.4A-D) in the utricle localize to hair cell bodies, which agrees with the enrichment for *Otof* in the HC cluster in section 3.3.2 as well as previous hair cell RNA-Seq gene expression studies (Burns, Kelly et al. 2015, Scheffer, Shen et al. 2015) and otoferlin in situ and immunohistochemistry analysis showing otoferlin protein signal at the presynaptic HC ribbon (Yasunaga, Grati et al. 1999). *Cd9* expression has been detected in early postnatal mouse utricle in previous research (Hertzano, Puligilla et al. 2010) but has not been further characterized. *Cd9* expression was highly-expressed in the SC cluster in section 3.2, and in situ hybridization results localize *Cd9* expression to the utricle sensory epithelium, specifically in supporting cell cytoplasm present in the interstices between HCs (Fig 3.5A-D).

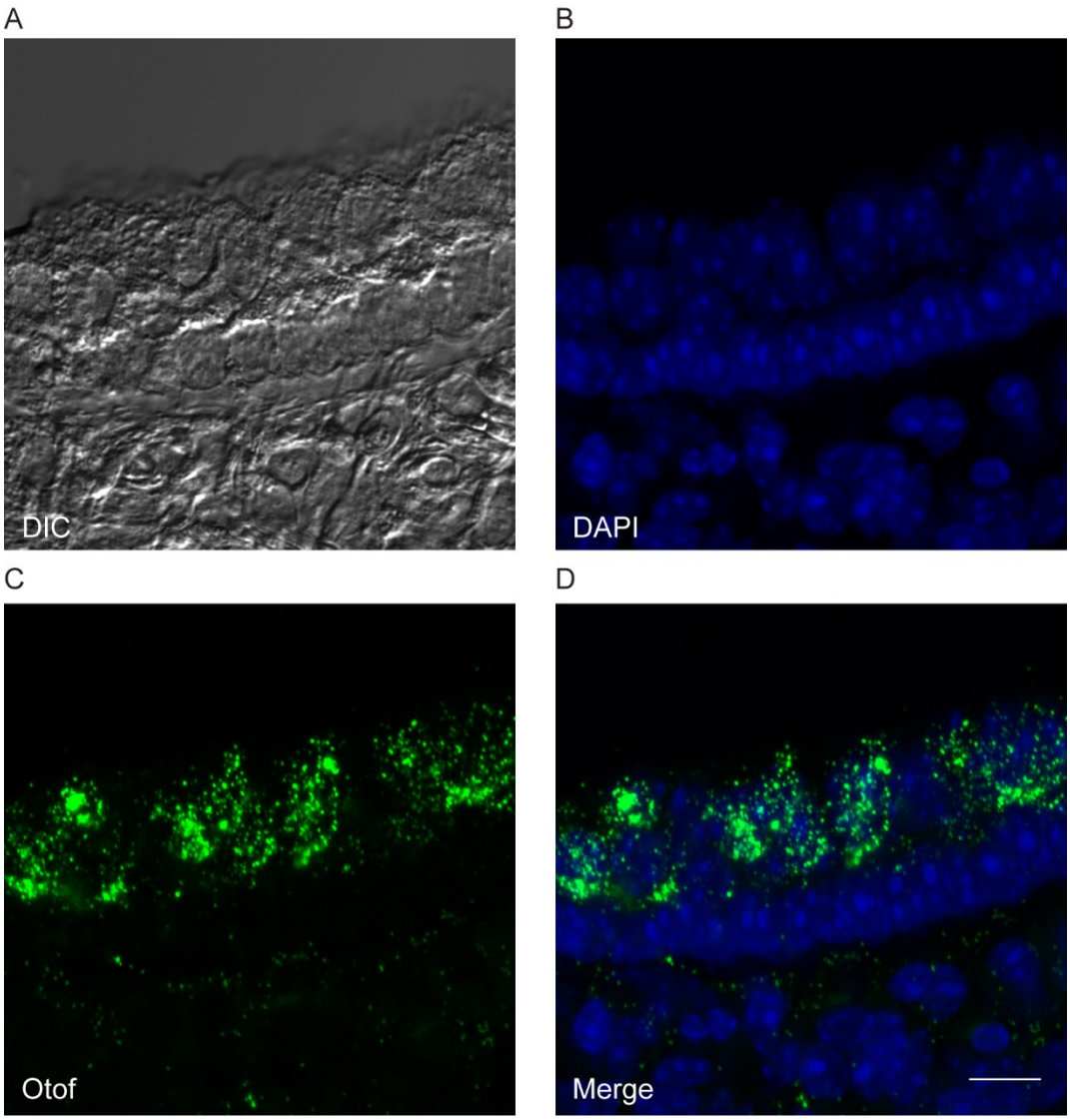

Figure 0.4 In situ hybridization signal for Otof transcript localizes to hair cell bodies in cross sections of utricle epithelium. A) Representative image of a 12 µm confocal Z-stack from control (non-heat shocked) cultured utricles hybridized with a fluorescent in situ probe against Otof transcript. Image is a Z-projection from the middle of the confocal stack. B) DAPI nuclear counterstaining. C) DIC image (single slice taken from Z-stack) showing hair cell and supporting cell morphology in utricle epithelium cross section. D) Composite image of A and B image channels showing Otof signal surrounding hair cell bodies in the apical portion of the sensory epithelium. Images were taken at 60X magnification and displayed as 3X digital zoom images. The scale bar in D represents 10 µm.

In situ hybridization for *Hspb1* (Fig 3.6) was performed in control (no heat shock) conditions (Fig 3.6 A-D) and 2 hours after heat shock (Fig 3.6 E-H, Fig 3.6 I-L displaying a 3X digital zoom on boxed regions in E-H). In the no heat shock condition, little fluorescent

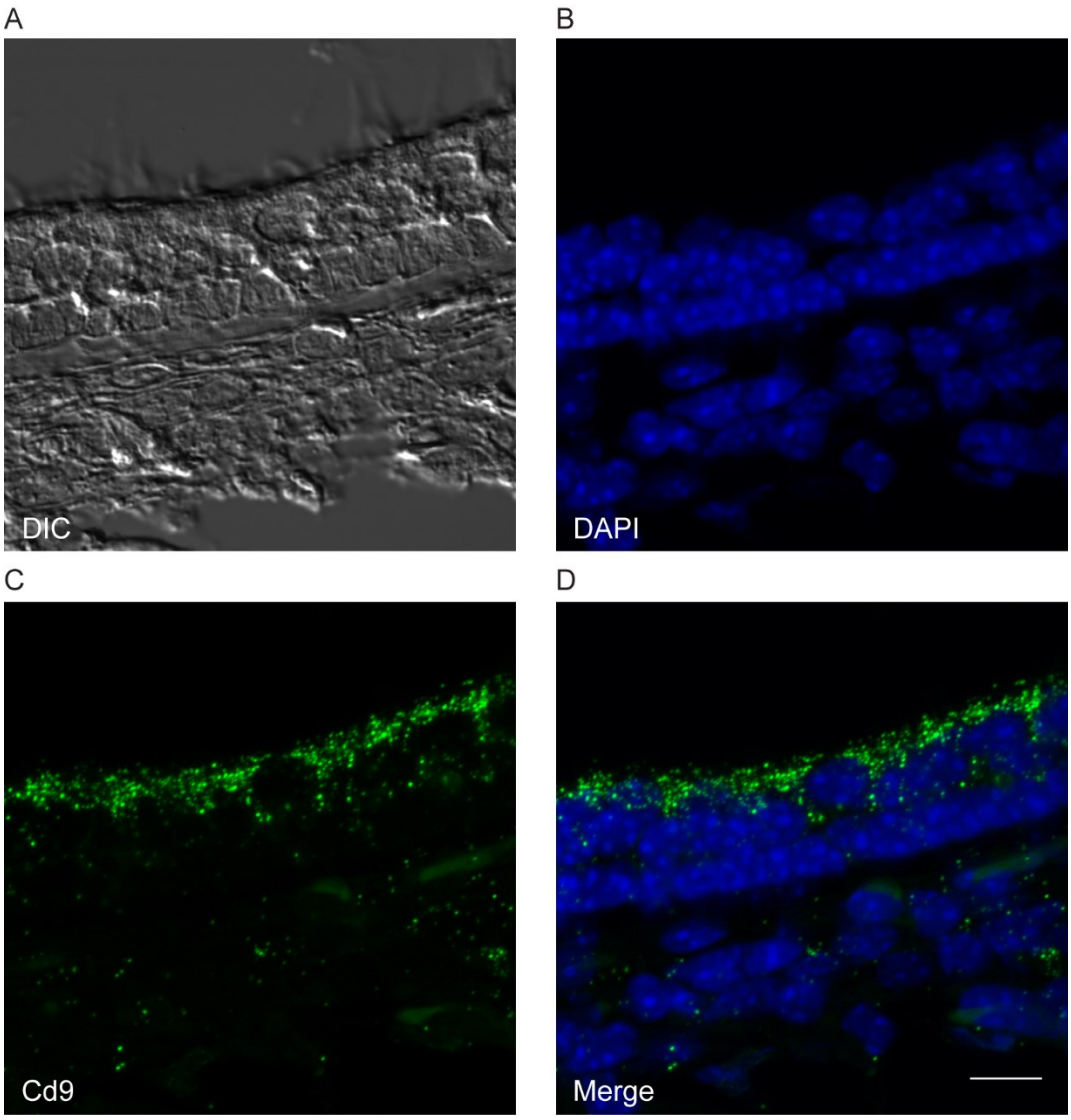

Figure 0.5 In situ hybridization signal for *Cd9* transcript localizes to supporting cell cytoplasm in cross sections of utricle epithelium. A) Representative image of a 12 µm confocal Z-stack from control cultured utricles hybridized with a fluorescent in situ probe against *Cd9* transcript. Image is a Z-projection from the middle of the confocal stack. B) DAPI nuclear counterstaining. C) DIC image (single slice taken from Z-stack) showing hair cell and supporting cell morphology in utricle epithelium cross section. D) Composite image of A and B image channels showing *CD9* signal excluded from hair cell bodies in the apical portion of the epithelia but expressed in the interstitial spaces in the medial epithelia corresponding to supporting cell bodies. Images were taken at 60X magnification and displayed as 3X digital zoom images. The scale bar in D represents 10 µm.

signal can be seen in the tissue, but there is some visible signal in the utricle epithelium and underlying stromal cell layer. In contrast, *Hspb1* in the single-cell expression data is detectable in the SC cluster both before and after heat shock. A robust signal can be

observed in the utricle epithelium following heat shock in the SC nuclear layer as well is in the interstitial space between HCs. Thus, the signal from the in situ localization suggests *Hspb1* induction in supporting cells following heat shock.

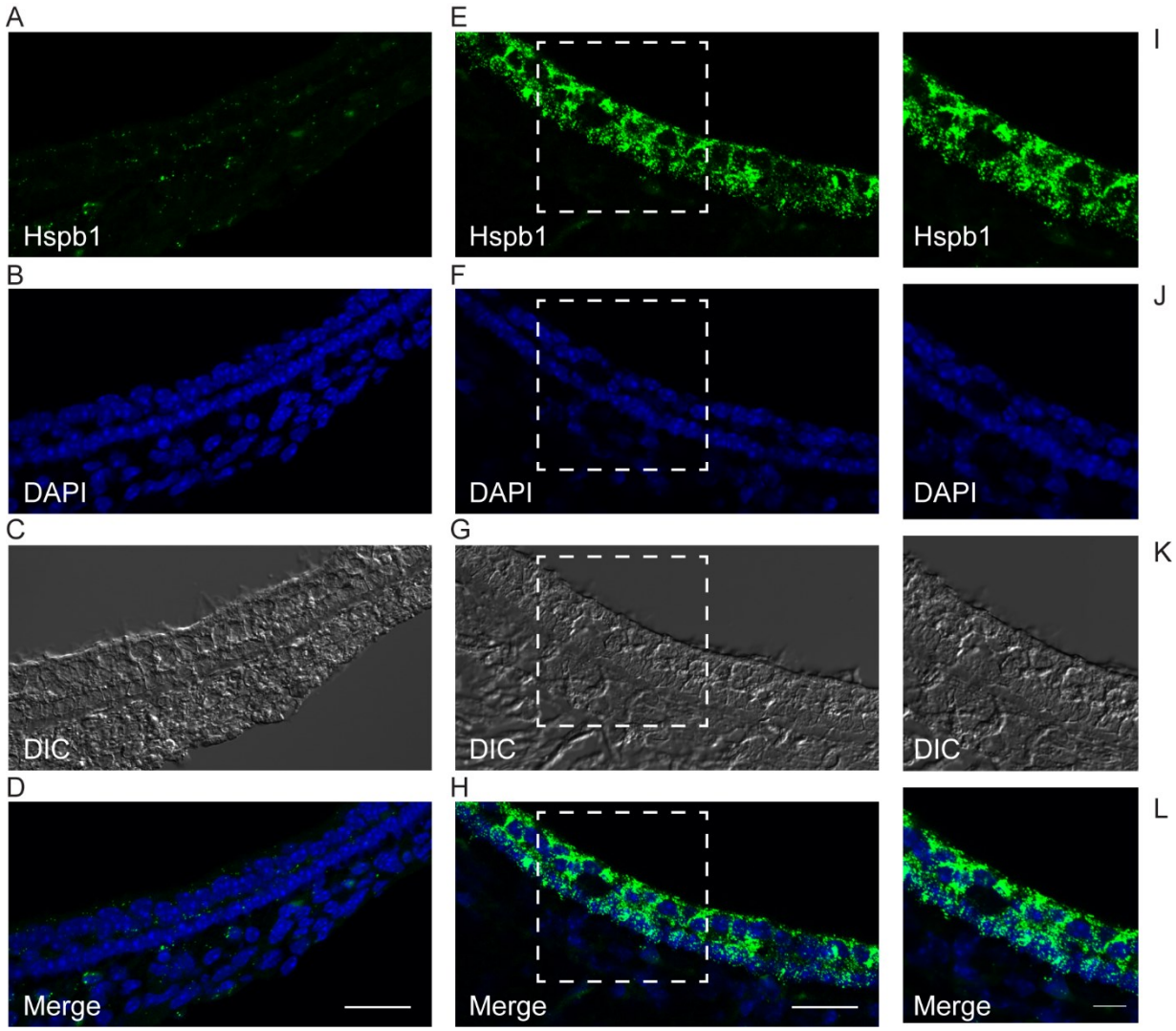

Figure 0.6 In situ hybridization signal for Hspb1 is significantly induced following heat shock in cross sections of utricle epithelium. A-D: Representative images of Hspb1 in situ hybridization of control (no heat shock) utricle cross section. A) Hspb1 fluorescent in situ signal. B) DAPI nuclear counterstaining. C) DIC image (single slice taken from Z-stack) showing hair cell and supporting cell morphology in utricle epithelium cross section. D) Composite image of A and B image channels showing a lack of Hspb1 induction in non-heat shocked utricle epithelium. E-H: Representative utricle cross section from heat shocked cultured utricles 2 hours post-heat shock hybridized with in situ probe against Hspb1 transcript. E) Hspb1 fluorescent in situ signal. F) DAPI nuclear counterstaining. G) DIC image (single slice taken from Z-stack) showing hair cell and supporting cell morphology in utricle epithelium cross section. H) Composite image of E and F show Hspb1 hybridization signal in the interstitial regions of the medial epithelium and in the basal supporting cell body region suggesting expression of Hspb1 in supporting cells following heat shock. Images were taken at 60X, scale bars in lower right corners of D and H represent 25 µm. I-L: 3X digital zoom inset of heat shocked utricle from region bounded by dashed line boxes in F-H. Scale bar in L represents 10 µm.

3.4 Discussion

In this study, we analysed single cells captured from adult utricle epithelium. Using RNA-Seq gene expression data, we clustered these cells into groups in an unsupervised manner into clusters corresponding to the two major groups of cells within the utricle sensory epithelium: supporting cells and hair cells. These cell types significantly expressed distinct collections of cell type-specific markers. By applying a supravital dye to the single cell suspensions, we were able to heat shock cells and distinguish them from one another within each cluster. The heat shock condition did not robustly cluster cell types into separate groups; however, using DGE analysis we were able to show the presence of a common heat shock response between both cell types.

Isolating transcripts exclusively from captured single cells eliminates the 'bleed-through' effect of RiboTag, which allows for a finer distinction of experimental condition in cell types; nevertheless, single cell RNA-Seq still has several important limitations. One limitation of the single cell workflow employed in this study is that there are several steps at which cells are either 'selected' or rejected based on a variety of parameters. These steps include exclusion due to low cDNA yield, exclusion due to lack of correlation to other cells during outlier analysis, or exclusion based on the number of genes detected in a given cell. Even after these first-pass steps, more cells were eliminated based on assessment canonical cell type marker expression and kmeans clustering. Thus, the presentation of the single-cell data in the results obtained here represent potentially only one possible interpretation of cell clustering and gene filtering. Ultimately, the most robust cells that were sequenced will likely represent the actual cell population, but changes in threshold criteria along any part of the platform could change the specifics of cells analysed in the dataset. Another limitation of

the single cell approach has to do with gene detection dropout. Because captured cells yield RNA concentrations that are often at the limit of detectability for current protocols, not detecting a transcript in a given sample is not always indicative of a true lack of expression (Hicks, Townes et al. 2017). The lack of significant expression of all marker genes could thus be due to the granularity of the captured single cells, but also the dropout effect could limit the number of markers detected in cells as well. The dropout is analogous to the suboptimal pulldown efficiency using the RiboTag technique that results in unenriched cell type marker transcripts that would be expected in a given IP. Due to the dropout effect, when analysing the effect of heat shock in each cell type comparison (Fig 3), it made the most sense to look only at genes induced due to heat shock in this study rather look for genes depleted by heat shock in each cell type. We were also able to isolate transcripts unique to control hair and supporting cells by comparing control hair cells to control supporting cells in a similar manner to the comparison made between control Gfi1-Cre IPs and GLAST-CreERT IPs in the Chapter 2. The fold change filtering in the single-cell DGE comparisons were used principally as qualitative filters when identifying significantly different genes between groups, since gene detection dropout may affect average expression levels for any gene within a cluster. The fact that the DEG lists between the control cell types in both experiments lead to the similar GO enrichments lends credence to the fundamental differences in transcriptional profiles between supporting cells and hair cells observed in this study and in the RiboTag analysis despite that limitation.

In situ hybridization results for *Otof*, a hair cell marker, and *Cd9*, a supporting cell marker identified in this study, show markedly different localization patterns in the utricle epithelium. *Otof* signal localized to the apical surface of the epithelium, localizing onto hair

cell bodies and nuclei visualized in the DIC and DAPI images, respectively. In contrast, the *Cd9* hybridization signal localized exclusively to interstitial spaces in the medial layer of the epithelium corresponding to areas of supporting cell cytoplasm by completely excluding more apical hair cell bodies and nuclei. One other in situ target, *Hspb1*, was chosen because it was observed that this transcript was specifically enriched in supporting cells. After heat shock, *Hspb1* signal was significantly increased in the utricle epithelium, with signal in both the basal layer of the epithelium, where supporting cell nuclei are located, as well as in the interstitial spaces in the medial layer of the epithelium similarly to *Cd9*, indicating a primarily supporting cell-based localization after heat shock. In non-heat shocked tissue, *Hspb1* signal was mostly absent, and this observation differs from the single cell expression data which shows *Hspb1* in both control and heat shocked supporting cells. This discrepancy may be an example of a transcriptional change induced in supporting cells as a result of the single cell dissociation and capture process, as HSP27 proteins can be induced by disruption of the cytoskeletal network (O'Reilly, Currie et al. 2010). Future studies may be able to elucidate differences in heat stress induction of HSPs versus stress caused by experimental factors such as cell dissociation.

Looking specifically at the transcriptional heat shock response, the majority of HSP transcript induction appears to be shared between heat shocked supporting cells and heat shocked hair cells when compared to their respective control groups in the single cell data. This shared expression includes the expression of stress-inducible HSP70 transcripts *Hspa1a* and *Hspa1b*. Interestingly, the results from the single cell study suggest a few unique genes that are expressed in each cell type. These types of results would be difficult to detect in RiboTag because of the background transcript carryover into each IP. In the single cell data,

heat shocked supporting cells appeared to significantly induce some additional genes uniquely within the 'protein folding' GO term, including a stress-inducible member of the HSP27 family, *Hspb1*. *Hspb1* is expressed under stress and is protective against toxic stimuli in the retina, which contains the highly-stratified sensory epithelium responsible for visual perception. In retinal glial cells, HSP27 immunoreactivity is high following optic nerve transection and is also induced in rat model of glaucoma injury (Krueger-Naug, Emsley et al. 2002, Kalesnykas, Niittykoski et al. 2007). Furthermore, HSP27 induction as a pre-treatment protected retinal function against ischemia (Whitlock, Agarwal et al. 2005) and also was capable of protecting retinal function in a rat model of ischemic preconditioning (Li, Roth et al. 2003). Taken in conjunction with the conclusions from the RiboTag chapter, a transcriptional heat shock response does appear to occur in both cell types. Heat shocked hair cells did not express many DEGs outside of the shared heat shock response, and even those genes expressed appeared to be weakly enriched only for the GO term 'protein transport' which is a general cellular process not associated with a stress-related GO pathway. The conclusion regarding the availability of translational machinery being the rate-limiting factor in the expression of heat shock transcripts in both supporting and hair cell types still holds given that translational machinery GO terms was also enriched for in control supporting cell DEGs. Preferential expression of *Hspb1* in supporting cells after heat shock may offer an additional layer of protective capability afforded to supporting cells following heat shock given the precedent of HSP27-mediated protection in the retina.

In summary, we have performed two cell-specific RNA-Seq studies on cells isolated from mouse cultured utricles, RiboTag RNA-Seq and single-cell RNA-Seq, and these the results of these studies have been characterized in the previous two chapters. We have

demonstrated that both methods are capable of selectively isolating cell-specific makers for both supporting cells and hair cells, which suggests that both methods are a viable means of selecting cell-specific transcripts from inner ear sensory epithelium. When considering the RiboTag dataset, DGE comparisons between heat shocked IPs were confounded by RiboTag's inability to completely deplete the IP of background RNA species from the input tissue lysate. Thus, although comparing IPs between Cre drivers afforded a robust DGE comparison in terms of enriched cell type marker genes, the primary conclusion that could be drawn from the RiboTag heat shock data was that at least one cell type responded to heat shock between hair cells and supporting cells , and the signal was carried over into the other cell type, or that both cell types responded to heat shock. Single cell RNA-Seq was then able to provide a cell-level granularity of mRNA species in the utricle epithelium, thus resolving the ambiguity inherent in the RiboTag technique without the need for modification of the RiboTag DGE analysis. Single cell RNA-Seq data, while suffering from low detectability of mRNA species due to technical limitations, was able to determine that heat shocked supporting cells and heat shocked hair cells are capable of inducing HSPs, including HSP70, following heat shock. As discussed in the RiboTag chapter, enrichment of gene ontology terms in the control state for each cell type suggested that supporting cells contain enrichment for translational machinery. A reduced ability of hair cells to translate available HSP transcripts induced by heat shock compared to supporting cells therefore may account for the previously-reported finding that supporting cells are strongly immunopositive for HSP70 while hair cells are not (May, Kramarenko et al. 2013). Gene ontology enrichments in the non-heat shocked hair cells and supporting cells strongly mirror those results observed in the RiboTag data, bolstering the idea that there are fundamental differences in steady-state

translational capability between these two cell types. Future research into cell-specific translation may further the understanding of the responses to stress in these two cell types.

3.5 Experimental contributions

I performed utricle dissection, culture, and epithelium isolation; performed single-cell capture; performed validation immunohistochemistry and in situ hybridization; prepared Nextera XT multiplexed library construction; performed bioinformatic clustering; performed enrichment analysis of DEGs and GO set overrepresentation testing. Lindsey May performed mouse breeding and genotyping and assisted in the utricle dissection, culture, and epithelium isolation process. She also assisted in performing single-cell dissociation and single-cell capture. Robert Morell performed RNA-Seq sample demultiplexing, raw read alignment, read quality analysis, and provided extensive bioinformatic guidance, and DEG analysis reporting. Daniel Martin generated the bioinformatic pipeline to align sample reads and provided extensive bioinformatic guidance. Mike Kelly in collaboration with Joseph Burns (Decibel Therapeutics, Boston MA) wrote the R scripts used to cluster single-cells, perform PCA analysis, and visualize single cell gene expression. Erich Boger performed SMART-seq cDNA generation, Nextera XT library construction, and performed the HiSeq 1500 flow cell preparation and sequencing runs. Matthew Kelley provided access to the Fluidigm C1 device and IFC imaging microscope equipment and provided guidance with the Fluidigm single-cell capture protocol.

Chapter 4: Perturbagen profiling of the inner ear heat shock response

4.1 Introduction

Hair cells are the sensory receptors of the inner ear and are susceptible to damage by a variety of stressors, referred to as ototoxins. A few lifesaving therapeutic drugs have ototoxic properties. The aminoglycoside antibiotics such as gentamicin and neomycin, used to treat drug-resistant tuberculosis and other severe infections, are one major class of widely-used therapeutics with ototoxic side effects. Other widely used ototoxic drugs include the platinum-containing antineoplastic agents such as cisplatin, which is used to treat solid tumors. The hearing and vestibular damage associated with these drugs ranges from approximately 20-30% in patients receiving aminoglycoside antibiotics (Moore, Smith et al. 1984, Lerner, Schmitt et al. 1986, Fausti, Henry et al. 1999) to as high as 75-100% of patients receiving the chemotherapeutic cisplatin (McKeage 1995).

The inner ear is capable of generating intrinsic protective signaling mechanisms to prevent the death of hair cells. Induction of heat shock proteins (HSPs) using a heat shock stress can prevent both aminoglycoside- and cisplatin-induced ototoxicity in mouse utricles in vitro (Cunningham and Brandon 2006), and this protection is dependent on heat-inducible forms of HSP70 (Taleb, Brandon et al. 2008). The heat shock response can also be induced by the pharmacological inhibition of HSP90, which induces the response by releasing the transcription factor heat shock factor 1, HSF1 (Whitesell, Bagatell et al. 2003). Protection against ototoxicity, referred to as otoprotection, using HSP90 inhibitors has been reported in in vitro experiments of rat inner ear tissue exposed to gentamicin and treated with HSP90 inhibitor geldanamycin (Yu, Szczepek et al. 2009) and in mouse inner ear tissue exposed to

kanamycin treated with HSP90 inhibitor alvespimycin (Liu, Yu et al. 2015). Pharmacological induction of other HSPs also render otoprotection in vivo as was previously shown in guinea pigs exposed to systemic cisplatin given geranylgeranylacetone, which induced three different families of HSPs (HSP27, HSP40, and HSP70) and reduced cisplatin-induced hearing loss (Lo, Wu et al. 2017). Some closely-related stress-induced proteins, such as heme oxygenase I (HO-1 aka HSP32) are also otoprotective in vitro and in vivo (Francis, Kramarenko et al. 2011, Baker, Roy et al. 2015). Thus, there is ample evidence demonstrating that HSP induction is otoprotective, and the identification of compounds that mimic heat shock has the potential to advance the development of therapies to prevent hearing loss associated with ototoxic drugs.

While there is no cell line that appropriately represents sensory hair cells, the zebrafish (*Danio rerio*) lateral line has proven a useful model system for screening compounds for their effects on sensory hair cells. Zebrafish have hair cells grouped into neuromasts, which the animal uses to detect changes in water current (Ou, Santos et al. 2010). Ototoxic drug-induced hair cell death in the zebrafish neuromast is well-characterized in response to a variety of ototoxic compounds including cisplatin, gentamicin, and neomycin (Harris, Cheng et al. 2003, Ton and Parng 2005). Molecules that are protective against cisplatin-induced ototoxicity in mammals, such as N-acetylcysteine and D-methionine, are also protective against cisplatin-induced hair cell death in zebrafish neuromasts, indicating that the zebrafish neuromast is a reasonable model system in which to screen for otoprotective compounds (Ton and Parng 2005), and substantial medium-throughput screens have been reported. A screen of 1,040 FDA-approved compounds and bioactives for protection against aminoglycoside ototoxicity revealed seven compounds, four of which inhibited hair cell

death in zebrafish neuromasts through blocking of aminoglycoside uptake into hair cells and the remaining three through inhibition of hair cell death through cell signalling mechanisms. One of the three compounds that prevent hair cell death was further validated as protective against neomycin in a model system in mouse utricle explant cultures (Ou, Cunningham et al. 2009). Another screen of 640 FDA-approved compounds against neomycin, kanamycin, gentamicin, and cisplatin revealed ten compounds that were protective against at least two of these ototoxins (Vlasits, Simon et al. 2012). Lastly, a screen of 160 ion channel modulators in zebrafish revealed 72 compounds that affected hair cell function, 13 of which protected against gentamicin damage in mouse neonatal cochlear cultures (Kenyon, Kirkwood et al. 2017).

The results of another zebrafish neuromast screen identified a novel candidate compound protective against aminoglycoside-induced hair cell death (Owens, Santos et al. 2008) that was subsequently modified into an otoprotective compound known as ORC-13661 that is protective in both rats and zebrafish in vivo (Chowdhury, Owens et al. 2018). Despite the progress made using the zebrafish model, it would be useful to be able to screen compounds in a mammalian cell line. Although a cell line, HEI-OC1, with inner ear cell type-like properties (Kalinec, Webster et al. 2003) has been developed; these cells have limitations in their cellular death responses and sensitivity to aminoglycoside ototoxicity that limit their use in otoprotection studies (Cederroth 2012, Chen, Hill et al. 2012, Kalinec, Thein et al. 2016). There are other cell models currently being developed for use in high-throughput drug screening (Kwan, Shen et al. 2015, Walters, Diao et al. 2015). The otoprotective effect of inducing HSPs through both physiological and pharmacological means suggests that these treatments share a transcriptional pattern of HSP gene expression. Knowledge of a shared

transcriptional pattern among these treatments may help identify a protected cellular state capable of preventing hair cell death.

The connectivity map (CMAP) project was developed with the goal of identifying transcriptional patterns among 164 small molecule treatments in three cell lines using gene expression microarrays (Lamb, Crawford et al. 2006). The results of CMAP were made publicly available, and this allowed investigators to query whether CMAP-tested small molecules induce similar or reverse gene expression patterns compared to disease states they might be investigating. Thus, an investigator would either be able to find compounds that could produce similar beneficial expression profiles to their biological transcriptional state of interest, or compounds that could oppose or even reverse transcriptional expression patterns associated with certain active disease expression profiles. Queries that aligned disease state to expression pattern using CMAP led to several advances, including the re-purposing of the anthelminthic microtubule polymerization inhibitor parbendazole as a potential osteoporosis therapeutic and the use of celastrol as a leptin sensitizer to treat obesity in mice (Brum, van de Peppel et al. 2015, Liu, Lee et al. 2015). The original CMAP project was expanded using the L1000 gene expression assay (Peck, Crawford et al. 2006) to increase the number of compounds and cell numbers screened as part of the NIH Library of Integrated Network-based Cellular Signatures (LINCS) initiative. In its most recent iteration, LINCS has 19,811 small molecule profiles and 5,075 gene knockdown/overexpression profiles assayed in 77 cell lines (Subramanian, Narayan et al. 2017). Investigators generating the LINCS profiles have also expanded the LINCS query tool to include a subset of this expanded dataset. As with the CMAP data, the query tool can show an investigator if there are any LINCS L1000-profiled small molecules that produce similar or opposite effects to the input gene expression

pattern of interest. In our study, we utilized the LINCS gene expression query tool to generate a list of perturbagens that matched the heat shock response gene signature in the inner ear.

4.2 Methods

4.2.1 Animals

Male and female CBA/J mice were obtained from The Jackson Laboratory. Young adult mice (age 4-8 weeks) were euthanized by CO2 inhalation followed by decapitation. Mouse animal protocols were approved by the NIDCD Institutional Animal Care and Use Committee. 5-7 days post fertilization (dpf) zebrafish larvae (wildtype, *AB strain) were maintained at 28.5ºC. Starting at 5 dpf, fish were anesthetized using MS222 (tricaine methanesulfonate, Sigma) and imaged either live or after fixation for 2 hrs with 4% paraformaldehyde. Zebrafish procedures were approved by The University of Washington Animal Care and Use Committee.

4.2.2 Organotypic Utricle Explant Culture

Utricles were dissected from both male and female CBA/J mice (age 4-8 weeks) into sterile 24-well plates as free-floating cultures (5-6 utricles pooled per well). Utricles were cultured in an incubator overnight in culture media (DMEM/F12 media supplemented with 5% fetal bovine serum (FBS, Life Technologies) and 50 U/ml penicillin G) at 37ºC (95% air/5% CO2). For induction of the heat shock response, utricles and media were transferred to a sterile 1.5 mL centrifuge tube that was placed in a water bath at 43°C for 30 minutes to induce heat shock. Utricles were then returned to the 24-well plate and recovered under

culture conditions (37ºC) for 2 hours for heat shock mRNA induction before downstream processing to extract RNA. For LINCS perturbagen gene expression tests, utricles were incubated overnight in culture media at 37ºC (95% air/5% CO2), followed by transfer into solutions containing perturbagens or a vehicle (0.1% DMSO). Following a 6-hour incubation in each perturbagen, utricles were immediately processed for RNA extraction. For LINCS perturbagen neomycin protection assays, utricles were incubated overnight in culture media at 37ºC (95% air/5% CO2), and were then exposed to each perturbagen for six hours followed by a brief 5-minute washout in culture media. They were then exposed to 2.5 mM neomycin for 24 hours. Neomycin was prepared in culture media and equilibrated at 37ºC and 5% CO2 for 3-6 hours before utricles were transferred. Following neomycin exposure, utricles were fixed and processed for immunohistochemistry.

4.2.3 RNA Extraction and Quality

RNA was extracted from 4-6 utricles according to the RNaqueous Micro kit protocol (Ambion). DNase I enzyme treatment was performed on each extracted RNA sample using the protocol in the RNaqeous DNase I kit to remove residual genomic DNA. All RNA samples were then analysed using a Bioanalyzer (Agilent) and a total RNA Pico Chip (Agilent) to assess RNA integrity number (RIN) score and RNA concentration, and for subsequent normalization of concentration for reverse transcription and qPCR. RNA samples with RIN scores of ≥ 8 were used in subsequent qPCR assays. There were some exceptions to this criterion in the RNA-Seq validation group, where the third control replicate used had a RIN score of 5.5 but did not show significantly different Ct values compared to the other control replicates. The exception to the RIN criterion in the perturbagen qPCR experiments was the third biological replicate of AT13387 exposure in utricles, which had a

RIN score of 6.3; however, there was no noticeable difference in the fold induction pattern or Ct values observed from this replicate compared to replicates with higher RIN values, so it was included in the dataset. For RNA-Seq, RIN scores and concentrations were analysed, and all replicates used had RIN scores of ≥ 8. The fourth control replicate had a RIN score of 4.5 and was dropped from subsequent analyses after RNA-Seq alignment, as it was an outlier library that had poor alignment compared to the other three control replicates.

4.2.4 cDNA/library preparation and RNA-Sequencing

Double-stranded cDNA was prepared using the SMARTer V4 Ultra Low Input Kit (Clontech). Libraries were prepared using a Nextera XT (Illumina) kit, individually barcoded, pooled to a 2 nM final pooled concentration, and sequenced on a HiSeq 1500 (Illumina) using 125 x 125 paired-end mode (trimmed to 93 x 93). Reads were aligned to the GENCODE vM4 mouse genome (GRCm38.p3) using STAR (v2.4.2a) (Dobin, Davis et al. 2013). Consensus heat shock gene expression signatures were generated by selecting those genes that three different gene expression (DGE) analysis tools identified as being significantly enriched or depleted: The analysis tools used were DESeq2 (Love, Huber et al. 2014), EdgeR (Robinson, McCarthy et al. 2010, McCarthy, Chen et al. 2012), and Limma-voom (Law, Chen et al. 2014). EdgeR and Limma-voom DEG tables were generated using Degust (Powell 2015).

4.2.5 LINCS Query tool

DGE analyses performed on the heat shocked utricle RNA-Seq data generated lists of transcripts that were either enriched or depleted by heat shock. The lists were then entered into the LINCS query tool on the LINCS Cloud website. At the time of the analysis the

query tool was hosted on LINCS Cloud (http://data.lincscloud.org.s3.amazonaws.com/index.html), and as of this publication the query tool is now hosted on the CLUE Platform (https://clue.io). The LINCS data used in the query are also available in two GEO repositories (GSE92742, GSE70138). The query tool identified transcripts from each list that it recognized based on its own directly-measured and computationally-inferred gene lists as represented by the red and blue lines in the LINCS query flowchart (see section 4.3.3, Fig 4.3 A). The transcripts that were recognized by the query tool are summarized in Appendix Table 6.1.

4.2.6 RT-qPCR gene expression assays

RNA extracted from utricles was reverse transcribed to cDNA using Taqman Reverse Transcription Reagents (Applied Biosystems), and gene targets were measured using Taqman probes normalized to *Actb* (primer-limited) multiplexed with target Taqman gene probes. qPCRs were performed on a 7500 Real Time PCR system (Applied Biosystems) for perturbagen exposure testing and RNA-Seq DEG validation, with plates prepared with Taqman Gene Expression PCR Master Mix (2X) (Applied Biosystems). Applied Biosystems qPCR results for RNA-Seq validation genes were also run independently on a Biomark HD platform using a Flex SixTM integrated fluidic circuit (IFC) (Fluidigm) according to manufacturer instructions and normalized to *Gapdh* (non-multiplexed) for fold change calculations. Briefly, cDNA samples underwent a 14-cycle PCR preamplification using relevant Taqman probes to amplify target cDNA. The Flex Six IFCTM was then primed with control line fluid using the IFC Controller HX (Fluidigm). Pre-amplified cDNA, 20X Gene Expression Master Mix (Fluidigm), Taqman Gene Expression PCR Master Mix (2X),

Taqman gene expression probes, and 2X Assay Loading Reagent were then loaded onto the primed IFC, which was then run on the Biomark HD. All Taqman probes used for qPCR experiments are listed in Appendix Table 6.2. For perturbagen gene expression testing, utricles were exposed to individual doses of perturbagen dissolved in 0.1% DMSO and compared to control utricles treated only with the 0.1% DMSO vehicle. For additional comparison, the profile of a 2-hour exposure to 0.1% DMSO vehicle was performed from Ct values obtained from the Biomark HD from vehicle-treated utricles run on the same IFC partition compared to the no heat-shocked control utricle samples from the RNA-Seq DEG validation experiment. Biological triplicate replicates (n=3) were performed for vehicle groups and perturbagen-exposed groups. For heat shock RNA-Seq DEG validation, biological triplicate replicates (n=3) for non-heat shocked and heat shocked groups were performed.

4.2.7 Immunohistochemistry and imaging

Mouse utricles: Utricle hair cell survival was assessed by counting myosin VIIa positive hair cells in utricles fixed with 4% PFA overnight at 4ºC, washed in 1X PBS (3X 15 min washes), blocked in immunohistochemistry (IHC) block buffer (1X PBS, 2% bovine serum albumin, 0.8% normal goat serum or normal donkey serum, and 0.4% Triton X-100) at RT for 3 hours. Utricles were immunostained using a mouse anti-myosin VIIa primary antibody (1:100, Developmental Studies Hybridoma Bank, 138-1) overnight at 4ºC. Utricles were then washed three times each for 15-minutes in IHC block buffer, followed by incubation in an anti-mouse Alexafluor-488 conjugated secondary antibody in IHC block buffer (1:500, ThermoFisher) followed by a 10-minute incubation using a nuclear counterstain (1:5000 Hoechst 33342, ThermoFisher) in 1X PBS followed by three 15-minute washes in 1XPBS.

Utricles were then mounted on glass slides using Fluoromount G (Southern Biotech). Hair cell counts taken from 50 x 50 μm boxes located either within the central (within the line of polarity reversal, a region that demarcates opposing orientations of hair cells in the utricle) or the peripheral (outside of the line of polarity reversal) region of the utricle, with four boxes sampled in each region.

Zebrafish: Following exposure to neomycin and perturbagen compound dose responses, zebrafish larvae (5-7 dpf) were fixed with 4% PFA (in 1X PBS) for 2 hours at RT, followed by three 15-minute washes in 1X PBS. Zebrafish larvae were then incubated for a 2-hour blocking period at room temperature (1% Triton X-100, 5% NGS in PBS). Larvae were then immunostained with mouse anti-parvalbumin primary antibody (monoclonal 1:400, Millipore MAB1572) in primary block (1% Triton X-100, 1% NGS in 1X PBS) at 4ºC overnight. Following three 15-minute washes in PBS-T (1X PBS, 1% Triton X-100), larvae were transferred into a solution containing a goat anti-mouse secondary antibody conjugated to Alexfluor-488 (1:500) in secondary block (1% NGS in 1X PBS). Larvae were washed in three 15-minute washes with PBS-T followed by three 15-minute washes in 1X PBS. Larvae were mounted using Fluoromount G on glass slides, and hair cell counts were performed on the SO1, SO2, O1, and OC1 neuromasts using an Axioplan fluorescent microscope (Zeiss) at 40X magnification as previously described (Raible and Kruse 2000, Harris, Cheng et al. 2003).

4.2.8 DASPEI Live Imaging

Zebrafish larvae were placed into 48-well plates and cultured in 300 μL embryo media (EM) (1 mM MgSO4, 120 μM KH2PO4, 74 μM Na2HPO4, 1 mM CaCl2, 500 μM KCl, 15 μM NaCl, and 500 μM NaHCO3 in dH2O) overnight. Following culture, zebrafish were

exposed to EM alone, vehicle (0.1-1% v/v DMSO depending on compound solubility or 0.1% v/v ethanol) alone, vehicle plus 200 μM neomycin, or perturbagen (10 μM, 1 μM, or 30 μM testing concentrations depending on the compound) plus neomycin for 1 hour. No toxic effect was observed as a result of vehicle exposure compared to EM alone, and no additional toxicity was observed in addition to neomycin. A list of the 42 screened perturbagens, vendor information, and location identification code for each perturbagen on the screening plate are summarized in Appendix Table 6.3. At the screening stages of the project, the compounds were identified by these plate location codes, thus we refer to these codes when we report the results of the screen. Following exposure to each compound, zebrafish were transferred into a six-well plate basket, washed twice with EM, and incubated in a solution of DASPEI (2-[4-(dimethylamino)styryl]-N-ethylpyridinium iodide) for 15 minutes, washed four times in EM, and placed into a solution of MS222 (tricaine methanesulfonate) for 5 minutes for anaesthesia. DASPEI scoring was performed using a MZ FL III fluorescent stereomicroscope (Leica Microsystems) with a DASPEI filter (excitation filter range: 450–490 nM, and barrier filter at 515 nM; Chroma Technologies) on anesthetized animals as previously described (Harris, Cheng et al. 2003). Briefly, 10 neuromasts per larva labelled with DASPEI were visualized at 5X magnification and evaluated for integrity based on a 0-2 scoring system. A score of 0 indicated an absence of all hair cells in the neuromast, 1 indicated partial loss of hair cells, and 2 indicated an intact neuromast. Scores from all 10 neuromasts were added together to give a composite DASPEI score for an individual zebrafish larva (n=10 larvae per treatment). Anesthetized animals were euthanized following scoring in an ice bath (4ºC or less) following DASPEI score determination.

4.2.9 Statistics

Statistical analyses and data visualizations were performed either in R for DGE analysis tools (including Corrplot (Wei, Simko et al. 2017) for global correlation visualization, PCAExplorer (Marini 2018) for DESeq2 PCA, heatmap, and PC gene loading visualizations) or Graphpad Prism 6 (GraphPad Software) for all other analyses. Statistical significance for zebrafish DASPEI scores was determined using the nonparametric Kruskal-Wallis test with Dunn's multiple comparisons comparing all controls and perturbagen treatments to the neomycin-only treated group. Statistical significance for zebrafish neuromast and mouse utricle hair cell counts were determined using one-way ANOVA followed by Tukey or Sidak multiple comparison post-hoc tests. Statistical significance for perturbagen qPCR fold changes was performed using multiple unpaired t-tests on ΔCt values between treatment groups with Holm-Sidak significance correction for multiple comparisons, and relative quantification of fold changes using the ΔΔCt method were then plotted. Correlations between qPCR and RNA-Seq fold changes were performed using a two-tailed Pearson correlation test. Graphs are shown with mean values ± standard deviation values unless otherwise noted, and alpha was set equal to 0.05 for statistical tests.

4.3 Results

4.3.1 RNA-Seq analysis of heat shocked mouse utricle explants produces a heat shock response transcriptional signature

We reported that exposure to non-lethal heat shock is protective against neomycin-induced hair cell death in whole-organ cultures of utricles from adult mice (Cunningham and

Brandon 2006, Taleb, Brandon et al. 2008). To determine the transcriptional profile induced by heat shock, control and heat shocked utricles were analysed by RNA-Seq. Using the DESeq2 DEG analysis in PCAExplorer, the transcriptional changes induced by heat shock were identified globally using principal component analysis (PCA). The first principal component (PC1) accounts for 75.2% of the total experimental variance in the top 500 most variable genes. Control and heat shocked groups are completely separated along the PC1 axis (Fig 4.1 A), suggesting that PC1 encompasses all the variation due to treatment group. No additional separation is contributed by PC2, which accounts for 10.5% of the variance. The top 10 genes contributing to PC1 are relevant to heat shock, including heat shock protein genes (*Hspb1, Hspb8, Hspe1, Hsph1, Hspa1a, Hspa1*b, and *Dnaja1* encoding HSP27, HSP22, HSP10, HSP105, HSP70-1, HSP70-2, and HSP40-A1 respectively) consistent with the idea that PC1 separation represents induction of the heat shock response (Fig 4.1 B). Sample-to-sample distance heatmapping of the individual heat shock and control replicates shows hierarchical clustering of individual samples according to condition, which is indicative of the heat shock treatment contributing to inter-sample correlation (Fig 4.1 C). DGE analysis of transcripts enriched in the heat shock samples relative to the control samples selected genes that met the criteria of a fold change of 2 or greater (i.e. a log2 fold change $\geq$ 1) and an adjusted p-value or q-value (FDR-corrected p-value) of 0.05 or less. 243 DEGs (Fig 4.1 D) met these selection criteria using all three analysis tools (DESeq2, Limma-voom, and EdgeR). 67 DEGs were identified as depleted in heat shock samples compared to controls (Fig 4.1 E) using a fold change of 0.5 or less and a q-value of 0.05 or less with agreement across all three analysis tools. Enriched and depleted genes identified in this

Enriched DEGs (LFC ≥ 1.0, FDR ≤ 0.05)							
Hspa1b	*Gm9817*	*Pgf*	*RP23-16N14.2*	*1700007K13Rik*	*Mknk2*	*Gm22753*	*4833407H14Rik*
Hspb1	*Gm12346*	*Diras2*	*Usp43*	*Trdj1*	*Fam107b*	*Wt1*	*Knstrn*
Hsp25-ps1	*Fgf21*	*Amigo3*	*Gm12603*	*Igf2bp2*	*Gadd45g*	*Cdh1*	*P4ha2*
Hsph1	*Ahsa2*	*Hsp90ab1*	*Pdk4*	*Slc25a38*	*Ivl*	*Wnt7b*	*Procr*
Hspa1a	*Rpph1*	*Morc4*	*Dedd2*	*Mns1*	*Rad51c*	*Hcar2*	*Osbpl3*
Dnajb1	*Fam84a*	*Il33*	*Smco3*	*Sfn*	*Cer1*	*Tnfrsf19*	*Dnd1*
Hspe1	*Gm6335*	*Zscan29*	*Proca1*	*Pitpnm3*	*Baiap2*	*Arid5b*	*Rhof*
Krt6a	*Gm8696*	*Myod1*	*Kctd18*	*Gzmm*	*Bpifc*	*Sele*	*Nr1d1*
Hspb8	*Chordc1*	*Angpt2*	*Lingo3*	*Gm14005*	*Ptprn*	*Nipal4*	*Klhdc7a*
Dnaja1	*Stip1*	*Dusp8*	*1200007C13Rik*	*Trib3*	*Sowahb*	*Lnx1*	*D330050G23Rik*
Hspa1l	*Cacybp*	*Lancl3*	*Tgfa*	*Cdr2*	*Fam46b*	*9330175E14Rik*	*Jdp2*
Bag3	*Cd83*	*Gm15459*	*Eepd1*	*Ptpn14*	*Macc1*	*Sh3bp2*	*Dusp4*
Mc4r	*Frem3*	*Gcnt2*	*Shb*	*Egr1*	*Fam83h*	*Ehd4*	*Fkbp4*
Hspd1	*Gm8337*	*Prrg4*	*F2rl1*	*4930563E18Rik*	*Gca*	*Krt80*	*Mfsd2b*
Hspe1-ps3	*Gml*	*Uspl1*	*Guca1b*	*Hhipl2*	*Bco1*	*Arc*	*Xk*
Krt1	*Aox1*	*Arl5c*	*Efhd2*	*Synpo2*	*Cnksr3*	*Gm7893*	*Myom2*
Gm7816	*Gm10382*	*Dnajb4*	*Mpzl3*	*Slc6a2*	*Ppl*	*P4ha1*	*Dkkl1*
Gm15542	*Serpinh1*	*Amotl2*	*Jun*	*Prkar1b*	*Ywhag*	*Gm14636*	*Edn1*
Hspe1-ps2	*Pmaip1*	*Cyr61*	*Srxn1*	*Ubc*	*Bend4*	*Mum1l1*	*Filip1l*
Gm12141	*Gm8326*	*Gm8428*	*Gm6368*	*Apobr*	*Dusp2*	*Gm12352*	*Vaultrc5*
Dnaja4	*Xirp1*	*Fam83g*	*Phlda2*	*Gm4262*	*Pde3b*	*Osmr*	*Prkab2*
Gm26825	*Parm1*	*Inpp5j*	*RP24-282D16.4*	*Snai3*	*Pdzd2*	*Dennd1c*	
Gm8355	*Zfand2a*	*Gm5511*	*RP23-21P10.1*	*Baiap2l1*	*Banp*	*Msl3l2*	
Hsp90aa1	*5830416P10Rik*	*Kcnk5*	*Fer1l5*	*Sapcd2*	*Gm8818*	*Pwwp2b*	
Atf3	*Ahsa1*	*Lor*	*Chka*	*Pkd1l1*	*RP23-346B12.4*	*Fam126a*	
Gm5844	*A530006G24Rik*	*Lamc2*	*Cdca2*	*Gpr75*	*Vgll3*	*Entpd3*	
Muc13	*Nog*	*Gm10069*	*Hspa4l*	*Opn3*	*Sh2d4a*	*Plin2*	
Swt1	*Gm29346*	*Sectm1b*	*Omp*	*Bhlha15*	*1700102P08Rik*	*Mthfd2*	
Tubgcp4	*Trim15*	*Arid5a*	*2310007B03Rik*	*Creb5*	*Tmcc3*	*Maff*	
Chac1	*Prickle1*	*Spsb1*	*Foxn1*	*Fhdc1*	*Dnajb2*	*Ahr*	
Hspa8	*Gm8141*	*RP24-210L3.2*	*Gprasp2*	*Rprl3*	*Gm22753*	*Fam46c*	
Pzp	*Cryab*	*Slc12a7*	*Gprasp1*	*Rgs1*	*Wt1*	*Nyap1*	

Depleted DEGs (LFC ≥ 1.0, FDR ≤ 0.05)							
Cdh19	*Fcgr2b*	*Mamdc2*	*Ramp2*	*Apba2*	*Col9a1*	*Snord13*	*Ankrd37*
Kctd12b	*Clec5a*	*Gper1*	*Zfyve28*	*Tmem88*	*Il15*	*Fcgr1*	*Mgp*
Fhl3	*Top2a*	*Dhh*	*Cd200r1*	*Ptafr*	*Pou3f1*	*Gjc3*	*Cyp1a1*
Stox1	*Tagln3*	*Plp1*	*Ndp*	*Nudt7*	*Fcgr3*	*Fam105a*	*Tnfsf10*
Smtnl2	*Slc30a3*	*Ms4a7*	*Arl11*	*Zfp773*	*C3ar1*	*Evi2a*	
Tram1l1	*Fam180a*	*Ly6c1*	*Sox18*	*Tlr13*	*Kcnj8*	*Slc25a18*	
Adh7	*Atoh1*	*Ahrr*	*Angptl2*	*Cd52*	*Meox2*	*Kcne3*	
Ushbp1	*Hpgds*	*Ccl12*	*Nxpe4*	*Mpz*	*8430408G22Rik*	*Mmp11*	
Rab19	*Gimap1*	*Scgb3a1*	*Gm29538*	*Acer2*	*Kcna1*	*Aplnr*	

Table 0.1 DEG analyses produce a transcriptional signature that are enriched or depleted by heat shock. Shown are the 243 enriched DEGs (red) and 67 depleted DEGs (blue) identified using the overlap of DESeq2, Limma-voom, and EdgeR DEG analysis tools as shown in Figure 1D ordered left-to-right in columns by the DEG magnitude of DESeq2 $\log_2$ fold changes.

analysis are summarized in Table 4.1. Taken together, these analyses indicate that whole-organ, adult mouse utricle cultures can induce a robust transcriptional heat shock response.

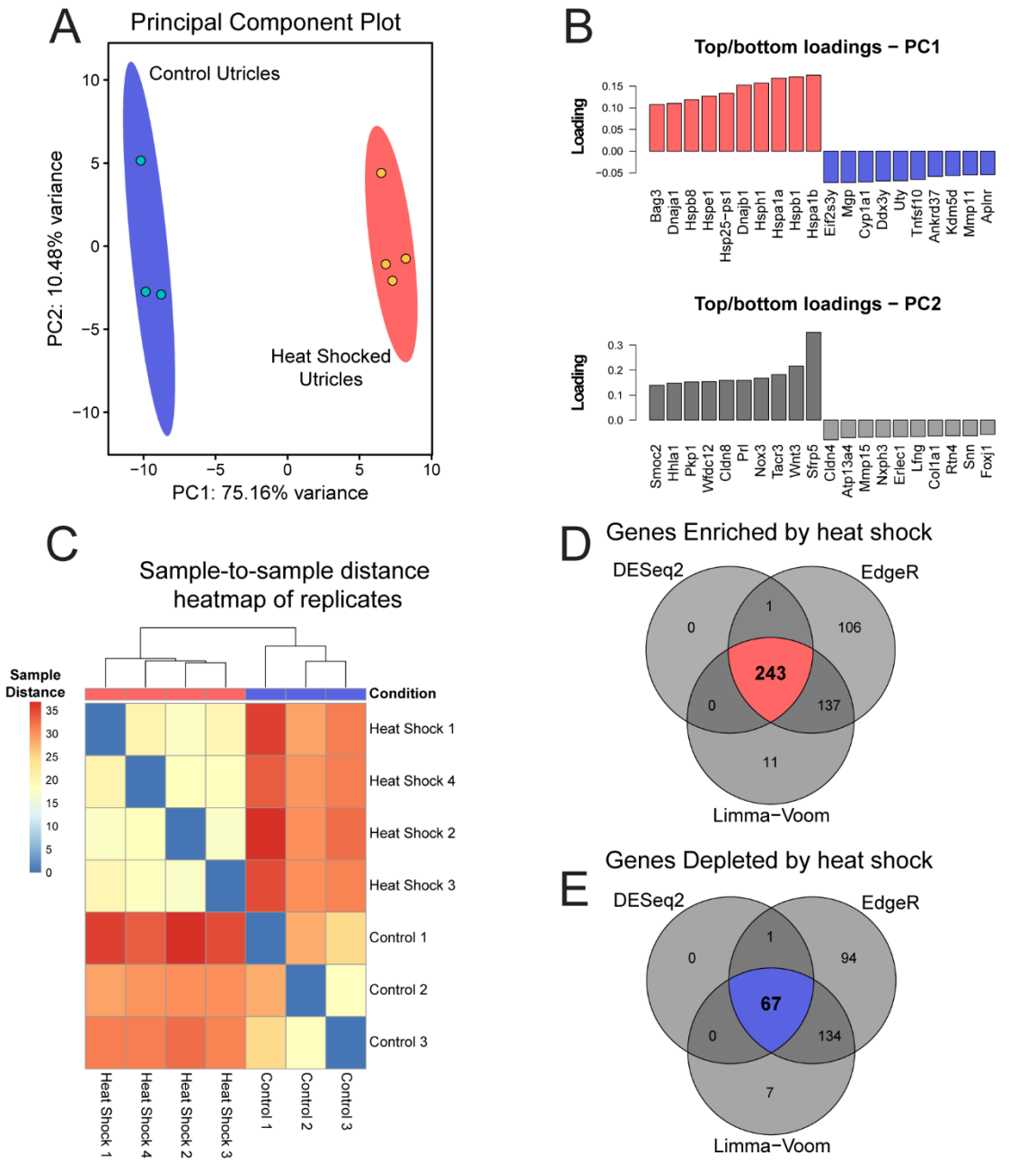

Figure 0.1 Bioinformatic analyses of whole utricle RNA-Seq data. A) PCA analysis of replicates from both heat shocked (red) and control (blue) utricles using the 500 most variable genes in the dataset. PC1 represents 75.16% of the total variance in the experimental data, and PC2 represents 10.48% of the total variance. The red (heat shock) and blue (control) ellipses around each set of replicates represent 95% confidence intervals. B) Top and bottom ten transcripts that contribute to PC1 and PC2 with PCA loading values plotted for each gene. C) Sample-to-sample distance heatmap for RNA-Seq reads with dendrograms showing hierarchical clustering of samples based on heat shock (red) and control (blue) conditions, labelled in the row above the heatmap based on sample distances. D) Results of overlapping DEGs using DESeq2, Limma-voom, and EdgeR tools with the criteria that the Log2 Fold Change value must be ≥ 1 with an adjusted p-value < 0.05 for all three analysis tools. 243 DEGs were enriched in the heat shock condition relative to control (upper Venn diagram in red), and E) 67 DEGs were depleted in the heat shock condition relative to control (lower Venn diagram in blue).

4.3.2 RT-qPCR validation of the heat shock transcriptional signature

To validate the signature of enriched and depleted DEGs, 8 genes (*Hspa1a, Hspa1b, Hspb1, Hsph1, Dnajb1, Bag3, Chac1, Cacybp*) were selected from the enriched DEG set at approximately the 80th percentile or above (ranging from the ~83rd percentile for *Cacybp* to the 100th percentile for *Hspa1b*, ordered by DESeq2 log2 fold change), and 3 genes (*Mgp*, *Tnfsf10, Gjc3*) were selected from the depleted DEG set at the 15th percentile or lower (ranging from the 0th percentile for *Tnfsf10* to the ~15th percentile for *Gjc3*, ordered by DESeq2 log2 fold change) for qPCR analysis using TaqMan probes. Independent samples of cultured utricles (n=3 per group) were prepared as heat shock or control as in the RNA-Seq experiment, and qPCR was performed on the total RNA from these samples (Fig 4.2 A). The gene expression patterns identified by RNA-Seq analysis were reproducible in this independent experiment (normalized to *Actb*), with 7/8 genes from the enriched DEG set (*Hspa1a, Hspa1b, Hspb1, Hsph1, Dnajb1, Bag3, Chac1*) significantly induced after heat shock, and 2/3 genes from the depleted DEG set (*Gjc3, Tnfsf10*) were significantly depleted. Two genes (*Cacybp* from the enriched DEG set and *Mgp* from the depleted DEG set) did not reach statistical significance after multiple corrections, but enrichment ($\Delta\Delta Ct = 0.54 \pm 0.33$, p-value = 0.10) or depletion ($\Delta\Delta Ct = -0.56 \pm 0.48$, p-value = 0.089) in the predicted directions did occur, respectively, in these genes relative to the control (no heat shock group). Although the $\log_2 FC$ values from DESeq2 and the $\log_2(\Delta\Delta Ct)$ values are not directly statistically comparable because measurements were made in different sample sets using different normalization methods, the Pearson correlation coefficient for the log-transformed fold changes for all 11 validation genes was equal to 0.91 ($p < 0.0001$) between the Taqman qPCR $\Delta\Delta Ct$ measurements and DESeq2 fold change measurements, indicative of significant

correlation between the two independent sets of gene expression patterns as a result of heat shock.

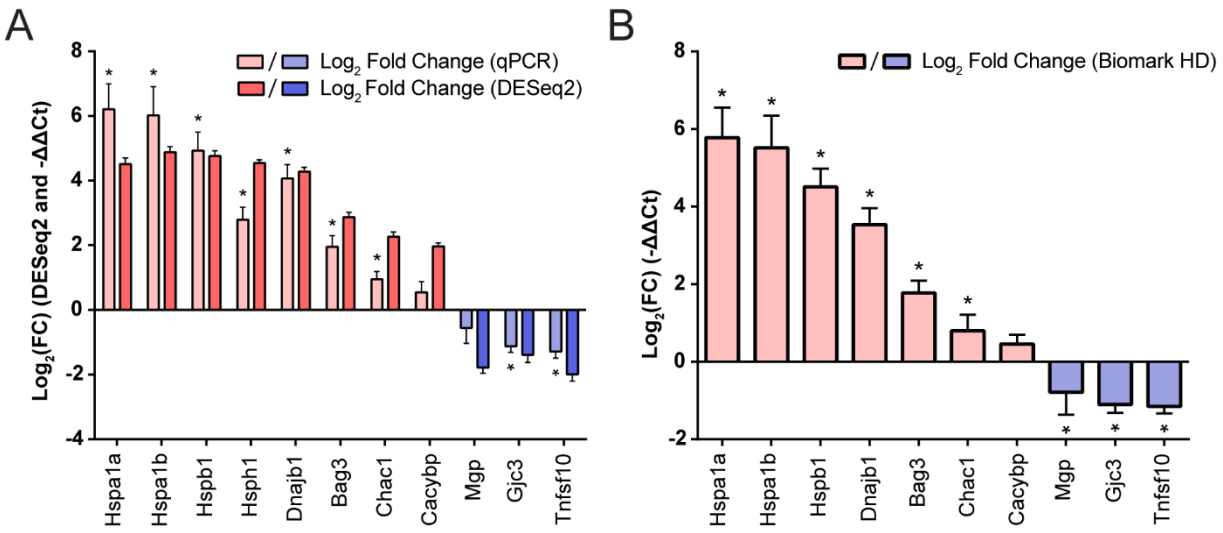

Figure 0.2 Validation of the utricle heat shock transcriptional signature. A) Fold changes (mean ± standard error values calculated from the DESeq2 model) of 8 enriched and 3 depleted DEGs from the heat shock transcriptional signature are shown in dark red and dark blue, respectively. RT-qPCR fold changes (normalized to *Actb*) performed in independent replicates (n=3 biological replicates per group) for the same 8 enriched and 3 depleted DEGs are shown in light red and light blue, respectively. B) Fold changes from independent replicates for 7 enriched and 3 depleted DEGs from the heat shock signature normalized to *Gapdh* and measured on the Biomark HD system show similar induction patterns as measured in A. Asterisks indicate statistically significant ($p < 0.05$) differences in heat shock ΔCt values compared to control replicates as measured by multiple unpaired t-tests following Holm-Sidak multiple comparison correction, represented above each ΔΔCt value.

Changes in gene expression between heat shock and control replicates were also validated for 10 validation genes on a Fluidigm Biomark HD platform (Fig 4.2 B). Expression of 6/7 genes *(Hspa1a, Hspa1b, Hspb1, Dnajb1, Bag3, Chac1*) from the enriched DEG set were significantly induced. Expression of 3/3 genes (*Mgp, Gjc3, Tnfsf10*) were significantly reduced. Again, changes in *Cacybp* were found to be not statistically significant. Reduction of *Mgp* expression was statistically significant on the Biomark HD platform, in contrast to the TaqMan analysis, suggesting a borderline significance of this result in concordance with the RNA-Seq DEG results. Furthermore, ΔΔCt values of all 10 genes calculated using both the Applied Biosystems and the Biomark HD platforms were highly correlated, with a Pearson correlation coefficient of 0.99 ($p < 0.0001$), indicating

agreement between the two sets of measurements. Together our validation experiments using two different methods confirm the overall pattern of upregulated and downregulated genes we observed in the RNA-Seq dataset.

4.3.3 LINCS query of the heat shock gene expression signature provides a ranking of small molecule perturbagens that produce similar and opposite transcriptional profiles in tested cell lines

We used LINCS analysis to compare signatures of DEGs found after heat shock to a database of gene expression changes found after treatment with a perturbagen drug library. The iteration of the LINCS tool used in this analysis (Subramanian, Narayan et al. 2017) accepted lists of enriched and depleted genes without fold change information. The LINCS L1000 assay measured 987 landmark genes and then computationally inferred the expression level of a total of approximately 11K genes (Duan, Flynn et al. 2014, Subramanian, Narayan et al. 2017). As a consequence, the query tool recognized only a subset of the genes entered from our RNA-Seq experiment: The LINCS query tool recognized 115/243 (47.3%) transcripts in the enriched DEGs, and 28/67 (41.8%) transcripts in the depleted DEGs (Fig 3A) for a total of 143/310 (46.1%) of the DEGs from our RNA-Seq dataset. The LINCS tool then ranked 3,273 perturbagen signatures according to how closely they induced gene expression changes that matched the input DEG subset from our heat shock RNA-Seq data. The ranking for each perturbagen signature was the normalized average rank match from 4 separate cell lines tested with each perturbagen in LINCS (Fig 4.3 B). 'Matching' perturbagens are those that produce gene expression changes similar to our input DEG list of transcripts enriched/depleted by heat shock (≥ 90th percentile mean rank). 'Reverse'

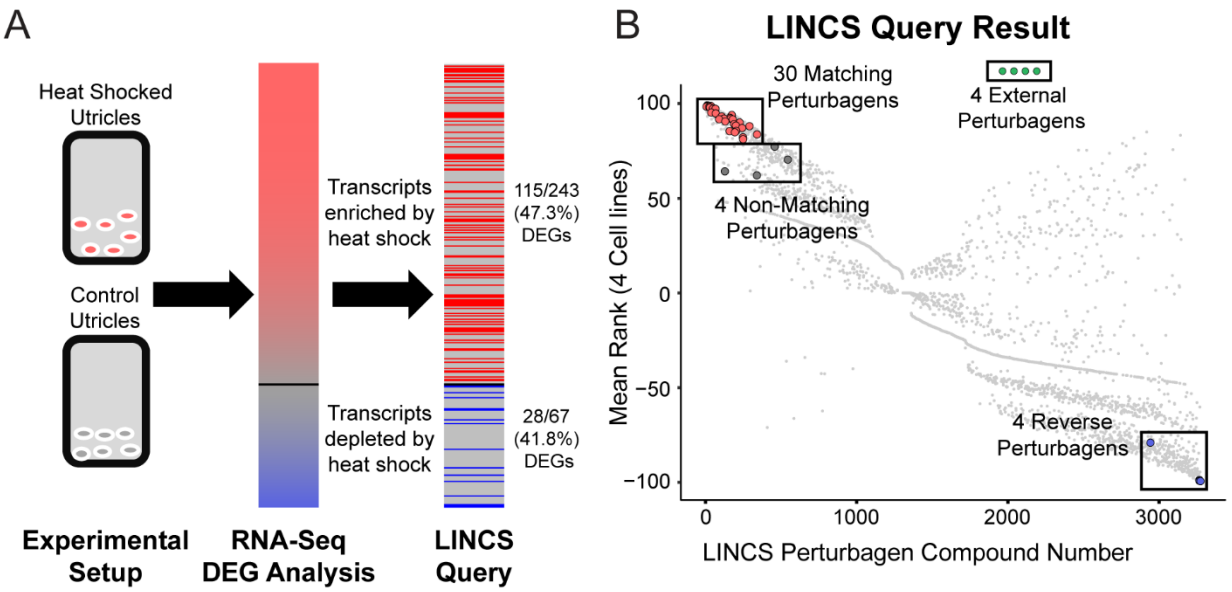

C

Matching Perturbagens					Non-Matching Perturbagens	Reverse Perturbagens	External Perturbagens
NSC 632839	Arachidonyl-trifluoro-methane	CYT-997	Parthenolide	Butein	Anisomycin	Sirolimus	Ranolazine
BCI-hydrochloride	Withaferin-a	SB-225002	BIIB021	Tanespimycin	Trichostatin-A	PP-1	AT-13387
MG-132	BNTX maleate	MLN-4924	Pifithrin-mu	Xanthohumol	Menadione	AZD-6482	STA-9090
MLN-2238	Phenethyl-isothiocyanate	Etoposide	Disulfiram	Ursolic-Acid	Elesclomol	Fostamatinib	AEG 3482
Manumycin-A	CMPD-1	NVP-AUY922	Geldanamycin	PU-H71			
SA-792709	Sappanone a	Alvespimycin	Teniposide	Piperlongumine			

Figure 0.3 LINCS identification of small molecule perturbagens that mimic the heat shock transcriptional signature. A) Schematic of the LINCS workflow. Utricle cultures were analysed by RNA-Seq to obtain a DEG signature of transcripts enriched or depleted by heat shock compared to control (red/blue gradient bar representing DEGs in Figure 1D and Table 1). The DEG signature was used as input for the LINCS Query tool, which recognized 115/243 (47.3%) enriched DEGs and 28/67 (41.8%) depleted DEGs. B) Scatterplot of the 3,273 small molecule perturbagen signatures in the LINCS Query database showing the normalized rank match in four core LINCS cell lines compared to the input signature from heat shocked utricles. A subset of the LINCS-identified perturbagens was selected and screened for otoprotection and induction of the heat shock DEG signature. Thirty matching perturbagens (shown in red) were selected from the ≥ 90th percentile of all LINCS signatures that matched the input DEG signature of heat shocked utricles. Four perturbagens (dark gray) between the 80th and 90th percentiles were selected as non-matching perturbagens. Four perturbagens (blue) that yielded the opposite signature to the input DEG signature were chosen as reverse perturbagens. Four compounds (green) chemically similar to LINCS-identified compounds were added as external comparisons to the LINCS dataset. C) The 30 matching perturbagen compound names are in red. The four non-matching perturbagen names are shown in gray; the four reverse perturbagen names are in blue, and the four external perturbagen names are in green.

perturbagens are those that produce gene expression changes that are opposite from our input list (≤ 10th percentile mean rank). Our analysis revealed 328 matching and reverse

perturbagen signatures using these cut offs. Small molecules that were chosen for analysis from outside of the LINCS dataset we refer to as 'external' perturbagens (Fig 4.3 B).

We selected a subset of perturbagens to test whether the protective effect of heat shock in hair cells could be reproduced (or reversed) by a small molecule. Thirty matching perturbagens (Fig 4.3 B-C, red) and four reverse perturbagens (Fig 4.3 B-C, blue) were chosen for further analysis. In addition, four 'non-matching' perturbagens were chosen from below the 90th percentile LINCS ranking (Fig 4.3 B-C, gray). Four 'external' perturbagen molecules related to matching perturbagens but not found in the LINCS analysis were also selected for screening (Fig 4.3 B-C, green). Thus, the LINCS query tool allowed us to design a targeted list of compounds capable of either matching or inverting our input gene expression signature.

4.3.4 Matching LINCS perturbagens share drug classifications and have precedent in existing literature for hair cell protection against ototoxic drugs

The LINCS-generated list of matching perturbagens included some classes of drugs that are known to protect hair cells. The molecular targets and signature rankings for each perturbagen in the screen are listed in Table 4.2. Six out of the 30 matching LINCS perturbagens are HSP90 inhibitors (NVP-AUY922, Alvespimycin, BIIB021, Geldanamycin, Tanespimycin, PU-H71), which is not surprising given that HSP90 inhibition results in transcriptional activation of HSPs via the transcription factor Hsf1 (Whitesell, Bagatell et al. 2003). Two members of the HSP90 inhibitor group, Alvespimycin and Geldanamycin, are protective against aminoglycoside-induced hair cell death (Yu, Szczepek et al. 2009, Liu, Yu et al. 2015) and can induce expression of HSPs in inner ear tissue. For this reason, we

selected two additional HSP90 inhibitors (AT-13387, STA-9090) to examine as well as another known HSP inducer, AEG 3482 (Salehi, Morris et al. 2006). Some additional compounds from the LINCS matching list were either known otoprotectants or were chemically related to known otoprotectants. These included proteasome inhibitors MG-132 and MLN-2238, the mitochondrial p53/HSP70 inhibitor pifithrin-μ, and the anti-inflammatory compound piperlogumine (Coffin, Rubel et al. 2013, Coffin, Williamson et al. 2013, Yadav, Choi et al. 2014). Thus, the results of the LINCS query are supported by literature indicating that several matching perturbagens are known to be protective in the inner ear.

Table 0.2 A detailed list of the 42 compounds chosen for otoprotection screening identified in Figure 4.3 B. The compound names, putative molecular targets or functions and the mean normalized rank in four cell lines compared to the input DEG signature are shown in separate columns. The compounds are color-coded to show matching perturbagens in red, non-matching perturbagens in gray, reverse perturbagens in blue, and external perturbagens in green.

Drug name	Description	Rank Score
NSC 632839	Ubiquitin isopeptidase inhibitor	99.1
BCI-hydrochloride	MAP kinase phosphatase (Dusp6) inhibitor	98.9
MG-132	Proteasome inhibitor	98.8
MLN-2238	Proteasome inhibitor	98.8
Manumycin-A	Farnesyltransferase inhibitor, NFkB pathway inhibitor	98.4
SA-792709	Retinoid receptor gamma agonist	98.2
Arachidonyl-trifluoro-methane	Cytosolic phospholipase inhibitor	97.9
Withaferin-a	Acetylcholinesterase inhibitor, Butyrylcholinesterase inhibitor, IKK inhibitor, NFkB pathway inhibitor, PKC inhibitor	97.3
BNTX maleate	δ1 opioid receptor antagonist	97.2
Phenethyl-isothiocyanate	Cancer cell growth inhibitor	95.2
CMPD-1	MAPKAPK2 inhibitor	94.9
Sappanone a	Hsf1 inducer	94
CYT-997	Tubulin Polymerization inhibitor	93.2
SB-225002	CXCR2 chemokine receptor antagonist	92.5
MLN-4924	NEDD activating enzyme inhibitor	92.1
Etoposide	Topoisomerase inhibitor	92.1
NVP-AUY922	HSP90 inhibitor	91.7
Alvespimycin	HSP90 inhibitor	91.6
Parthenolide	NFkB pathway inhibitor, adiponectin receptor agonist	90.6
BIIB021	HSP90 inhibitor	90
Pifithrin-mu	HSP70 inhibitor	89.2
Disulfiram	Aldehyde dehydrogenase inhibitor, DNA methyltransferase inhibitor, TRPA1 agonist	88.4
Geldanamycin	HSP90 inhibitor	88.1
Teniposide	Topoisomerase inhibitor, DNA repair enzyme inhibitor, mitotic inhibitor	87.1
Butein	Angiotensin converting enzyme inhibitor, epidermal growth factor receptor (EGFR) inhibitor	85.6
Tanespimycin	HSP90 inhibitor	85.5
Xanthohumol	Aromatase inhibitor, diacylglycerol O acyltransferase inhibitor, valosin containing protein inhibitor	84.9
Ursolic-Acid	Antioxidant/General Antiinflammatory	83.7
PU-H71	HSP90 inhibitor	82.2
Piperlongumine	Glutathione transferase inhibitor	81.2
Anisomycin	DNA synthesis inhibitor	77.2
Trichostatin-A	HDAC inhibitor, CDK expression enhancer, ID1 expression inhibitor	70.4
Menadione	CDC inhibitor, mitochondrial DNA polymerase inhibitor,	64.2
Elesclomol	Apoptosis stimulant, HSP agonist, HSP inducer, oxidative stress inducer, topoisomerase inhibitor	62.1
Sirolimus	mTOR inhibitor	-79.1
PP-1	Arc inhibitor, Abl kinase inhibitor	-98.8
AZD-6482	PI3K inhibitor	-99.2
Fostamatinib	Syk inhibitor, FLT3 inhibitor	-99.4
Ranolazine	Fatty acid oxidation partial inhibitor, Sodium channel blocker	External
AT-13387	HSP90 inhibitor	External
STA-9090	HSP90 inhibitor	External
AEG 3482	HSP inducer, JNK inhibitor	External

4.3.5 Screening selected LINCS perturbagens in zebrafish against neomycin-induced ototoxicity yielded three otoprotective hits

Based on the results above, we screened the 42 LINCS-identified perturbagens and related compounds (Fig 4.3 C) for their effects on aminoglycoside-induced hair cell death in the zebrafish lateral line. Zebrafish larvae (5-7 dpf) were exposed to neomycin (200 μM) for 1 hr in the presence or absence of each perturbagen (10 μM). Ten neuromasts on each fish were scored (ranging between 0-2 per neuromast) based on the observer's estimate of the fluorescence intensity of the DASPEI label (Harris, Cheng et al. 2003) (see Methods section 4.2.8). Screening was performed in batches, with each 48-well plate including its own positive and negative controls (Fig 4). The previously-identified otoprotective compound ORC-13661 (10 μM) (Chowdhury, Owens et al. 2018), used as a positive control, demonstrated consistent significant protection from 200 μM neomycin (Fig 4.4A-D and Fig 4.4. G-H, green bars). The criteria for a compound to be called protective in the initial screen was to achieve statistical significance ($p < 0.05$) as compared to the neomycin alone group based on the DASPEI score. The significant protective effect had to then be replicated in a secondary validation screen. Some compounds look quite close in terms of DASPEI score in the initial screen (Fig 4.4 A-C) but were discarded after failing validation in a secondary screen. Protective "hits" identified in the initial perturbagen screen were AT13387 (plate location H1) (Fig 4.4 A, brown bar, $p = 0.01$) and Pifithrin-μ (G3) (Fig 4.4 B, pink bar, $p = 0.048$). The protective effects of each of these compounds were then validated in a replication experiment (Fig 4.4 G, $p = 0.04$ and 0.0009, respectively). AEG 3482 (C5) (Fig 4.4 C, blue bar) was not significantly protective at 10 μM. However, a follow-up round of screening was performed at alternative doses for some compounds based on specificity for

the molecular targets and compound activities listed from vendors. AEG 3482 has a reported EC50 value of 20 μM in the prevention of neuronal death caused by nerve growth factor (NGF) withdrawal (Salehi, Morris et al. 2006), so a high concentration (30 μM) was attempted in the DASPEI assay (Fig 4.4 E, blue) and was found to be significantly protective ($p = 0.0003$). The protective effect of AEG 3482 was then replicated in a subsequent experiment (Fig 4.4 F). Certain highly specific compounds (MG-132, MLN-2238, PU-H71) were also screened at a lower concentration (1 μM), and results from the either high or low dose were then validated. MG-132 (D3) and MLN-2238 (H2) were each significantly protective in the first round of the low-dose screen (Fig 4E, $p = 0.02$, and $p = 0.0075$, respectively); however, the protective effect of these two perturbagens was not replicated in the validation screen (Fig 4.4 F, $p = 0.33$ and 0.32, respectively) and so they were not examined further.

Figure 0.4 LINCS-identified perturbagen screening in zebrafish revealed three compounds that protect against neomycin-induced hair cell death in lateral line neuromasts. A-D: DASPEI screening of perturbagens against neomycin-induced ototoxicity in zebrafish neuromasts. Negative controls (-) are shown in light gray (n=5-10 zebrafish per bar); vehicle controls (0.1-1% DMSO or 0.1% ethanol) are shown in gray (n=5-10), and positive controls with the otoprotective compound ORC-13661 are shown in green (n=5-10). 200 μM neomycin (red) resulted in significant hair cell death (n=10-20). Perturbagens that were either not protective or were protective but failed to replicate in a validation experiment are shown in dark gray. Three perturbagens, designated according to their locations on the culture plate as C5 (blue), G3 (pink), and H1 (brown), were protective against neomycin-induced hair cell death in this screen (n=10 for all perturbagen treatment bars). A) DASPEI scores from the first screen of perturbagens tested at 10 μM against 200 μM neomycin. H1 (AT-13387, brown) was protective in this batch. B) DASPEI scores from the second batch of perturbagens screened at 10 μM against 200 μM neomycin. G3 (Pifithrin-μ, pink) was identified as a protective hit in this batch. C) Third batch of compounds screened at 10 μM against 200 μM neomycin. C5 (AEG 3482, blue) was later identified as a hit at a different concentration but was not significantly protective at 10 μM ($p > 0.05$). D) Remaining batch of perturbagens screened at 1% DMSO and 10 μM concentration to increase solubility. E-G: E) DASPEI scores using a batch of compounds at alternative high or low doses. C5 was identified as a hit at 30 μM. F) DASPEI scores from the C5 validation screen of alternative high or low dose compounds. G) DASPEI scores from the validation experiment for 10 μM H1 and 10 μM G3 hits demonstrating a repeatable protective effect against 200 μM neomycin. Asterisks represent adjusted p-values for Dunn's multiple comparisons test following a Kruskal-Wallis test for treatment with * representing $p \leq 0.05$, ** representing $p \leq 0.01$, *** representing $p < 0.001$, **** representing $p < 0.0001$, and 'ns' (not significant) representing $p > 0.05$. All error bars in A-G represent ± S.D. values.

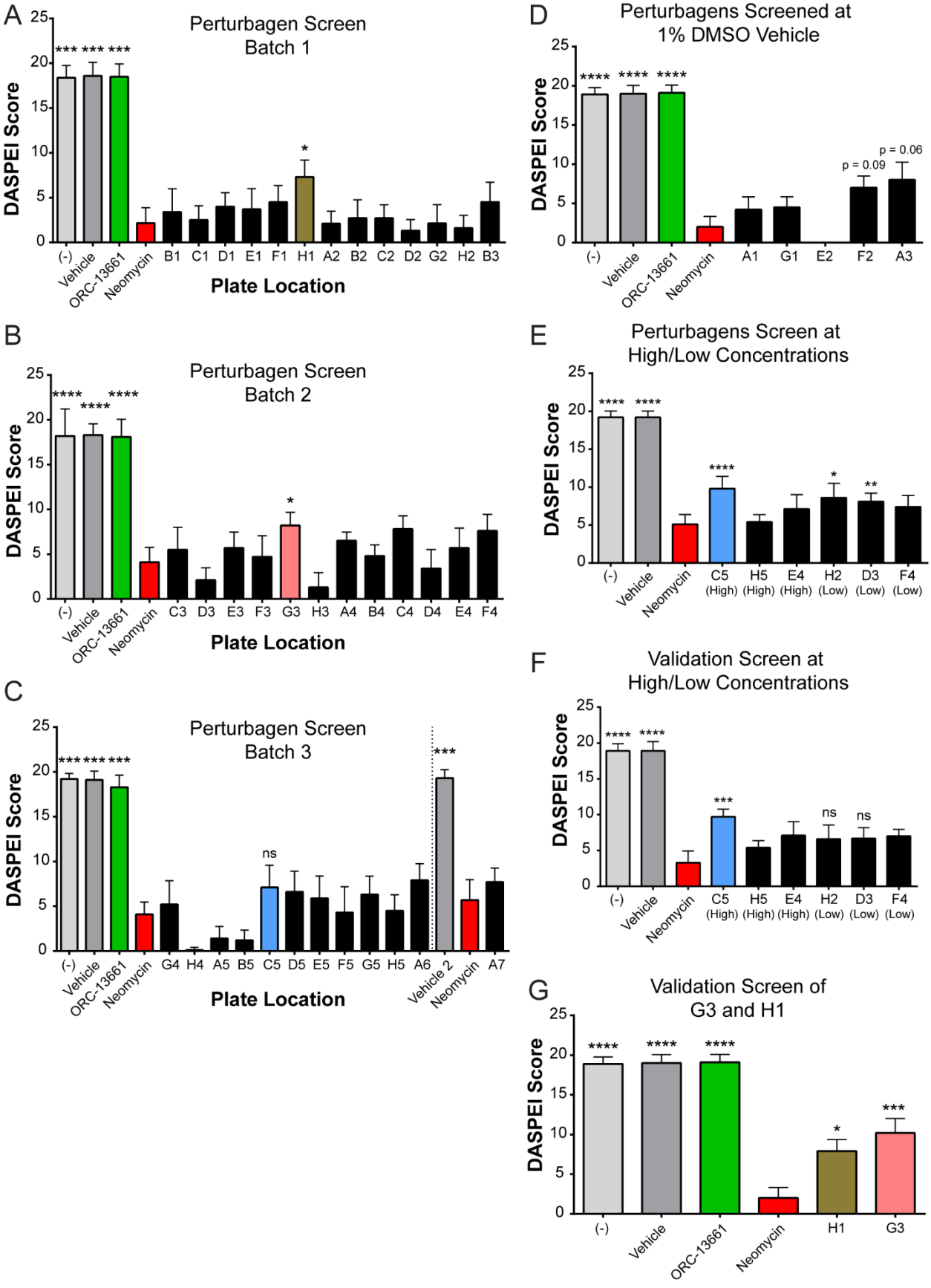
A
Perturbagen Screen
Batch 1
DASPEI Score
Plate Location
(-)
Vehicle
ORC-13661
Neomycin
B1 C1 D1 E1 F1 H1 A2 B2 C2 D2 G2 H2 B3
B
Perturbagen Screen
Batch 2
DASPEI Score
Plate Location
(-)
Vehicle
ORC-13661
Neomycin
C3 D3 E3 F3 G3 H3 A4 B4 C4 D4 E4 F4
C
Perturbagen Screen
Batch 3
DASPEI Score
Plate Location
(-)
Vehicle
ORC-13661
Neomycin
G4 H4 A5 B5 C5 D5 E5 F5 G5 H5 A6
Vehicle 2
Neomycin
A7
ns
D
Perturbagens Screened at
1% DMSO Vehicle
DASPEI Score
p = 0.09
p = 0.06
(-)
Vehicle
ORC-13661
Neomycin
A1 G1 E2 F2 A3
E
Perturbagens Screen at
High/Low Concentrations
DASPEI Score
(-)
Vehicle
Neomycin
C5 (High)
H5 (High)
E4 (High)
H2 (Low)
D3 (Low)
F4 (Low)
F
Validation Screen at
High/Low Concentrations
DASPEI Score
ns
(-)
Vehicle
Neomycin
C5 (High)
H5 (High)
E4 (High)
H2 (Low)
D3 (Low)
F4 (Low)
G
Validation Screen of
G3 and H1
DASPEI Score
(-)
Vehicle
ORC-13661
Neomycin
H1
G3

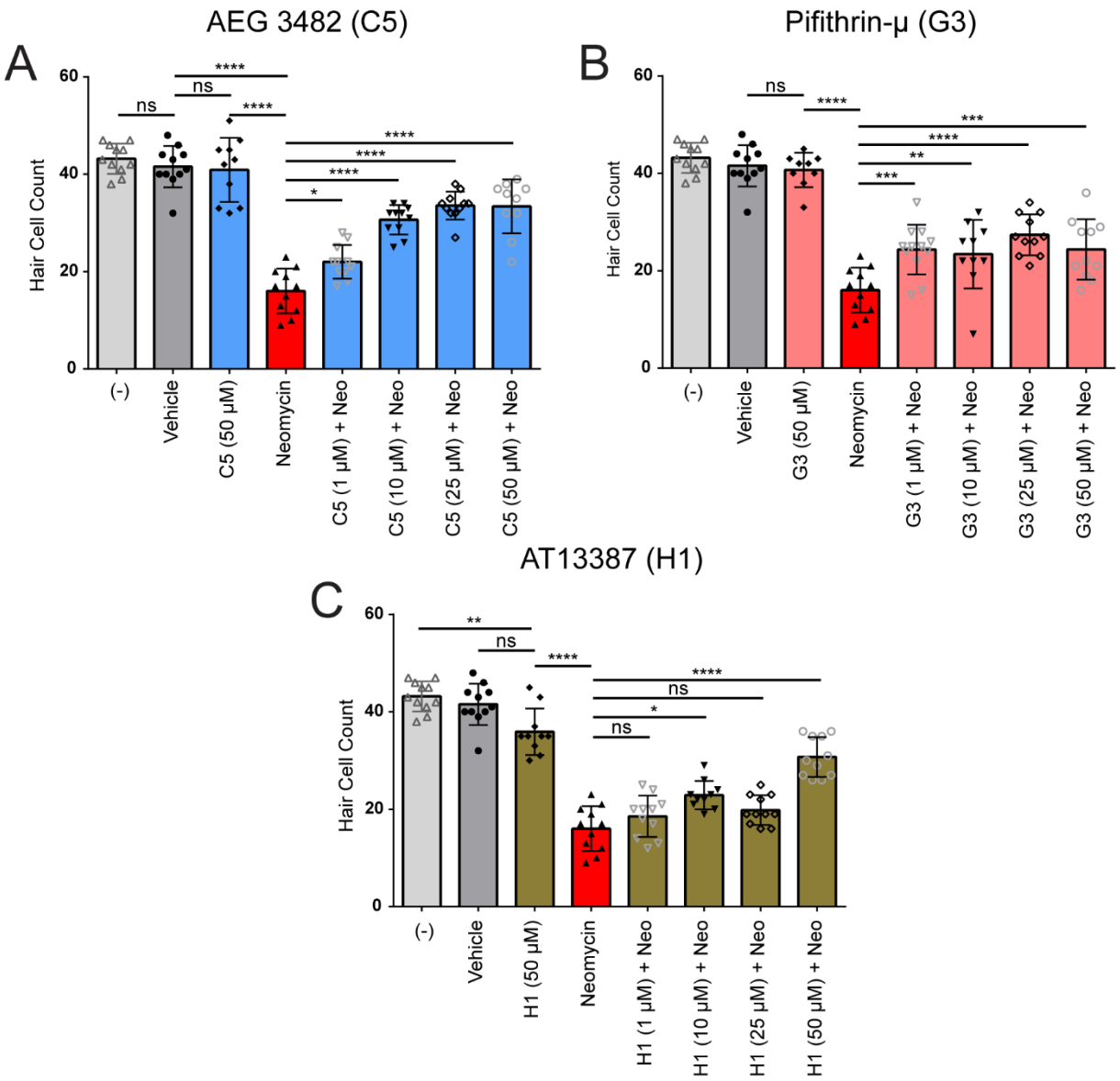

Figure 0.5 All perturbagen hits show protection against neomycin-induced hair cell death at multiple doses. A) Dose response relationship for C5 (AEG 3482, blue). Hair cells were counted from anti-parvalbumin-labelled neuromasts. B) Dose- response relationship for G3 (Pifithrin-µ, pink) C) Dose-response relationship for H1 (AT-13387, brown). Negative control, vehicle, and neomycin plus vehicle groups are identical in all three experiments, as all doses for all three drugs were tested in the same experiment (n=8-10 per group) but are stratified into separate graphs for clarity of the comparisons being made. Asterisks represent adjusted p-values from Sidak multiple comparisons test following one-way ANOVA with * representing $p \leq 0.05$, ** representing $p \leq 0.01$, *** representing $p < 0.001$, **** representing $p < 0.0001$, and 'ns' (not significant) representing $p > 0.05$. All error bars in A-C represent ± S.D. values.

Following identification and validation of the three perturbagen hits (AT13387, Pifithrin-µ, AEG 3482) in the DASPEI screen, we examined the dose-response relationship of each of these compounds. Each compound was tested at 1, 10, 25, and 50 µM as co-treatment with

200 μM neomycin for 1 hr. The highest concentration (50 μM) for each perturbagen was tested without neomycin to evaluate its potential toxicity. Treatment with AEG 3482 showed a clear dose-response relationship, with survival of hair cells significantly increasing with increasing concentrations of AEG 3482 with neomycin compared to neomycin alone (Fig 4.5 A, blue bars, $p < 0.05$ at 1 μM, $p < 0.0001$ at 5, 10, 25, and 50 μM). Treatment with Pifithrin-μ did not show a dose-response relationship, but rather demonstrated significant protection against neomycin at all doses tested (Fig 4.5 B, pink bars, $p < 0.001$ at 1 μM, $p < 0.01$ at 5 μM, $p < 0.0001$ at 10 μM, $p < 0.001$ at 50 μM). AT13387 treatment resulted in an inconsistent protective effect, with significant protection observed at the 10 μM and 50 μM doses (Fig 4.5 C, brown bars, $p = 0.0033$ at 10 μM and $p < 0.0001$ at 50 μM) but not at 25 μM. The results of the DASPEI screen and dose-response assays indicate that AEG 3482, Pifithrin-μ, and AT13387 can protect against neomycin-induced hair cell death in zebrafish lateral line neuromasts.

4.3.6 LINCS hits induce the heat shock transcriptional expression signature in cultured mouse utricles

In order to examine the transcriptional response of the three protective compounds in a mammalian system, we applied each compound to whole organ cultures of utricles from adult mice (Brandon, Voelkel-Johnson et al. 2012). Seven of the eight transcripts validated by qPCR analysis that were increased after heat shock (*Hspa1a, Hspa1a, Hspb1, Dnajb1, Hsph1, Bag3, Chac1*) were examined with an additional two enriched genes from the RNA-Seq data (*Hspe1* and *Hmox1*), and three of the transcripts validated by qPCR that were depleted after heat shock (*Mgp, Gcj3, Tnfsf10*) were measured after perturbagen exposure. Each perturbagen was administered as a six-hour pre-treatment followed by immediate RNA

extraction. DESeq2 fold changes are shown in Fig 4.6 A. No significant changes in expression of heat shock signature genes was noted in utricles treated with vehicle alone (0.1% DMSO) (Fig 4.6 B). Treatment with AEG 3482 (Fig 4.6 C) resulted in significant induction of 7/9 transcripts in the heat shock transcriptional signature (*Hspa1a, Hspa1b, Hspb1, Dnajb1, Hsph1, Hmox1, Chac1*; $p < 0.05$, multiple unpaired two-tailed t-tests with Holm-Sidak multiple comparisons adjustment) and significantly reduced expression of 2/3 heat shock-depleted transcripts (*Gjc3, Tnfsf10*). Pifithrin-μ (Fig 4.6 D) significantly induced 9/9 heat shock-enriched transcripts and significantly reduced 2/3 heat shock-depleted transcripts (*Gjc3, Tnfsf10*). AT13387 significantly induced expression of 8/9 heat shock-induced transcripts (*Hspa1a, Hspa1b, Dnajb1, Hspb1, Hspe1, Hsph1, Bag3, Chac1*) and reduced expression of 0/3 heat shock-depleted transcripts. The gene expression profile of AZD-6482, one of the LINCS reverse perturbagens, (i.e., in the bottom 10th percentile of LINCS-identified perturbagens), (Fig 4.6 F) induced expression of only 1/9 heat shock-induced transcripts genes (*Hmox1*), and significantly induced expression of 1/3 heat shock-depleted transcripts (*Tnfsf10*). Individual fold-change magnitudes differed for each perturbagen. For example, *Hmox1* enrichment differed substantially, with AEG-3482 and Pifithrin-μ exposures resulting in significant and considerable Hmox1 induction (roughly 16-fold and 23-fold induction compared to vehicle treatment, respectively), whereas AT13387 induced only modest Hmox1 expression (roughly 1.6-fold) compared to vehicle treatment. No direct statistical comparison between qPCR gene expression patterns from each perturbagen treatment can be made, due to differences in vehicle-treated samples and inter-plate variability; however, we observed significant positive Pearson correlation coefficients between heat shock and AEG 3482 (0.71, $p = 0.009$), Pifithrin-μ (0.80, $p = 0.002$), and

AT13387 (0.86, p = 0.0003) treatments. A significant negative Pearson correlation coefficient was observed between heat shock and AZD-6482 (-0.74, p = 0.006) treatment, and there was no significant correlation between vehicle treatment and heat shock (-0.33, p = 0.38), AEG 3482 (-0.14, p = 0.72), Pifithrin-μ (-0.15, p = 0.69), AT13387 (-0.26, p = 0.50), or AZD-6482 (0.29, p=0.44) treatments (See Appendix Figure 6.1). Taken together, these data indicate that each perturbagen hit that was protective in zebrafish induced a gene expression signature in mouse utricle that resembled the heat shock transcriptional signature.

Figure 0.6 The perturbagen hits induce the heat shock transcriptional signature in cultured mouse utricles. Gene signature profiling was performed using Taqman qPCR probes. A) The heat shock transcriptional profile. Shown are Log_2 fold changes (from DESeq2 DEG analysis) for heat shocked utricles compared to controls. Asterisks indicate significance, and error bars are ± SE for each Log_2 fold change. B) The vehicle used for the perturbagens does not induce a heat shock transcriptional signature. Shown are Log_2 fold changes (ΔΔCt) for genes measured in utricles exposed to 0.1% DMSO vehicle compared to non-heat shocked control utricles normalized to *Gapdh* using the Biomark HD platform. C-F: Examination of the transcriptional signatures induced by three perturbagen hits and one reverse hit. Gene expression was measured in 7 enriched and 3 depleted DEGs from the RNA-Seq DEG signature validation in Figure 4.2 in addition to two additional genes, *Hmox1* and *Hspe1* on the Applied Biosystems platform. C) AEG 3482 induces the heat shock transcriptional signature in utricles. Shown are Log2 fold changes (ΔΔCt) in utricles treated with AEG3482 (25 μM) normalized to *Actb*. D) Pifithrin-μ induces the heat shock transcriptional signature in utricles. Shown are Log_2 fold changes (ΔΔCt) in utricles treated with pifithrin-μ compared to vehicle. E) AT-13387 induces the heat shock transcriptional signature in utricles. Shown are Log_2 fold changes (ΔΔCt) in utricles treated with AT-13387 compared to vehicle. F) The reverse perturbagen AZD-6482 does not induce the heat shock transcriptional signature. Shown are Log_2 fold changes in utricles treated with AZD-6482 compared to vehicle. Asterisks in A-D indicate significant ($p < 0.05$) ΔCt differences compared to DMSO vehicle ΔCt values in multiple unpaired t-tests following Holm-Sidak multiple comparison correction (n=3 biological replicates per group).

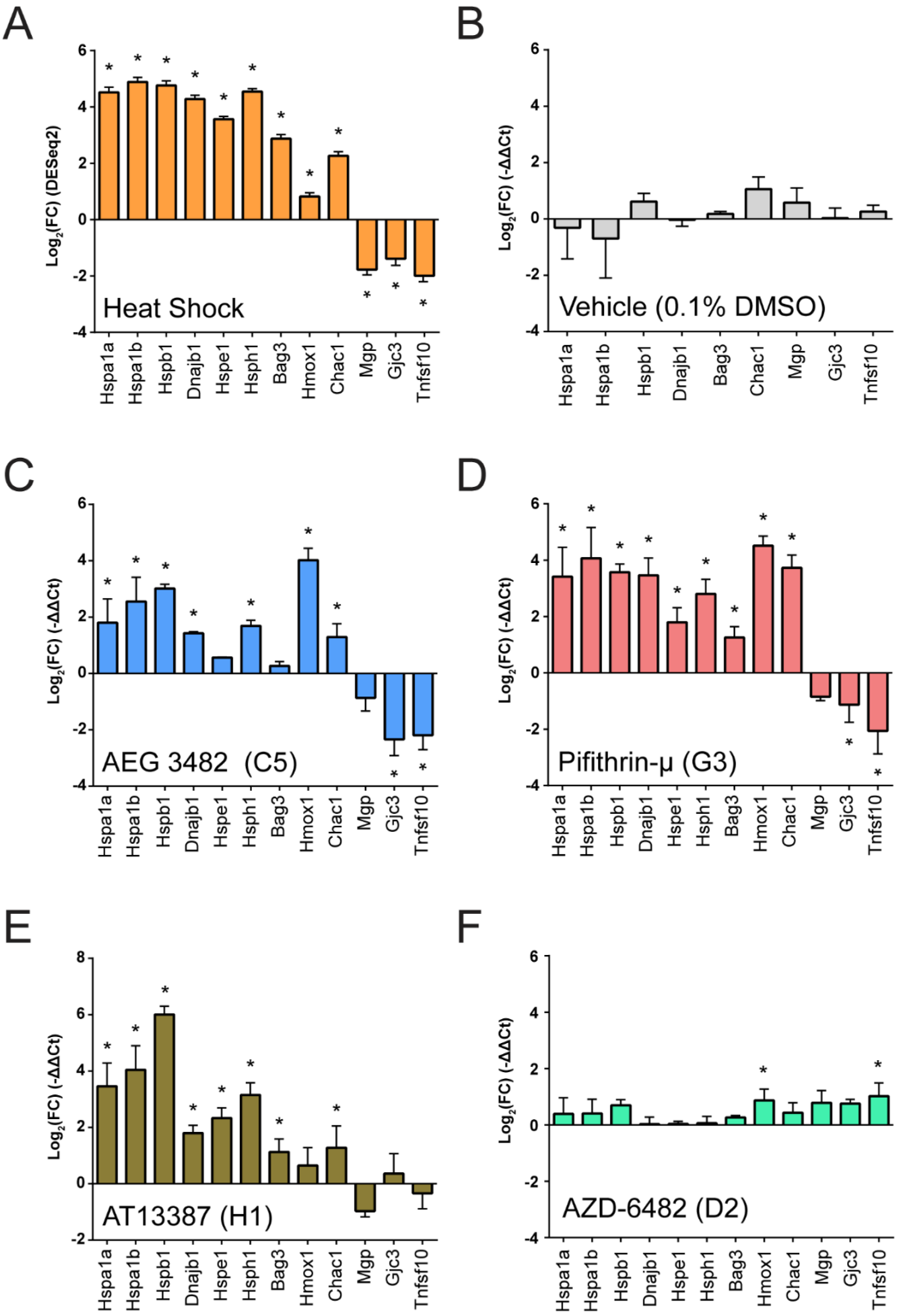
A
Log2(FC) (DESeq2)
Heat Shock
B
Log2(FC) (-ΔΔCt)
Vehicle (0.1% DMSO)
C
Log2(FC) (-ΔΔCt)
AEG 3482 (C5)
D
Log2(FC) (-ΔΔCt)
Pifithrin-μ (G3)
E
Log2(FC) (-ΔΔCt)
AT13387 (H1)
F
Log2(FC) (-ΔΔCt)
AZD-6482 (D2)
Hspa1a
Hspa1b
Hspb1
Dnajb1
Hspe1
Hsph1
Bag3
Hmox1
Chac1
Mgp
Gjc3
Tnfsf10

4.3.7 The perturbagen pifithrin-μ reduces neomycin-induced hair cell death in cultured utricles from adult mice

We next examined whether the three protective perturbagens identified in the zebrafish screen reduce aminoglycoside-induced hair cell death in mouse utricles. AEG 3482 was not protective against neomycin-induced hair cell death in either the peripheral or central regions of the utricle (Fig 4.7 A-B, blue bars). AT13387 alone was toxic to hair cells, reducing survival in the central region but not in the peripheral region (Fig 4.7 A-B, brown bars). AT13387 was not protective in either region. In the absence of neomycin, pifithrin-μ (Fig 4.7 A-B, pink bars) caused a significant reduction in the number of hair cells in both regions compared to vehicle alone; however, pifithrin-μ was also significantly protective against neomycin-induced hair cell death (Fig 4.7 A-B, pink bars). Of the three perturbagen hits that were protective in the zebrafish screen, only pifithrin-μ was protective against neomycin-induced hair cell death, although it also independently caused some damage to hair cells as a single treatment. To assess whether reducing the dose of pifithrin-μ would reduce the toxic effect we observed, we also tested pifithrin-μ at 5 μM, which eliminated both the toxicity and the protective effect of the compound (Fig 4.7 C, D) ($p > 0.99$ for both comparisons). Overall our data indicate that the LINCS tool generated a list of perturbagens that matched the transcriptional profile of protective heat shock. We screened 43 perturbagens in zebrafish, and 3 (~7%) of these were protective. One of these, pifithrin-μ, was also protective in a mammalian inner ear system.

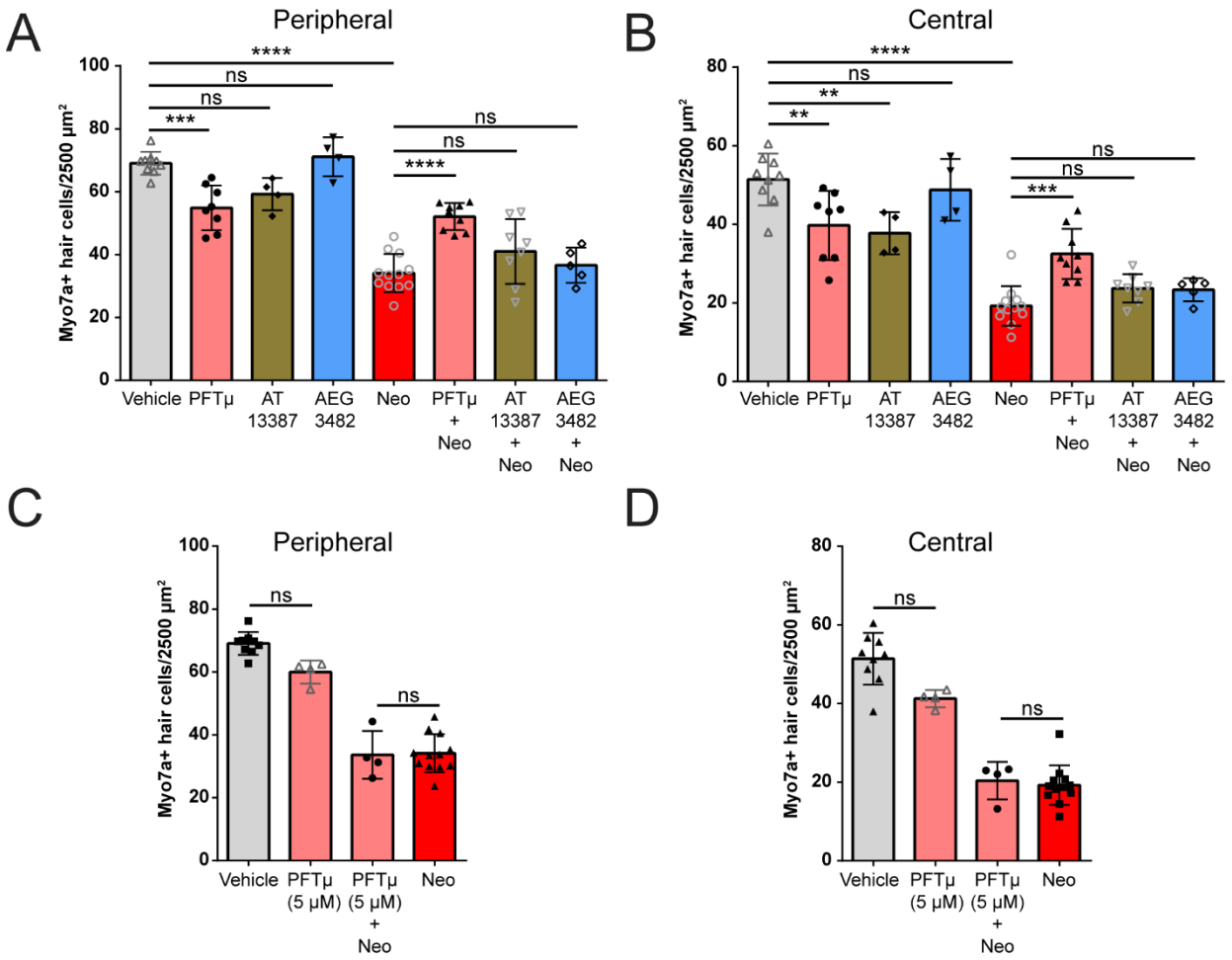

Figure 0.7 Perturbagen hit Pifithrin-µ reduces aminoglycoside-induced hair cell death in cultured mouse utricles. A) Myosin VIIa- and Hoechst 33342-labelled hair cell counts in the peripheral region of utricles treated with vehicle (0.1% DMSO, gray), Pifithrin-µ (10 µM, pink), AT13387 (10 µM, brown), or AEG3482 (25 µM, blue). B) Hair cell counts labelled as in A for the central region of the utricle. Hair cell count results in A-D are pooled from two independent experiments with the significant effects replicated in the second experiment (n=4-12 utricles per group). C-D) Reducing the concentration of pifithrin-µ to 5 µM reduces the toxicity of the compound but also abolishes the protection against neomycin-induced hair cell death in both the peripheral (C) and central (D) regions of the utricle. Vehicle and neomycin conditions in (C) and (D) are repeated from (A) and (B) as 5 µM exposures were performed in the same experiment. Asterisks represent adjusted p-values from Tukey post-hoc test results following one-way ANOVA with *** representing $p < 0.001$, **** representing $p < 0.0001$, and 'ns' (not significant) representing $p > 0.05$. All error bars in A-D represent ± S.D. values.

4.4 Discussion

This study utilized a workflow that began with a previously-identified otoprotective stimulus, heat shock, and ended with a small molecule that could recapitulate both the gene

expression profile and otoprotective effect of heat shock. The LINCS database was used to identify perturbagens that match the transcriptional signature of heat shock, which were then moved through two separate model systems to test effects on inner ear ototoxicity: The zebrafish neuromast and the adult mouse utricle. Pifithrin-μ was identified as a perturbagen that recapitulates both the gene expression profile and protective effect of heat shock.

We can make several observations from this workflow pertaining to the use of LINCS, a bioinformatic tool that allowed us to move from an RNA-Seq gene expression profile into a perturbagen screening assay by matching the heat shock gene expression pattern to a database of gene expression patterns in cell lines exposed to small molecules. Using the results from the LINCS Query alone, only a subset of the genes that were used as inputs are recognized by the L1000 gene expression assay used in the LINCs database. In addition, there is a lack of fold enrichment/depletion information for use in this query, which reduces the complexity of the gene expression pattern into a binary (induced/depleted) comparison. In addition, the LINCS query expression patterns are made against nine core human cancer cell lines, which may respond to perturbagen application very differently from inner ear epithelia. Despite these limitations, the perturbagens returned from LINCS query using the heat shock signature did recapitulate the heat shock gene expression signature in the cultured utricle system. Because only the perturbagens that were hits in the zebrafish screen were carried forward into utricle model, we cannot conclude that every matching perturbagen would match the heat shock signature; however, we can say that AT13387, being an HSP90 inhibitor and external perturbagen, did induce the expected heat shock expression signature. We also tested the expression pattern of cultured utricles exposed to reverse perturbagen AZD-6482, and this exposure resulted in a significantly different gene expression pattern by

qPCR compared to the matching perturbagen pifithrin-μ, suggesting that the LINCS designation of 'matching' versus 'reverse' provides specificity in gene expression patterning despite some limitations of the query tool.

Our LINCS query results include several compounds that have been previously investigated with respect to ototoxicity. The HSP90 inhibitor Alvespimycin (also known as 17-DMAG) has been shown to protect against kanamycin exposure in mouse neonatal cochlear explants and to induce HSP70 localized by immunohistochemistry to inner and outer cochlear hair cells (Liu, Yu et al. 2015). Geldanamycin, another HSP90 inhibitor, was effective in reducing gentamicin-induced hair cell death in organ of Corti explants (Yu, Szczepek et al. 2009). Pifithrin-μ was previously found to be protective against neomycin- and gentamicin-induced damage in zebrafish neuromasts (Coffin, Rubel et al. 2013). The proteasome inhibitors MLN-2238 and MG-132 are related to Z-LLF-CHO, a proteasome inhibitor that protects against gentamicin, neomycin, and cisplatin-induced ototoxicity in zebrafish (Coffin, Williamson et al. 2013). Etoposide and teniposide, both inhibitors of topoisomerase 2, share molecular target activity with amsacrine, an antineoplastic agent with topoisomerase II inhibition activity that is otoprotective against aminoglycoside-induced hair cell death in the zebrafish lateral line (Ou, Cunningham et al. 2009). In the 'non-matching perturbagen' category, the perturbagen Trichostatin A (LINCS query signature 86th percentile), a class I/II HDAC inhibitor, protects early postnatal organ of Corti explants against cisplatin-induced ototoxicity *in vitro* and also induced the expression of several genes related to synaptic plasticity that had been downregulated by cisplatin exposure (Wang, Zhang et al. 2013). Parthenolide (LINCS query signature 95th percentile), an NF-κB inhibitor, increased apoptotic signalling in rat cochlear explants and synthetic peptide

inhibition of NF-κB induced significant hair cell death in these explants (Nagy, Monge et al. 2005). The effects of some reverse perturbagens (and related compounds) have also previously been studied in the inner ear. AZD-6482 (LINCS query bottom 0.01^{th} percentile), a PI3K signalling pathway inhibitor, is related to the activity of the protein PTEN, which also down-regulates PI3K signalling. In a study of rat cochlear explants, inhibition of PI3K using a small molecule inhibitor sensitized hair cells to gentamicin-induced damage (Chung, Pak et al. 2006). With the LINCS query data, we would be able to hypothesize the ototoxic sensitization effect of PI3K inhibition is at least not due to the generation of an HSP-inducing stress response. Furthermore, in mouse cochlear explants, inhibition of PTEN by an inhibitor or by genetic ablation was protective against gentamicin-induced ototoxicity (Jadali and Kwan 2016). These results together suggest a protective role for PI3K signalling in hair cell survival. Sirolimus, another reverse perturbagen has mixed effects, with one study demonstrating protection of hair cells and improved hearing function in rats *in vivo* exposed to cisplatin (Fang and Xiao 2014), and another study showing sirolimus-induced hair cell damage in rat cochlear explants (Leitmeyer, Glutz et al. 2015). It is difficult to compare the results of these two studies directly due to their differences in experimental design, but the overall suggestion is that the activity of rapamycin is involved in determining hair cell survival. The observation that only one of the matching perturbagens was protective and the other two hits from the zebrafish screen were external HSP-inducers implies that the transcriptional profiling used in LINCS may only point to families of protective compounds, but that the specific exposures and dosing schemes will likely need to be optimized for any individual compound. Despite some non-matching and reverse perturbagens not being related to induction of the heat shock response, their signatures within the LINCS query tool

demonstrate that gene expression signatures exist within the LINCS query tool that may be of interest in future inner ear research investigating hair cell function and survival signalling. Overall our data indicate that the LINCS query tool is useful for identifying compounds that can mimic or reverse important cellular processes related to ototoxicity or hearing loss.

Two of the protective perturbagens identified in zebrafish, AEG 3482 and AT13387, did not protect hair cells against neomycin-induced death in the mouse adult utricle. It is important to note that in hair cells from both animals, the duration and timing of perturbagen exposure and the dose and duration of exposure to ototoxin must be considered as factors that may cause individual compounds to elicit a protective effect. In previous studies the heat shock stimulus has been administered as a pre-treatment (Cunningham and Brandon 2006), suggesting that the timing of perturbagen exposure compared to ototoxin application is an additional factor that should be considered. Previous work suggests that zebrafish neuromast hair cells respond to treatment with different aminoglycosides with differential time courses of cell death (Owens, Coffin et al. 2009), allowing for differentiation between 'acute' and 'chronic' types of ototoxicity and otoprotective responses (Coffin, Williamson et al. 2013). We only tested perturbagens against acute aminoglycoside exposure, and it is possible that they may show a positive response under different conditions. Finally, it may be that perturbagens designed to function against mammalian targets may be ineffective against zebrafish while still effective in utricle cultures.

In summary, we used the transcriptional signature of heat shock, which is protective against ototoxic drug-induced hair cell death, to look for small molecules in the LINCS database that mimic the transcriptional signature of heat shock and thus may also be protective in the inner ear. We heat shocked cultured utricle explants from adult mice and

performed RNA-sequencing on them, comparing to control (no heat shock) utricles. We then input selected differentially-expressed genes into the LINCS query tool and selected a subset of small molecule perturbagens that either matched, did not match, or reversed the heat shock signature in the cell lines tested in the LINCS database. We screened these molecules for protection against hair cell death caused by the ototoxic aminoglycoside antibiotic neomycin in zebrafish lateral line neuromasts. From this screen, three molecules were protective against neomycin-induced hair cell death: AEG 3482, Pifithrin-μ, and AT13387. The LINCS-identified matching perturbagen pifithrin-μ reproduced the heat shock gene expression signature in cultured mouse utricles, while the LINCS-identified reverse perturbagen AZD-6482 did not induce the heat shock transcriptional signature in utricles. We tested the perturbagens that were protective in the zebrafish screen to determine if they were protective against neomycin-induced hair cell death in cultured utricles. One of the perturbagens, pifithrin-μ, protected hair cells from neomycin damage in the cultured utricle explant model system. Taken together our data describe a new workflow for utilizing RNA-Seq datasets coupled with the LINCS query tool to identify compounds that mimic (or reverse) a gene expression signature of interest for studies of inner ear damage and protection.

4.5 Experimental contributions

I performed utricle dissections, RNA extractions and quality control, cDNA reverse transcription, Nextera XT library preparation and quality control, differential gene expression analysis, LINCS database queries, zebrafish perturbagen screening, qPCR reactions, and utricle perturbagen testing. Robert Morell and Dani Martin assisted with the RNA-Seq

demultiplexing and alignments as well as preliminary differential gene expression analysis. Erich Boger performed HiSeq sequencing and assisted with Nextera XT library preparation. Patricia Wu assisted with zebrafish perturbagen screening. David Raible provided access to zebrafish for screening and provided guidance with the zebrafish perturbagen screening protocol.

Outlook: Summary and future directions

The goals of this study were to 1) find transcriptional responses to heat shock in hair cells and supporting cells of the inner ear, and 2) to identify otoprotective compounds capable of inducing a response like heat shock in inner ear tissue. To accomplish the first goal, we employed two cell-specific isolation techniques. After validating that both techniques can isolate cell-specific transcriptomes, the results of both lines of experimentation led to the conclusion that both hair cells and supporting cells can initiate a transcriptional heat shock response; however, a notable lack of translational machinery transcripts were noted in hair cells compared to supporting cells, which suggested that hair cells may not mount a translational heat shock response. To accomplish the second goal, we used an open-source database to identify small molecules that act as perturbagens to induce heat shock-like transcriptional patterns in cell lines. The result of this study yielded small molecules capable of preventing ototoxic hair cell death in zebrafish, one of these small molecules was also capable of preventing ototoxic damage in mouse utricle *in vitro*. Furthermore, it was noted that all the zebrafish-identified protective molecules produced gene expression signatures that were highly correlated to the gene expression signature of heat shock. Together these results suggest that the effect of native heat shock response in inner ear tissue can be pharmacologically recapitulated to protect hair cells from ototoxic damage in multiple model

systems, but also suggests that careful selection of time and dose also play a role in the protective effect of the heat shock response. Having addressed the goals of the project, the current study has also generated some interesting hypotheses for future research. From the first goal, a study of HSP27 expression and otoprotective capability could be an interesting avenue of study. Here we have identified HSP27 as highly expressed in supporting cells, therefore there may be an additional HSP that has protective abilities in the inner ear, and again this protection may be non-cell autonomous. Secondly, exploring the translational capacity of hair cells may be another interesting avenue to explore, as we have shown here that hair cells appear to be deficient in some DEGs involved in translation. From the second goal, future studies could use the same pipeline to characterize the transcriptional profiles of novel molecules of interest in the inner ear. In addition, transcriptional alignment tools like the LINCS Query may help identify similar small molecules in the future if there are compounds identified with otoprotective capability that do not have a fully-elucidated mechanism of action.

Appendices

Recognized enriched LINCS query genes				
Ahr	Dennd1c	Hsp90aa1	Mns1	Ptprn
Ahsa1	Diras2	Hsp90ab1	Morc4	Rad51c
Amotl2	Dnaja1	Hspa1a	Mthfd2	Rgs1
Angpt2	Dnajb1	Hspa1l	Myom2	Rhof
Aox1	Dnajb2	Hspa4l	Opn3	Sele
Apobr	Dnajb4	Hspa8	Osbpl3	Serpinh1
Arc	Dusp2	Hspb1	Osmr	Sfn
Arid5a	Dusp4	Hspb8	P4ha1	Sh2d4a
Arid5b	Dusp8	Hspd1	P4ha2	Sh3bp2
Atf3	Edn1	Hspe1	Parm1	Shb
Bag3	Efhd2	Hsph1	Pde3b	Slc12a7
Baiap2	Egr1	Igf2bp2	Pdk4	Slc25a38
Banp	Ehd4	Il33	Pdzd2	Slc6a2
Cacybp	Entpd3	Inpp5j	Pgf	Spsb1
Cd83	F2rl1	Ivl	Phlda2	Stip1
Cdh1	Fam46c	Jun	Plin2	Tgfa
Cdr2	Filip1l	Kcnk5	Pmaip1	Trib3
Chac1	Fkbp4	Krt1	Ppl	Trim15
Chka	Foxn1	Krt6a	Prkab2	Tubgcp4
Chordc1	Gadd45g	Lamc2	Prkar1b	Uspl1
Creb5	Gca	Maff	Procr	Vgll3
Cryab	Gprasp1	Mc4r	Prrg4	Wt1
Cyr61	Gzmm	Mknk2	Ptpn14	Xk
Recognized depleted LINCS query genes				
Angptl2	Clec5a	Hpgds	Mpz	Sox18
Apba2	Col9a1	Il15	Ndp	Tagln3
Aplnr	Evi2a	Kcna1	Plp1	Tnfsf10
C3ar1	Fam105a	Kcnj8	Pou3f1	Top2a
Cd52	Fcgr2b	Meox2	Ptafr	
Cdh19	Fhl3	Mgp	Ramp2	

Appendix Table 6.1 The gene names recognized by the LINCS query tool. The 115 enriched genes recognized are displayed in the top half of the table, and the 28 depleted genes recognized are displayed in the bottom half. Genes are displayed in alphabetical order for both enriched and depleted categories.

Gene Name	Taqman Assay ID
Hspa1b	Mm03038954_s1
Hspa1a	Mm01159846_s1
Hspb1	Mm00834384_g1
Hsph1	Mm00442864_m1
Dnajb1	Mm00444519_m1
Bag3	Mm00443474_m1
Cacybp	Mm01295897_g1
Chac1	Mm00509926_m1
Mgp	Mm00485009_m1
Tnfsf10	Mm01283606_m1
Gjc3	Mm01204089_m1
Hmox1	Mm00516005_m1
Hspe1	Mm00434083_m1
Actb	Mm02619580_g1
Gapdh	Mm99999915_g1

Appendix Table 0.2 Summary table of gene names and Taqman assay product identifiers used for validation by RT-qPCR in utricle of the DEG heat shock signature identified by RNA-Seq (Figure 4.2) and LINCS perturbagen gene expression profiling in utricle (Figure 4.6).

Appendix Table 0.3 Summary table of 42 perturbagens used the zebrafish DASPEI screen. Table contains the name of each perturbagen compound, the vendor and catalogue number of the compound purchased for the screen, and its location on the screening plate used as the stock concentration plate, which was used to determine perturbagen identity after screening.

Perturbagen Name	Vendor (Cat #)	Plate Location
Sirolimus	SelleckChem S1039	A1
BIIB021	SelleckChem S1175	A2
CYT-997	SelleckChem S2195	A3
Anisomycin	SelleckChem S7409	A4
Withaferin-a	Tocris 2816	A5
BCI-hydrochloride	Sigma B4313	A6
Arachidonyl-trifluoro-methyl ketone	Tocris 1462	A7
Trichostatin-A	SelleckChem S1045	B1
Etoposide	SelleckChem S1225	B2
Parthenolide	SelleckChem S2341	B3
Piperlongumine	SelleckChem S7551	B4
CMPD-1	Tocris 2186	B5
Elesclomol	SelleckChem S1052	C1
Ranolazine	SelleckChem S1425	C2
Ursolic-Acid	SelleckChem S2370	C3
SB-225002	SelleckChem S7651	C4
AEG 3482	Tocris 2651	C5
NVP-AUY922	SelleckChem S1069	D1
AZD-6482	SelleckChem S1462	D2
MG-132	SelleckChem S2619	D3
Xanthohumol	SelleckChem S7889	D4
BNTX maleate	Tocris 0899	D5
Tanespimycin	SelleckChem S1141	E1
Disulfiram	SelleckChem S1680	E2
Fostamatinib	SelleckChem S2625	E3
Butein	SelleckChem S8036	E4
Manumycin-A	Sigma 444170-M	E5
Alvespimycin	SelleckChem S1142	F1
Teniposide	SelleckChem S1787	F2
Geldanamycin	SelleckChem S2713	F3
PU-H71	SelleckChem S8039	F4
Phenethyl-isothiocyanate	Sigma 253731	F5
STA-9090	SelleckChem S1159	G1
Menadione	SelleckChem S1949	G2
Pifithrin-mu	SelleckChem S2930	G3
NSC 632839	Tocris 2647	G4
MLN-4924	EmdMillipore 5.05477.0001	G5
AT-13387	SelleckChem S1163	H1
MLN-2238	SelleckChem S2180	H2
PP-1	SelleckChem S7060	H3
SA-792709	Tocris 2020	H4
Sappanone a dimethyl ether	MicroSource 201136	H5

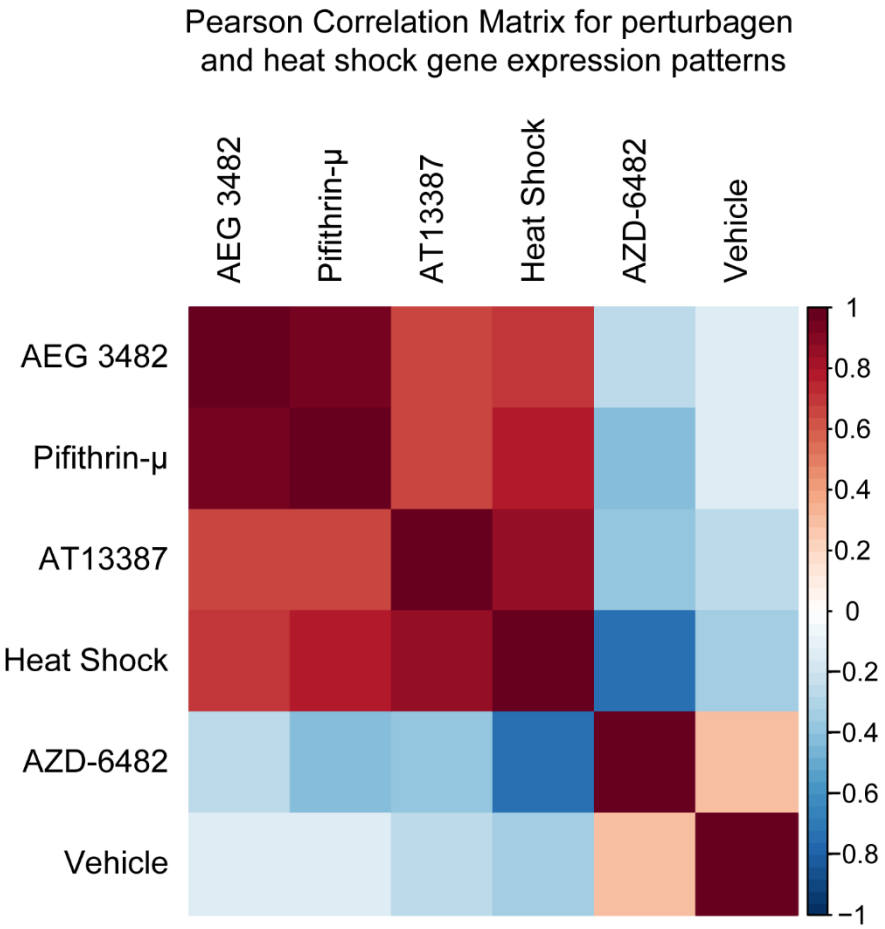

Appendix Figure 0.1 A Pearson correlation heatmap matrix of gene expression changes in heat shock signature genes in cultured utricles following exposure to either heat shock, AEG3482, Pifithrin-μ, AT13387, AZD-6482, or DMSO vehicle. The color shading within the heatmap corresponds to the degree of correlation. Red indicates a positive correlation coefficient between two treatments; white signifies a lack of correlation, and blue signifies a negative correlation coefficient.

Bibliography

Abrashkin, K. A., M. Izumikawa, T. Miyazawa, C.-H. Wang, M. A. Crumling, D. L. Swiderski, L. A. Beyer, T.-W. L. Gong and Y. Raphael (2006). "The fate of outer hair cells after acoustic or ototoxic insults." Hearing Research **218**(1): 20-29.

Al-Malky, G., S. J. Dawson, T. Sirimanna, E. Bagkeris and R. Suri (2015). "High-frequency audiometry reveals high prevalence of aminoglycoside ototoxicity in children with cystic fibrosis." J Cyst Fibros **14**(2): 248-254.

Alam, S. A., K. Ikeda, T. Oshima, M. Suzuki, T. Kawase, T. Kikuchi and T. Takasaka (2000). "Cisplatin-induced apoptotic cell death in Mongolian gerbil cochlea." Hear Res **141**(1-2): 28-38.

Ananthan, J., A. L. Goldberg and R. Voellmy (1986). "Abnormal proteins serve as eukaryotic stress signals and trigger the activation of heat shock genes." Science **232**(4749): 522-524.

Anniko, M. and R. Wroblewski (1986). "Ionic environment of cochlear hair cells." Hear Res **22**: 279-293.

Anttonen, T., I. Belevich, A. Kirjavainen, M. Laos, C. Brakebusch, E. Jokitalo and U. Pirvola (2014). "How to bury the dead: elimination of apoptotic hair cells from the hearing organ of the mouse." J Assoc Res Otolaryngol **15**(6): 975-992.

Avissar, Y., J. H. Choi, C. Rye, J. DeSaix, O. College, V. Jurukovski, R. University and R. R. Wise (2013). Biology, OpenStax College, Rice University.

Baker, T. G., S. Roy, C. S. Brandon, I. K. Kramarenko, S. P. Francis, M. Taleb, K. M. Marshall, R. Schwendener, F. S. Lee and L. L. Cunningham (2015). "Heat shock protein-mediated protection against Cisplatin-induced hair cell death." J Assoc Res Otolaryngol **16**(1): 67-80.

Banfi, B., B. Malgrange, J. Knisz, K. Steger, M. Dubois-Dauphin and K. H. Krause (2004). "NOX3, a superoxide-generating NADPH oxidase of the inner ear." J Biol Chem **279**(44): 46065-46072.

Beere, H. M., B. B. Wolf, K. Cain, D. D. Mosser, A. Mahboubi, T. Kuwana, P. Tailor, R. I. Morimoto, G. M. Cohen and D. R. Green (2000). "Heat-shock protein 70 inhibits apoptosis by preventing recruitment of procaspase-9 to the Apaf-1 apoptosome." Nat Cell Biol **2**(8): 469-475.

Benkafadar, N., J. Menardo, J. Bourien, R. Nouvian, F. Francois, D. Decaudin, D. Maiorano, J. L. Puel and J. Wang (2017). "Reversible p53 inhibition prevents cisplatin ototoxicity without blocking chemotherapeutic efficacy." EMBO Mol Med **9**(1): 7-26.

Berglund, A. M. and D. K. Ryugo (1987). "Hair cell innervation by spiral ganglion neurons in the mouse." J Comp Neurol **255**(4): 560-570.

Betts, J. G., P. Desaix, J. E. Johnson, O. Korol, D. Kruse, B. Poe, J. Wise, M. D. Womble and K. A. Young (2013). Anatomy & Physiology, OpenStax College, Rice University.

Bird, J. E., N. Daudet, M. E. Warchol and J. E. Gale (2010). "Supporting cells eliminate dying sensory hair cells to maintain epithelial integrity in the avian inner ear." J Neurosci **30**(37): 12545-12556.

Boulikas, T. and M. Vougiouka (2004). "Recent clinical trials using cisplatin, carboplatin and their combination chemotherapy drugs (review)." Oncol Rep **11**(3): 559-595.

Brandon, C. S., C. Voelkel-Johnson, L. A. May and L. L. Cunningham (2012). "Dissection of adult mouse utricle and adenovirus-mediated supporting-cell infection." J Vis Exp(61).

Breglio, A. M., A. E. Rusheen, E. D. Shide, K. A. Fernandez, K. K. Spielbauer, K. M. McLachlin, M. D. Hall, L. Amable and L. L. Cunningham (2017). "Cisplatin is retained in the cochlea indefinitely following chemotherapy." Nat Commun **8**(1): 1654.

Brock, P. R., R. Maibach, M. Childs, K. Rajput, D. Roebuck, M. J. Sullivan, V. Laithier, M. Ronghe, P. Dall'Igna, E. Hiyama, B. Brichard, J. Skeen, M. E. Mateos, M. Capra, A. A. Rangaswami, M. Ansari, C. Rechnitzer, G. J. Veal, A. Covezzoli, L. Brugieres, G. Perilongo, P. Czauderna, B. Morland and E. A. Neuwelt (2018). "Sodium Thiosulfate for Protection from Cisplatin-Induced Hearing Loss." N Engl J Med **378**(25): 2376-2385.

Brum, A. M., J. van de Peppel, C. S. van der Leije, M. Schreuders-Koedam, M. Eijken, B. C. van der Eerden and J. P. van Leeuwen (2015). "Connectivity Map-based discovery of parbendazole reveals targetable human osteogenic pathway." Proc Natl Acad Sci U S A **112**(41): 12711-12716.

Bucks, S. A., B. C. Cox, B. A. Vlosich, J. P. Manning, T. B. Nguyen and J. S. Stone (2017). "Supporting cells remove and replace sensory receptor hair cells in a balance organ of adult mice." eLife **6**: e18128.

Burns, J. C., M. C. Kelly, M. Hoa, R. J. Morell and M. W. Kelley (2015). "Single-cell RNA-Seq resolves cellular complexity in sensory organs from the neonatal inner ear." Nat Commun **6**: 8557.

Burns, J. C. and J. S. Stone (2017). "Development and regeneration of vestibular hair cells in mammals." Semin Cell Dev Biol **65**: 96-105.

Cai, T., H. I. Jen, H. Kang, T. J. Klisch, H. Y. Zoghbi and A. K. Groves (2015). "Characterization of the transcriptome of nascent hair cells and identification of direct targets of the Atoh1 transcription factor." J Neurosci **35**(14): 5870-5883.

Cederroth, C. R. (2012). "Loss of aminoglycoside sensitivity in HEI-OC1 cells?" Hear Res **292**(1-2): 83-85; author response pg 86.

Chen, F. Q., K. Hill, Y. J. Guan, J. Schacht and S. H. Sha (2012). "Activation of apoptotic pathways in the absence of cell death in an inner-ear immortomouse cell line." Hear Res **284**(1-2): 33-41.

Chen, P., F. Zindy, C. Abdala, F. Liu, X. Li, M. F. Roussel and N. Segil (2003). "Progressive hearing loss in mice lacking the cyclin-dependent kinase inhibitor Ink4d." Nat Cell Biol **5**(5): 422-426.
Choung, Y. H., A. Taura, K. Pak, S. J. Choi, M. Masuda and A. F. Ryan (2009). "Generation of highly-reactive oxygen species is closely related to hair cell damage in rat organ of Corti treated with gentamicin." Neuroscience **161**(1): 214-226.
Chowdhury, S., K. N. Owens, R. J. Herr, Q. Jiang, X. Chen, G. Johnson, V. E. Groppi, D. W. Raible, E. W. Rubel and J. A. Simon (2018). "Phenotypic Optimization of Urea-Thiophene Carboxamides To Yield Potent, Well Tolerated, and Orally Active Protective Agents against Aminoglycoside-Induced Hearing Loss." J Med Chem **61**(1): 84-97.
Chung, W. H., K. Pak, B. Lin, N. Webster and A. F. Ryan (2006). "A PI3K pathway mediates hair cell survival and opposes gentamicin toxicity in neonatal rat organ of Corti." J Assoc Res Otolaryngol **7**(4): 373-382.
Ciarimboli, G., D. Deuster, A. Knief, M. Sperling, M. Holtkamp, B. Edemir, H. Pavenstadt, C. Lanvers-Kaminsky, A. am Zehnhoff-Dinnesen, A. H. Schinkel, H. Koepsell, H. Jurgens and E. Schlatter (2010). "Organic cation transporter 2 mediates cisplatin-induced oto- and nephrotoxicity and is a target for protective interventions." Am J Pathol **176**(3): 1169-1180.
Coffin, A. B., E. W. Rubel and D. W. Raible (2013). "Bax, Bcl2, and p53 differentially regulate neomycin- and gentamicin-induced hair cell death in the zebrafish lateral line." J Assoc Res Otolaryngol **14**(5): 645-659.
Coffin, A. B., K. L. Williamson, A. Mamiya, D. W. Raible and E. W. Rubel (2013). "Profiling drug-induced cell death pathways in the zebrafish lateral line." Apoptosis **18**(4): 393-408.
Corey, D. P. and A. J. Hudspeth (1979). "Ionic basis of the receptor potential in a vertebrate hair cell." Nature **281**(5733): 675-677.
Cunningham, L. L. (2006). "The adult mouse utricle as an in vitro preparation for studies of ototoxic-drug-induced sensory hair cell death." Brain Res **1091**(1): 277-281.
Cunningham, L. L. and C. S. Brandon (2006). "Heat shock inhibits both aminoglycoside- and cisplatin-induced sensory hair cell death." J Assoc Res Otolaryngol **7**(3): 299-307.
Cunningham, L. L., A. G. Cheng and E. W. Rubel (2002). "Caspase activation in hair cells of the mouse utricle exposed to neomycin." J Neurosci **22**(19): 8532-8540.
Cunningham, L. L., J. I. Matsui, M. E. Warchol and E. W. Rubel (2004). "Overexpression of Bcl-2 prevents neomycin-induced hair cell death and caspase-9 activation in the adult mouse utricle in vitro." J Neurobiol **60**(1): 89-100.
Dalet, A., J. Bonsacquet, S. Gaboyard-Niay, I. Calin-Jageman, R. L. Chidavaenzi, S. Venteo, G. Desmadryl, J. M. Goldberg, A. Lysakowski and C. Chabbert (2012). "Glutamate Transporters EAAT4 and EAAT5 Are Expressed in Vestibular Hair Cells and Calyx Endings." PLoS ONE **7**(9): e46261.
Dallos, P. (1992). "The active cochlea." J Neurosci **12**(12): 4575-4585.
Dallos, P. and R. R. Fay (2012). The cochlea, Springer Science & Business Media.
Daugaard, M., M. Rohde and M. Jaattela (2007). "The heat shock protein 70 family: Highly homologous proteins with overlapping and distinct functions." FEBS Lett **581**(19): 3702-3710.
De Gendt, K., G. Verhoeven, P. S. Amieux and M. F. Wilkinson (2014). "Research Resource: Genome-Wide Identification of AR-Regulated Genes Translated in Sertoli Cells In Vivo Using the RiboTag Approach." Molecular Endocrinology **28**(4): 575-591.
DeLuca, D. S., J. Z. Levin, A. Sivachenko, T. Fennell, M. D. Nazaire, C. Williams, M. Reich, W. Winckler and G. Getz (2012). "RNA-SeQC: RNA-seq metrics for quality control and process optimization." Bioinformatics **28**(11): 1530-1532.
Dobin, A., C. A. Davis, F. Schlesinger, J. Drenkow, C. Zaleski, S. Jha, P. Batut, M. Chaisson and T. R. Gingeras (2013). "STAR: ultrafast universal RNA-seq aligner." Bioinformatics **29**(1): 15-21.
Duan, Q., C. Flynn, M. Niepel, M. Hafner, J. L. Muhlich, N. F. Fernandez, A. D. Rouillard, C. M. Tan, E. Y. Chen, T. R. Golub, P. K. Sorger, A. Subramanian and A. Ma'ayan (2014). "LINCS Canvas

Browser: interactive web app to query, browse and interrogate LINCS L1000 gene expression signatures." Nucleic Acids Res **42**(Web Server issue): W449-460.
Eshraghi, A. A., J. Wang, E. Adil, J. He, A. Zine, M. Bublik, C. Bonny, J. L. Puel, T. J. Balkany and T. R. Van De Water (2007). "Blocking c-Jun-N-terminal kinase signaling can prevent hearing loss induced by both electrode insertion trauma and neomycin ototoxicity." Hear Res **226**(1-2): 168-177.
Fang, B. and H. Xiao (2014). "Rapamycin alleviates cisplatin-induced ototoxicity in vivo." Biochem Biophys Res Commun **448**(4): 443-447.
Fausti, S. A., J. A. Henry, W. J. Helt, D. S. Phillips, R. H. Frey, D. Noffsinger, V. D. Larson and C. G. Fowler (1999). "An individualized, sensitive frequency range for early detection of ototoxicity." Ear Hear **20**(6): 497-505.
Fettiplace, R. and K. X. Kim (2014). "The physiology of mechanoelectrical transduction channels in hearing." Physiol Rev **94**(3): 951-986.
Flock, A. and H. C. Cheung (1977). "Actin filaments in sensory hairs of inner ear receptor cells." J Cell Biol **75**(2 Pt 1): 339-343.
Forge, A. (1985). "Outer hair cell loss and supporting cell expansion following chronic gentamicin treatment." Hearing Research **19**(2): 171-182.
Forge, A. and L. Li (2000). "Apoptotic death of hair cells in mammalian vestibular sensory epithelia." Hear Res **139**(1-2): 97-115.
Forge, A., L. Li and G. Nevill (1998). "Hair cell recovery in the vestibular sensory epithelia of mature guinea pigs." J Comp Neurol **397**(1): 69-88.
Forge, A. and J. Schacht (2000). "Aminoglycoside antibiotics." Audiol Neurootol **5**(1): 3-22.
Forge, A., A. Wright and S. J. Davies (1987). "Analysis of structural changes in the stria vascularis following chronic gentamicin treatment." Hear Res **31**(3): 253-265.
Francis, S. P. and L. L. Cunningham (2017). "Non-autonomous Cellular Responses to Ototoxic Drug-Induced Stress and Death." Frontiers in Cellular Neuroscience **11**(252).
Francis, S. P., J. Katz, K. D. Fanning, K. A. Harris, B. D. Nicholas, M. Lacy, J. Pagana, P. F. Agris and J. B. Shin (2013). "A novel role of cytosolic protein synthesis inhibition in aminoglycoside ototoxicity." J Neurosci **33**(7): 3079-3093.
Francis, S. P., Kramarenko, II, C. S. Brandon, F. S. Lee, T. G. Baker and L. L. Cunningham (2011). "Celastrol inhibits aminoglycoside-induced ototoxicity via heat shock protein 32." Cell Death Dis **2**: e195.
Freyer, D. R., L. Chen, M. D. Krailo, K. Knight, D. Villaluna, B. Bliss, B. H. Pollock, J. Ramdas, B. Lange, D. Van Hoff, M. L. VanSoelen, J. Wiernikowski, E. A. Neuwelt and L. Sung (2017). "Effects of sodium thiosulfate versus observation on development of cisplatin-induced hearing loss in children with cancer (ACCL0431): a multicentre, randomised, controlled, open-label, phase 3 trial." Lancet Oncol **18**(1): 63-74.
Furness, D. N. and K. P. Lehre (1997). "Immunocytochemical localization of a high-affinity glutamate-aspartate transporter, GLAST, in the rat and guinea-pig cochlea." Eur J Neurosci **9**(9): 1961-1969.
Gabai, V. L., A. B. Meriin, D. D. Mosser, A. W. Caron, S. Rits, V. I. Shifrin and M. Y. Sherman (1997). "Hsp70 prevents activation of stress kinases. A novel pathway of cellular thermotolerance." J Biol Chem **272**(29): 18033-18037.
Garrido, C., S. Gurbuxani, L. Ravagnan and G. Kroemer (2001). "Heat shock proteins: endogenous modulators of apoptotic cell death." Biochem Biophys Res Commun **286**(3): 433-442.
Gillespie, P. G. and U. Muller (2009). "Mechanotransduction by hair cells: models, molecules, and mechanisms." Cell **139**(1): 33-44.
Gillespie, P. G. and R. G. Walker (2001). "Molecular basis of mechanosensory transduction." Nature **413**(6852): 194-202.

Glowatzki, E., N. Cheng, H. Hiel, E. Yi, K. Tanaka, G. C. Ellis-Davies, J. D. Rothstein and D. E. Bergles (2006). "The glutamate-aspartate transporter GLAST mediates glutamate uptake at inner hair cell afferent synapses in the mammalian cochlea." J Neurosci **26**(29): 7659-7664.
Glowatzki, E. and P. A. Fuchs (2002). "Transmitter release at the hair cell ribbon synapse." Nat Neurosci **5**(2): 147-154.
Gomez-Ruiz, S., D. Maksimovic-Ivanic, S. Mijatovic and G. N. Kaluderovic (2012). "On the discovery, biological effects, and use of Cisplatin and metallocenes in anticancer chemotherapy." Bioinorg Chem Appl **2012**: 140284.
Grunberg, S. M., S. Sonka, L. L. Stevenson and F. M. Muggia (1989). "Progressive paresthesias after cessation of therapy with very high-dose cisplatin." Cancer Chemother Pharmacol **25**(1): 62-64.
Guthrie, O. W. (2008). "Aminoglycoside induced ototoxicity." Toxicology **249**(2-3): 91-96.
Harris, J. A., A. G. Cheng, L. L. Cunningham, G. MacDonald, D. W. Raible and E. W. Rubel (2003). "Neomycin-induced hair cell death and rapid regeneration in the lateral line of zebrafish (Danio rerio)." J Assoc Res Otolaryngol **4**(2): 219-234.
Hartl, F. U., A. Bracher and M. Hayer-Hartl (2011). "Molecular chaperones in protein folding and proteostasis." Nature **475**(7356): 324-332.
Hashino, E. and M. Shero (1995). "Endocytosis of aminoglycoside antibiotics in sensory hair cells." Brain Res **704**(1): 135-140.
Hertzano, R., C. Puligilla, S. L. Chan, C. Timothy, D. A. Depireux, Z. Ahmed, J. Wolf, D. J. Eisenman, T. B. Friedman, S. Riazuddin, M. W. Kelley and S. E. Strome (2010). "CD44 is a marker for the outer pillar cells in the early postnatal mouse inner ear." J Assoc Res Otolaryngol **11**(3): 407-418.
Hickox, A. E., A. C. Wong, K. Pak, C. Strojny, M. Ramirez, J. R. Yates, 3rd, A. F. Ryan and J. N. Savas (2017). "Global Analysis of Protein Expression of Inner Ear Hair Cells." J Neurosci **37**(5): 1320-1339.
Hicks, S. C., F. W. Townes, M. Teng and R. A. Irizarry (2017). "Missing data and technical variability in single-cell RNA-sequencing experiments." Biostatistics.
Hinshaw, H. C., W. H. Feldman and K. H. Pfuetze (1946). "Streptomycin in treatment of clinical tuberculosis." Am Rev Tuberc **54**(3): 191-203.
Hirose, K., D. M. Hockenbery and E. W. Rubel (1997). "Reactive oxygen species in chick hair cells after gentamicin exposure in vitro." Hear Res **104**(1-2): 1-14.
Hirose, K., M. A. Rutherford and M. E. Warchol (2017). "Two cell populations participate in clearance of damaged hair cells from the sensory epithelia of the inner ear." Hearing Research **352**: 70-81.
Houghton, J. L., K. D. Green, W. Chen and S. Garneau-Tsodikova (2010). "The future of aminoglycosides: the end or renaissance?" Chembiochem **11**(7): 880-902.
Hudspeth, A. J. (1997). "How hearing happens." Neuron **19**(5): 947-950.
Jadali, A. and K. Y. Kwan (2016). "Activation of PI3K signaling prevents aminoglycoside-induced hair cell death in the murine cochlea." Biol Open **5**(6): 698-708.
Jana, S. and J. K. Deb (2006). "Molecular understanding of aminoglycoside action and resistance." Appl Microbiol Biotechnol **70**(2): 140-150.
Jee, H. (2016). "Size dependent classification of heat shock proteins: a mini-review." J Exerc Rehabil **12**(4): 255-259.
Jiang, H., S. H. Sha, A. Forge and J. Schacht (2006). "Caspase-independent pathways of hair cell death induced by kanamycin in vivo." Cell Death Differ **13**(1): 20-30.
Jiang, M., T. Karasawa and P. S. Steyger (2017). "Aminoglycoside-Induced Cochleotoxicity: A Review." Front Cell Neurosci **11**: 308.
Jin, Z. H., T. Kikuchi, K. Tanaka and T. Kobayashi (2003). "Expression of glutamate transporter GLAST in the developing mouse cochlea." Tohoku J Exp Med **200**(3): 137-144.
Kachar, B., M. Parakkal, M. Kurc, Y. Zhao and P. G. Gillespie (2000). "High-resolution structure of hair-cell tip links." Proc Natl Acad Sci U S A **97**(24): 13336-13341.

Kaimal, V., E. E. Bardes, S. C. Tabar, A. G. Jegga and B. J. Aronow (2010). "ToppCluster: a multiple gene list feature analyzer for comparative enrichment clustering and network-based dissection of biological systems." Nucleic Acids Res **38**(Web Server issue): W96-102.
Kalesnykas, G., M. Niittykoski, J. Rantala, R. Miettinen, A. Salminen, K. Kaarniranta and H. Uusitalo (2007). "The expression of heat shock protein 27 in retinal ganglion and glial cells in a rat glaucoma model." Neuroscience **150**(3): 692-704.
Kalinec, G., P. Thein, C. Park and F. Kalinec (2016). "HEI-OC1 cells as a model for investigating drug cytotoxicity." Hear Res **335**: 105-117.
Kalinec, G. M., P. Webster, D. J. Lim and F. Kalinec (2003). "A cochlear cell line as an in vitro system for drug ototoxicity screening." Audiol Neurootol **8**(4): 177-189.
Karasawa, T. and P. S. Steyger (2015). "An integrated view of cisplatin-induced nephrotoxicity and ototoxicity." Toxicol Lett **237**(3): 219-227.
Kaur, T., K. Hirose, E. W. Rubel and M. E. Warchol (2015). "Macrophage recruitment and epithelial repair following hair cell injury in the mouse utricle." Frontiers in Cellular Neuroscience **9**(150).
Kawashima, Y., G. S. Geleoc, K. Kurima, V. Labay, A. Lelli, Y. Asai, T. Makishima, D. K. Wu, C. C. Della Santina, J. R. Holt and A. J. Griffith (2011). "Mechanotransduction in mouse inner ear hair cells requires transmembrane channel-like genes." J Clin Invest **121**(12): 4796-4809.
Kazmierczak, P., H. Sakaguchi, J. Tokita, E. M. Wilson-Kubalek, R. A. Milligan, U. Muller and B. Kachar (2007). "Cadherin 23 and protocadherin 15 interact to form tip-link filaments in sensory hair cells." Nature **449**(7158): 87-91.
Kenyon, E. J., N. K. Kirkwood, S. R. Kitcher, M. O'Reilly, M. Derudas, D. M. Cantillon, R. J. Goodyear, A. Secker, S. Baxendale, J. C. Bull, S. J. Waddell, T. T. Whitfield, S. E. Ward, C. J. Kros and G. P. Richardson (2017). "Identification of ion-channel modulators that protect against aminoglycoside-induced hair cell death." JCI Insight **2**(24).
Kesser, B. W., G. T. Hashisaki, K. Fletcher, H. Eppard and J. R. Holt (2007). "An in vitro model system to study gene therapy in the human inner ear." Gene Ther **14**(15): 1121-1131.
Khan, S. and R. Chang (2013). "Anatomy of the vestibular system: a review." NeuroRehabilitation **32**(3): 437-443.
Kobayashi, H., N. Ohashi, Y. Watanabe and K. Mizukoshi (1987). "Clinical features of cisplatin vestibulotoxicity and hearing loss." ORL J Otorhinolaryngol Relat Spec **49**(2): 67-72.
Krey, J. F., M. Drummond, S. Foster, E. Porsov, S. Vijayakumar, D. Choi, K. Friderici, S. M. Jones, A. L. Nuttall and P. G. Barr-Gillespie (2016). "Annexin A5 is the Most Abundant Membrane-Associated Protein in Stereocilia but is Dispensable for Hair-Bundle Development and Function." Sci Rep **6**: 27221.
Krueger-Naug, A. M., J. G. Emsley, T. L. Myers, R. W. Currie and D. B. Clarke (2002). "Injury to retinal ganglion cells induces expression of the small heat shock protein Hsp27 in the rat visual system." Neuroscience **110**(4): 653-665.
Kwan, K. Y., J. Shen and D. P. Corey (2015). "C-MYC transcriptionally amplifies SOX2 target genes to regulate self-renewal in multipotent otic progenitor cells." Stem Cell Reports **4**(1): 47-60.
Lamb, J., E. D. Crawford, D. Peck, J. W. Modell, I. C. Blat, M. J. Wrobel, J. Lerner, J. P. Brunet, A. Subramanian, K. N. Ross, M. Reich, H. Hieronymus, G. Wei, S. A. Armstrong, S. J. Haggarty, P. A. Clemons, R. Wei, S. A. Carr, E. S. Lander and T. R. Golub (2006). "The Connectivity Map: using gene-expression signatures to connect small molecules, genes, and disease." Science **313**(5795): 1929-1935.
Lanford, P. J., Y. Lan, R. Jiang, C. Lindsell, G. Weinmaster, T. Gridley and M. W. Kelley (1999). "Notch signalling pathway mediates hair cell development in mammalian cochlea." Nat Genet **21**(3): 289-292.
Law, C. W., Y. Chen, W. Shi and G. K. Smyth (2014). "voom: precision weights unlock linear model analysis tools for RNA-seq read counts." Genome Biology **15**(2): R29.
Leitmeyer, K., A. Glutz, V. Radojevic, C. Setz, N. Huerzeler, H. Bumann, D. Bodmer and Y. Brand (2015). "Inhibition of mTOR by Rapamycin Results in Auditory Hair Cell Damage and

Decreased Spiral Ganglion Neuron Outgrowth and Neurite Formation In Vitro." Biomed Res Int **2015**: 925890.
LeMasurier, M. and P. G. Gillespie (2005). "Hair-cell mechanotransduction and cochlear amplification." Neuron **48**(3): 403-415.
Lerner, S. A., B. A. Schmitt, R. Seligsohn and G. J. Matz (1986). "Comparative study of ototoxicity and nephrotoxicity in patients randomly assigned to treatment with amikacin or gentamicin." Am J Med **80**(6b): 98-104.
Lesniak, W., V. L. Pecoraro and J. Schacht (2005). "Ternary complexes of gentamicin with iron and lipid catalyze formation of reactive oxygen species." Chem Res Toxicol **18**(2): 357-364.
Li, B. and C. N. Dewey (2011). "RSEM: accurate transcript quantification from RNA-Seq data with or without a reference genome." BMC Bioinformatics **12**(1): 323.
Li, C. Y., J. S. Lee, Y. G. Ko, J. I. Kim and J. S. Seo (2000). "Heat shock protein 70 inhibits apoptosis downstream of cytochrome c release and upstream of caspase-3 activation." J Biol Chem **275**(33): 25665-25671.
Li, H. and P. S. Steyger (2011). "Systemic aminoglycosides are trafficked via endolymph into cochlear hair cells." Sci Rep **1**: 159.
Li, Y., S. Roth, M. Laser, J. X. Ma and C. E. Crosson (2003). "Retinal preconditioning and the induction of heat-shock protein 27." Invest Ophthalmol Vis Sci **44**(3): 1299-1304.
Liang, F., B. A. Schulte, C. Qu, W. Hu and Z. Shen (2005). "Inhibition of the calcium- and voltage-dependent big conductance potassium channel ameliorates cisplatin-induced apoptosis in spiral ligament fibrocytes of the cochlea." Neuroscience **135**(1): 263-271.
Lin, V., J. S. Golub, T. B. Nguyen, C. R. Hume, E. C. Oesterle and J. S. Stone (2011). "Inhibition of Notch activity promotes nonmitotic regeneration of hair cells in the adult mouse utricles." J Neurosci **31**(43): 15329-15339.
Liu, J., J. Lee, M. A. Salazar Hernandez, R. Mazitschek and U. Ozcan (2015). "Treatment of obesity with celastrol." Cell **161**(5): 999-1011.
Liu, Y., Y. Yu, H. Chu, D. Bing, S. Wang, L. Zhou, J. Chen, Q. Chen, C. Pan, Y. Sun and Y. Cui (2015). "17-DMAG induces Hsp70 and protects the auditory hair cells from kanamycin ototoxicity in vitro." Neurosci Lett **588**: 72-77.
Liu, Z., J. A. Dearman, B. C. Cox, B. J. Walters, L. Zhang, O. Ayrault, F. Zindy, L. Gan, M. F. Roussel and J. Zuo (2012). "Age-dependent in vivo conversion of mouse cochlear pillar and Deiters' cells to immature hair cells by Atoh1 ectopic expression." J Neurosci **32**(19): 6600-6610.
Lo, W. C., C. T. Wu, H. C. Lee, Y. H. Young, Y. L. Chang and P. W. Cheng (2017). "Evaluation of geranylgeranylacetone against cisplatin-induced ototoxicity by auditory brainstem response, heat shock proteins and oxidative levels in guinea pigs." Neurotoxicol Teratol **61**: 29-35.
Love, M. I., W. Huber and S. Anders (2014). "Moderated estimation of fold change and dispersion for RNA-seq data with DESeq2." Genome Biology **15**(12): 550.
Lowenheim, H., D. N. Furness, J. Kil, C. Zinn, K. Gultig, M. L. Fero, D. Frost, A. W. Gummer, J. M. Roberts, E. W. Rubel, C. M. Hackney and H. P. Zenner (1999). "Gene disruption of p27(Kip1) allows cell proliferation in the postnatal and adult organ of corti." Proc Natl Acad Sci U S A **96**(7): 4084-4088.
Lundberg, Y. W., Y. Xu, K. D. Thiessen and K. L. Kramer (2015). "Mechanisms of otoconia and otolith development." Dev Dyn **244**(3): 239-253.
Lysakowski, A. and J. M. Goldberg (2004). Morphophysiology of the Vestibular Periphery. The Vestibular System. S. M. Highstein, R. R. Fay and A. N. Popper. New York, NY, Springer New York**:** 57-152.
Marcotti, W., S. M. van Netten and C. J. Kros (2005). "The aminoglycoside antibiotic dihydrostreptomycin rapidly enters mouse outer hair cells through the mechano-electrical transducer channels." J Physiol **567**(Pt 2): 505-521.
Marini, F. (2018). "'pcaExplorer: Interactive Visualization of RNA-seqData Using a Principal Components Approach'." R package version 2.6.0.

Matern, M., S. Vijayakumar, Z. Margulies, B. Milon, Y. Song, R. Elkon, X. Zhang, S. M. Jones and R. Hertzano (2017). "Gfi1(Cre) mice have early onset progressive hearing loss and induce recombination in numerous inner ear non-hair cells." Sci Rep **7**: 42079.

Matern, M. S., A. Beirl, Y. Ogawa, Y. Song, N. Paladugu, K. S. Kindt and R. Hertzano (2018). "Transcriptomic Profiling of Zebrafish Hair Cells Using RiboTag." Frontiers in Cell and Developmental Biology **6**(47).

May, L. A., Kramarenko, II, C. S. Brandon, C. Voelkel-Johnson, S. Roy, K. Truong, S. P. Francis, E. L. Monzack, F. S. Lee and L. L. Cunningham (2013). "Inner ear supporting cells protect hair cells by secreting HSP70." J Clin Invest **123**(8): 3577-3587.

McAlister, L. and D. B. Finkelstein (1980). "Heat shock proteins and thermal resistance in yeast." Biochem Biophys Res Commun **93**(3): 819-824.

McCarthy, D. J., Y. Chen and G. K. Smyth (2012). "Differential expression analysis of multifactor RNA-Seq experiments with respect to biological variation." Nucleic Acids Res **40**(10): 4288-4297.

McKeage, M. J. (1995). "Comparative adverse effect profiles of platinum drugs." Drug Saf **13**(4): 228-244.

Mellado Lagarde, M. M., G. Wan, L. Zhang, A. R. Gigliello, J. J. McInnis, Y. Zhang, D. Bergles, J. Zuo and G. Corfas (2014). "Spontaneous regeneration of cochlear supporting cells after neonatal ablation ensures hearing in the adult mouse." Proceedings of the National Academy of Sciences of the United States of America **111**(47): 16919-16924.

Mi, H., X. Huang, A. Muruganujan, H. Tang, C. Mills, D. Kang and P. D. Thomas (2017). "PANTHER version 11: expanded annotation data from Gene Ontology and Reactome pathways, and data analysis tool enhancements." Nucleic Acids Research **45**(D1): D183-D189.

Mi, H., A. Muruganujan, J. T. Casagrande and P. D. Thomas (2013). "Large-scale gene function analysis with the PANTHER classification system." Nature Protocols **8**: 1551.

Michalski, N. and C. Petit (2015). "Genetics of auditory mechano-electrical transduction." Pflugers Arch **467**(1): 49-72.

Montcouquiol, M., J. Valat, C. Travo and A. Sans (1998). "A role for BDNF in early postnatal rat vestibular epithelia maturation: implication of supporting cells." Eur J Neurosci **10**(2): 598-606.

Monzack, E. L., L. A. May, S. Roy, J. E. Gale and L. L. Cunningham (2015). "Live imaging the phagocytic activity of inner ear supporting cells in response to hair cell death." Cell Death And Differentiation **22**: 1995.

Moore, R. D., C. R. Smith and P. S. Lietman (1984). "Risk factors for the development of auditory toxicity in patients receiving aminoglycosides." J Infect Dis **149**(1): 23-30.

Moran, L., M. E. Mirault, A. P. Arrigo, M. Goldschmidt-Clermont and A. Tissieres (1978). "Heat shock of Drosophila melanogaster induces the synthesis of new messenger RNAs and proteins." Philos Trans R Soc Lond B Biol Sci **283**(997): 391-406.

More, S. S., O. Akil, A. G. Ianculescu, E. G. Geier, L. R. Lustig and K. M. Giacomini (2010). "Role of the copper transporter, CTR1, in platinum-induced ototoxicity." J Neurosci **30**(28): 9500-9509.

Morimoto, R. I. (1998). "Regulation of the heat shock transcriptional response: cross talk between a family of heat shock factors, molecular chaperones, and negative regulators." Genes Dev **12**(24): 3788-3796.

Morris, J. K., A. Maklad, L. A. Hansen, F. Feng, C. Sorensen, K. F. Lee, W. B. Macklin and B. Fritzsch (2006). "A disorganized innervation of the inner ear persists in the absence of ErbB2." Brain Res **1091**(1): 186-199.

Mukherjea, D., S. Jajoo, T. Kaur, K. E. Sheehan, V. Ramkumar and L. P. Rybak (2010). "Transtympanic administration of short interfering (si)RNA for the NOX3 isoform of NADPH oxidase protects against cisplatin-induced hearing loss in the rat." Antioxid Redox Signal **13**(5): 589-598.

Nagy, I., A. Monge, A. Albinger-Hegyi, S. Schmid and D. Bodmer (2005). "NF-kappaB is required for survival of immature auditory hair cells in vitro." J Assoc Res Otolaryngol **6**(3): 260-268.

Nicholas, B. D., S. Francis, E. L. Wagner, S. Zhang and J. B. Shin (2017). "Protein Synthesis Inhibition and Activation of the c-Jun N-Terminal Kinase Are Potential Contributors to Cisplatin Ototoxicity." Front Cell Neurosci **11**: 303.

O'Malley, J. T., J. B. Nadol, Jr. and M. J. McKenna (2016). "Anti CD163+, Iba1+, and CD68+ Cells in the Adult Human Inner Ear: Normal Distribution of an Unappreciated Class of Macrophages/Microglia and Implications for Inflammatory Otopathology in Humans." Otol Neurotol **37**(1): 99-108.

O'Reilly, A. M., R. W. Currie and D. B. Clarke (2010). "HspB1 (Hsp 27) expression and neuroprotection in the retina." Mol Neurobiol **42**(2): 124-132.

Oishi, N., S. Duscha, H. Boukari, M. Meyer, J. Xie, G. Wei, T. Schrepfer, B. Roschitzki, E. C. Boettger and J. Schacht (2015). "XBP1 mitigates aminoglycoside-induced endoplasmic reticulum stress and neuronal cell death." Cell Death Dis **6**: e1763.

Okano, T., T. Nakagawa, T. Kita, S. Kada, M. Yoshimoto, T. Nakahata and J. Ito (2008). "Bone marrow-derived cells expressing Iba1 are constitutively present as resident tissue macrophages in the mouse cochlea." Journal of Neuroscience Research **86**(8): 1758-1767.

Ottersen, O. P., Y. Takumi, A. Matsubara, A. S. Landsend, J. H. Laake and S. Usami (1998). "Molecular organization of a type of peripheral glutamate synapse: the afferent synapses of hair cells in the inner ear." Prog Neurobiol **54**(2): 127-148.

Ou, H. C., L. L. Cunningham, S. P. Francis, C. S. Brandon, J. A. Simon, D. W. Raible and E. W. Rubel (2009). "Identification of FDA-approved drugs and bioactives that protect hair cells in the zebrafish (Danio rerio) lateral line and mouse (Mus musculus) utricle." J Assoc Res Otolaryngol **10**(2): 191-203.

Ou, H. C., F. Santos, D. W. Raible, J. A. Simon and E. W. Rubel (2010). "Drug screening for hearing loss: using the zebrafish lateral line to screen for drugs that prevent and cause hearing loss." Drug Discov Today **15**(7-8): 265-271.

Owens, K. N., A. B. Coffin, L. S. Hong, K. O. Bennett, E. W. Rubel and D. W. Raible (2009). "Response of mechanosensory hair cells of the zebrafish lateral line to aminoglycosides reveals distinct cell death pathways." Hear Res **253**(1-2): 32-41.

Owens, K. N., F. Santos, B. Roberts, T. Linbo, A. B. Coffin, A. J. Knisely, J. A. Simon, E. W. Rubel and D. W. Raible (2008). "Identification of genetic and chemical modulators of zebrafish mechanosensory hair cell death." PLoS Genet **4**(2): e1000020.

Pagkalis, S., E. Mantadakis, M. N. Mavros, C. Ammari and M. E. Falagas (2011). "Pharmacological considerations for the proper clinical use of aminoglycosides." Drugs **71**(17): 2277-2294.

Pan, B., N. Akyuz, X. P. Liu, Y. Asai, C. Nist-Lund, K. Kurima, B. H. Derfler, B. Gyorgy, W. Limapichat, S. Walujkar, L. N. Wimalasena, M. Sotomayor, D. P. Corey and J. R. Holt (2018). "TMC1 Forms the Pore of Mechanosensory Transduction Channels in Vertebrate Inner Ear Hair Cells." Neuron **99**(4): 736-753.e736.

Park, M. K., B. D. Lee, S. W. Chae, J. Chi, S. K. Kwon and J. J. Song (2012). "Protective effect of NecroX, a novel necroptosis inhibitor, on gentamicin-induced ototoxicity." Int J Pediatr Otorhinolaryngol **76**(9): 1265-1269.

Peck, D., E. D. Crawford, K. N. Ross, K. Stegmaier, T. R. Golub and J. Lamb (2006). "A method for high-throughput gene expression signature analysis." Genome Biol **7**(7): R61.

Pirkkala, L., P. Nykanen and L. Sistonen (2001). "Roles of the heat shock transcription factors in regulation of the heat shock response and beyond." Faseb j **15**(7): 1118-1131.

Powell, D. (2015). Degust: Visualize, explore and appreciate RNA-seq differential gene-expression data. COMBINE RNA-seq workshop.

Previati, M., I. Lanzoni, L. Astolfi, F. Fagioli, G. Vecchiati, A. Pagnoni, A. Martini and S. Capitani (2007). "Cisplatin cytotoxicity in organ of Corti-derived immortalized cells." J Cell Biochem **101**(5): 1185-1197.

Raible, D. W. and G. J. Kruse (2000). "Organization of the lateral line system in embryonic zebrafish." J Comp Neurol **421**(2): 189-198.

Richter, K., M. Haslbeck and J. Buchner (2010). "The heat shock response: life on the verge of death." Mol Cell **40**(2): 253-266.
Ritossa, F. (1962). "A new puffing pattern induced by temperature shock and DNP in drosophila." Experientia **18**(12): 571-573.
Robinson, M. D., D. J. McCarthy and G. K. Smyth (2010). "edgeR: a Bioconductor package for differential expression analysis of digital gene expression data." Bioinformatics **26**(1): 139-140.
Rosenberg, B., L. Vancamp and T. Krigas (1965). "Inhibition of cell division in escherichia coli by electrolysis products from a platinum electrode." Nature **205**: 698-699.
Rosenberg, B., L. VanCamp, J. E. Trosko and V. H. Mansour (1969). "Platinum compounds: a new class of potent antitumour agents." Nature **222**(5191): 385-386.
Rozencweig, M., D. D. von Hoff, M. Slavik and F. M. Muggia (1977). "Cis-diamminedichloroplatinum (II). A new anticancer drug." Ann Intern Med **86**(6): 803-812.
Ryan, A. and P. Dallos (1975). "Effect of absence of cochlear outer hair cells on behavioural auditory threshold." Nature **253**(5486): 44-46.
Sagwa, E. L., N. Ruswa, F. Mavhunga, T. Rennie, H. G. Leufkens and A. K. Mantel-Teeuwisse (2015). "Comparing amikacin and kanamycin-induced hearing loss in multidrug-resistant tuberculosis treatment under programmatic conditions in a Namibian retrospective cohort." BMC Pharmacol Toxicol **16**: 36.
Salehi, A. H., S. J. Morris, W. C. Ho, K. M. Dickson, G. Doucet, S. Milutinovic, J. Durkin, J. W. Gillard and P. A. Barker (2006). "AEG3482 is an antiapoptotic compound that inhibits Jun kinase activity and cell death through induced expression of heat shock protein 70." Chem Biol **13**(2): 213-223.
Sanz, E., R. Evanoff, A. Quintana, E. Evans, J. A. Miller, C. Ko, P. S. Amieux, M. D. Griswold and G. S. McKnight (2013). "RiboTag analysis of actively translated mRNAs in Sertoli and Leydig cells in vivo." PLoS One **8**(6): e66179.
Sanz, E., L. Yang, T. Su, D. R. Morris, G. S. McKnight and P. S. Amieux (2009). "Cell-type-specific isolation of ribosome-associated mRNA from complex tissues." Proc Natl Acad Sci U S A **106**(33): 13939-13944.
Sapareto, S. A., L. E. Hopwood, W. C. Dewey, M. R. Raju and J. W. Gray (1978). "Effects of hyperthermia on survival and progression of Chinese hamster ovary cells." Cancer Res **38**(2): 393-400.
Sato, E., H. E. Shick, R. M. Ransohoff and K. Hirose (2010). "Expression of Fractalkine Receptor CX3CR1 on Cochlear Macrophages Influences Survival of Hair Cells Following Ototoxic Injury." Journal of the Association for Research in Otolaryngology **11**(2): 223-234.
Schacht, J. (1998). "Aminoglycoside ototoxicity: prevention in sight?" Otolaryngol Head Neck Surg **118**(5): 674-677.
Schacht, J., A. E. Talaska and L. P. Rybak (2012). "Cisplatin and aminoglycoside antibiotics: hearing loss and its prevention." Anat Rec (Hoboken) **295**(11): 1837-1850.
Schatz, A., E. Bugle and S. A. Waksman (1944). "Streptomycin, a Substance Exhibiting Antibiotic Activity Against Gram-Positive and Gram-Negative Bacteria." **55**(1): 66-69.
Scheffer, D. I., J. Shen, D. P. Corey and Z. Y. Chen (2015). "Gene Expression by Mouse Inner Ear Hair Cells during Development." J Neurosci **35**(16): 6366-6380.
Seyednasrollah, F., A. Laiho and L. L. Elo (2015). "Comparison of software packages for detecting differential expression in RNA-seq studies." Brief Bioinform **16**(1): 59-70.
Sha, S. H. and J. Schacht (1999). "Formation of reactive oxygen species following bioactivation of gentamicin." Free Radic Biol Med **26**(3-4): 341-347.
Sha, S. H., R. Taylor, A. Forge and J. Schacht (2001). "Differential vulnerability of basal and apical hair cells is based on intrinsic susceptibility to free radicals." Hear Res **155**(1-2): 1-8.
Shakil, S., R. Khan, R. Zarrilli and A. U. Khan (2008). "Aminoglycosides versus bacteria--a description of the action, resistance mechanism, and nosocomial battleground." J Biomed Sci **15**(1): 5-14.

So, H., H. Kim, J. H. Lee, C. Park, Y. Kim, E. Kim, J. K. Kim, K. J. Yun, K. M. Lee, H. Y. Lee, S. K. Moon, D. J. Lim and R. Park (2007). "Cisplatin cytotoxicity of auditory cells requires secretions of proinflammatory cytokines via activation of ERK and NF-kappaB." J Assoc Res Otolaryngol **8**(3): 338-355.

Stankiewicz, A. R., G. Lachapelle, C. P. Foo, S. M. Radicioni and D. D. Mosser (2005). "Hsp70 inhibits heat-induced apoptosis upstream of mitochondria by preventing Bax translocation." J Biol Chem **280**(46): 38729-38739.

Stankovic, K., C. Rio, A. Xia, M. Sugawara, J. C. Adams, M. C. Liberman and G. Corfas (2004). "Survival of adult spiral ganglion neurons requires erbB receptor signaling in the inner ear." J Neurosci **24**(40): 8651-8661.

Stepanyan, R. S., A. A. Indzhykulian, A. C. Velez-Ortega, E. T. Boger, P. S. Steyger, T. B. Friedman and G. I. Frolenkov (2011). "TRPA1-mediated accumulation of aminoglycosides in mouse cochlear outer hair cells." J Assoc Res Otolaryngol **12**(6): 729-740.

Stone, J. S., S. R. Wisner, S. A. Bucks, M. M. Mellado Lagarde and B. C. Cox (2018). "Characterization of Adult Vestibular Organs in 11 CreER Mouse Lines." J Assoc Res Otolaryngol **19**(4): 381-399.

Subramanian, A., R. Narayan, S. M. Corsello, D. D. Peck, T. E. Natoli, X. Lu, J. Gould, J. F. Davis, A. A. Tubelli, J. K. Asiedu, D. L. Lahr, J. E. Hirschman, Z. Liu, M. Donahue, B. Julian, M. Khan, D. Wadden, I. C. Smith, D. Lam, A. Liberzon, C. Toder, M. Bagul, M. Orzechowski, O. M. Enache, F. Piccioni, S. A. Johnson, N. J. Lyons, A. H. Berger, A. F. Shamji, A. N. Brooks, A. Vrcic, C. Flynn, J. Rosains, D. Y. Takeda, R. Hu, D. Davison, J. Lamb, K. Ardlie, L. Hogstrom, P. Greenside, N. S. Gray, P. A. Clemons, S. Silver, X. Wu, W. N. Zhao, W. Read-Button, X. Wu, S. J. Haggarty, L. V. Ronco, J. S. Boehm, S. L. Schreiber, J. G. Doench, J. A. Bittker, D. E. Root, B. Wong and T. R. Golub (2017). "A Next Generation Connectivity Map: L1000 Platform and the First 1,000,000 Profiles." Cell **171**(6): 1437-1452.e1417.

Sugawara, M., G. Corfas and M. C. Liberman (2005). "Influence of supporting cells on neuronal degeneration after hair cell loss." J Assoc Res Otolaryngol **6**(2): 136-147.

Sugawara, M., J. C. Murtie, K. M. Stankovic, M. C. Liberman and G. Corfas (2007). "Dynamic patterns of neurotrophin 3 expression in the postnatal mouse inner ear." J Comp Neurol **501**(1): 30-37.

Takada, Y., T. Takada, M. Y. Lee, D. L. Swiderski, L. L. Kabara, D. F. Dolan and Y. Raphael (2015). "Ototoxicity-induced loss of hearing and inner hair cells is attenuated by HSP70 gene transfer." Mol Ther Methods Clin Dev **2**: 15019.

Takahashi, Y. and M. Igarashi (2017). "Destination of aminoglycoside antibiotics in the 'post-antibiotic era'." J Antibiot (Tokyo).

Taleb, M., C. S. Brandon, F. S. Lee, K. C. Harris, W. H. Dillmann and L. L. Cunningham (2009). "Hsp70 inhibits aminoglycoside-induced hearing loss and cochlear hair cell death." Cell Stress Chaperones **14**(4): 427-437.

Taleb, M., C. S. Brandon, F. S. Lee, M. I. Lomax, W. H. Dillmann and L. L. Cunningham (2008). "Hsp70 inhibits aminoglycoside-induced hair cell death and is necessary for the protective effect of heat shock." J Assoc Res Otolaryngol **9**(3): 277-289.

Tao, L. and N. Segil (2015). "Early transcriptional response to aminoglycoside antibiotic suggests alternate pathways leading to apoptosis in sensory hair cells in the mouse inner ear." Frontiers in Cellular Neuroscience **9**(190).

Tissieres, A., H. K. Mitchell and U. M. Tracy (1974). "Protein synthesis in salivary glands of Drosophila melanogaster: relation to chromosome puffs." J Mol Biol **84**(3): 389-398.

Ton, C. and C. Parng (2005). "The use of zebrafish for assessing ototoxic and otoprotective agents." Hear Res **208**(1-2): 79-88.

van den Brink, S. C., F. Sage, A. Vertesy, B. Spanjaard, J. Peterson-Maduro, C. S. Baron, C. Robin and A. van Oudenaarden (2017). "Single-cell sequencing reveals dissociation-induced gene expression in tissue subpopulations." Nat Methods **14**(10): 935-936.

van Ruijven, M. W., J. C. de Groot, F. Hendriksen and G. F. Smoorenburg (2005). "Immunohistochemical detection of platinated DNA in the cochlea of cisplatin-treated guinea pigs." Hear Res **203**(1-2): 112-121.
van Ruijven, M. W., J. C. de Groot, S. F. Klis and G. F. Smoorenburg (2005). "The cochlear targets of cisplatin: an electrophysiological and morphological time-sequence study." Hear Res **205**(1-2): 241-248.
Vlasits, A. L., J. A. Simon, D. W. Raible, E. W. Rubel and K. N. Owens (2012). "Screen of FDA-approved drug library reveals compounds that protect hair cells from aminoglycosides and cisplatin." Hear Res **294**(1-2): 153-165.
Walters, B. J., S. Diao, F. Zheng, B. J. Walters, W. S. Layman and J. Zuo (2015). "Pseudo-immortalization of postnatal cochlear progenitor cells yields a scalable cell line capable of transcriptionally regulating mature hair cell genes." Sci Rep **5**: 17792.
Wan, G., G. Corfas and J. S. Stone (2013). "Inner ear supporting cells: rethinking the silent majority." Semin Cell Dev Biol **24**(5): 448-459.
Wang, P., P. Zhang, J. Huang, M. Li and X. Chen (2013). "Trichostatin A protects against cisplatin-induced ototoxicity by regulating expression of genes related to apoptosis and synaptic function." Neurotoxicology **37**: 51-62.
Wang, Q. and P. S. Steyger (2009). "Trafficking of systemic fluorescent gentamicin into the cochlea and hair cells." J Assoc Res Otolaryngol **10**(2): 205-219.
Wang, Y., A. Rattner, Y. Zhou, J. Williams, Philip M. Smallwood and J. Nathans (2012). "Norrin/Frizzled4 Signaling in Retinal Vascular Development and Blood Brain Barrier Plasticity." Cell **151**(6): 1332-1344.
Wangemann, P. (2006). "Supporting sensory transduction: cochlear fluid homeostasis and the endocochlear potential." J Physiol **576**(Pt 1): 11-21.
Watanabe, K., S. Inai, K. Jinnouchi, S. Baba and T. Yagi (2003). "Expression of caspase-activated deoxyribonuclease (CAD) and caspase 3 (CPP32) in the cochlea of cisplatin (CDDP)-treated guinea pigs." Auris Nasus Larynx **30**(3): 219-225.
Wei, T., V. Simko, M. Levy, Y. Xie, Y. Jin and J. Zemla (2017). "Package 'corrplot'." Statistician **56**: 316-324.
White, P. M., A. Doetzlhofer, Y. S. Lee, A. K. Groves and N. Segil (2006). "Mammalian cochlear supporting cells can divide and trans-differentiate into hair cells." Nature **441**: 984.
Whitesell, L., R. Bagatell and R. Falsey (2003). "The stress response: implications for the clinical development of hsp90 inhibitors." Curr Cancer Drug Targets **3**(5): 349-358.
Whitlock, N. A., N. Agarwal, J. X. Ma and C. E. Crosson (2005). "Hsp27 upregulation by HIF-1 signaling offers protection against retinal ischemia in rats." Invest Ophthalmol Vis Sci **46**(3): 1092-1098.
Yadav, M. K., J. Choi and J. J. Song (2014). "Protective effect of hexane and ethanol extract of piper longum L. On gentamicin-induced hair cell loss in neonatal cultures." Clin Exp Otorhinolaryngol **7**(1): 13-18.
Yang, H., J. Gan, X. Xie, M. Deng, L. Feng, X. Chen, Z. Gao and L. Gan (2010). "Gfi1-Cre knock-in mouse line: A tool for inner ear hair cell-specific gene deletion." Genesis (New York, N.Y. : 2000) **48**(6): 400-406.
Yang, T., E. S. Scholl, N. Pan, B. Fritzsch, F. Haeseleer and A. Lee (2016). "Expression and Localization of CaBP Ca2+ Binding Proteins in the Mouse Cochlea." PLoS One **11**(1): e0147495.
Yasunaga, S., M. Grati, M. Cohen-Salmon, A. El-Amraoui, M. Mustapha, N. Salem, E. El-Zir, J. Loiselet and C. Petit (1999). "A mutation in OTOF, encoding otoferlin, a FER-1-like protein, causes DFNB9, a nonsyndromic form of deafness." Nat Genet **21**(4): 363-369.
Yu, Y., A. J. Szczepek, H. Haupt and B. Mazurek (2009). "Geldanamycin induces production of heat shock protein 70 and partially attenuates ototoxicity caused by gentamicin in the organ of Corti explants." J Biomed Sci **16**: 79.

Zhang, D. S., V. Piazza, B. J. Perrin, A. K. Rzadzinska, J. C. Poczatek, M. Wang, H. M. Prosser, J. M. Ervasti, D. P. Corey and C. P. Lechene (2012). "Multi-isotope imaging mass spectrometry reveals slow protein turnover in hair-cell stereocilia." Nature **481**(7382): 520-524.
Zheng, J., W. Shen, D. Z. He, K. B. Long, L. D. Madison and P. Dallos (2000). "Prestin is the motor protein of cochlear outer hair cells." Nature **405**(6783): 149-155.

Biographical Information

EDUCATION

PhD Biochemistry, Johns Hopkins University School of Medicine.
August 2014-Present GPA 3.63, Biochemistry, Cell and Molecular Biology (BCMB) Program.
B.S. Biochemistry (with distinction), Neuroscience (2nd major) University of Virginia
Class of 2011

EMPLOYMENT and RESEARCH EXPERIENCE

Marketing and Small Business Analyst Internship, Biohealth Innovations. Rockville, MD.
July 2017 – September 2017
Investigative Research Analyst, AMPEL Biosolutions LLC. Charlottesville, VA.
December 2013 – December 2017
Research Technician, A. Ryan Laboratory, Department of Surgery, UCSD. La Jolla, CA.
July 2013 – July 2014
Research Associate, Jill Venton Laboratory, Chemistry Department, UVA. Charlottesville, VA.
August 2012- June 2013
Junior Fellowship, Post-Baccalaureate Intramural Training Award (IRTA), Lisa Cunningham Laboratory, NIDCD. Bethesda, MD.
July 2011- June 2012

PUBLICATIONS

Ryals M., Pak K., Jalota R., Kurabi A., Ryan AF. A kinase inhibitor library screen identifies novel enzymes involved in ototoxic damage to the murine organ of Corti. *PLoS One*. 2017;12(10):e0186001. https://doi.org/10.1371/journal.pone.0186001.
Grammer, A., **Ryals, M**., Heuer, S., Robl, R., Madamanchi, S., Davis, L., Lipsky, P. (2016). Drug repositioning in SLE: crowd-sourcing, literature-mining and Big Data analysis. *Lupus*, 25(10), 1150-1170.
Lipsky, P. E., **Ryals, M.**, Smearman, J., Soler, V., Grammer, A. (2014). A Novel Strategy to Identify and Evaluate Approved Drugs and Treatments for Repositioning As Therapies for Systemic Lupus Erythematosus (SLE). In *ARTHRITIS & RHEUMATOLOGY* (Vol. 66, pp. S294-S294).
Nguyen, M. D., Lee, S. T., Ross, A. E., **Ryals, M.**, Choudhry, V. I., Venton, B. J. (2014). Characterization of spontaneous, transient adenosine release in the caudate-putamen and prefrontal cortex. *PloS One*, 9(1), e87165.
Nguyen, M. D., Ross, A. E., **Ryals, M.**, Lee, S. T., & Venton, B. J. (2015). Clearance of rapid adenosine release is regulated by nucleoside transporters and metabolism. *Pharmacology Research & Perspectives*, 3(6).
Roy, S.*, **Ryals, M.***, Van den Bruele, A. B., Fitzgerald, T. S., & Cunningham, L. L. (2013). Sound preconditioning therapy inhibits ototoxic hearing loss in mice. *J Clin Invest*, 123(11), 4945-4949.
*Co-first authors.